University of Canterbury

Masters Thesis

Cognitive impairment in Parkinson's disease: a study of early-phase amyloid PET and arterial spin labeling perfusion MRI

Author:
Megan Stark

Supervisors:
Dr. Steve Marsh
Dr. Tracy Melzer

A thesis submitted in fulfilment of the requirements for the degree of Master of Science in Medical Physics

in the

College of Science
Department of Physics and Astronomy

April 2016

Abstract

Cognitive impairment in Parkinson's disease:
a study of early-phase amyloid PET and arterial spin labeling perfusion MRI

by Megan Stark

The characteristic motor symptoms present in Parkinson's disease are often accompanied by a range of non-motor symptoms; in particular, cognitive impairment leading to dementia has an 80% cumulative prevalence in PD but with incredibly variable time for dementia onset. This study presents and compares early-phase [^{18}F] Florbetaben (FBB) positron emission tomography (PET) and arterial spin labeling magnetic resonance imaging (ASL MRI) of perfusion in the context of cognitive decline and imminent conversion to dementia in Parkinson's disease.

Patients underwent a comprehensive neuropsychological battery prior to inclusion in the study, which was used to classify patients as PD with normal cognition (PD-N, n=4), mild cognitive impairment (PD-MCI, n=41) or dementia (PDD, n=5), and to assign each patient a summary global cognitive score and an individualized Parkinsons disease dementia risk score (PDDRS). Early-phase FBB PET images, and structural and arterial spin labeled MR images were acquired for each patient, which were then coregistered, normalized and smoothed in preparation for analysis.

The relative measures of brain function given by each imaging modality were analysed using the general linear model, in order to identify any association with cognitive status and dementia risk in the subject group. Cognitive decline and increased dementia conversion risk were found to be significantly associated with distinct regions of cortical hypoperfusion as quantified by the ASL data. FBB-derived images did not exhibit any significant association with cognition or dementia risk, and did not correlate significantly with ASL perfusion measures, suggesting that the two techniques are measuring different physiological phenomenon. A network based approach using principal component analysis identified networks of cortical hypoperfusion in the ASL data that related significantly to cognition and risk of conversion to dementia.

This thesis raises questions regarding the physiological information presented by early-phase PET, which remains a worthwhile area of further investigation. The PDDRS-related perfusion network developed here presents a potential biomarker of imminent conversion to dementia in Parkinsons disease.

Acknowledgements

This research would not have been possible without the exceptional support and encouragement I have received from my supervisors, Dr. Tracy Melzer and Dr. Steve Marsh. Their endless patience, knowledge and scientific advice have been indispensable, and I thank them for always fielding my many questions with ease.

I would like to thank my friends and colleagues at the New Zealand Brain Research Institute for their feedback and support, and the daily lunch-time chats that made working at the NZBRI such a pleasure. Special acknowledgement must be made of the tireless work done by Leslie Livingston, Kyla-Louise Wood and all those involved in recruiting and assessing patients at the NZBRI, without whom this research would not have been possible.

Lastly, I thank my friends and family for their constant support, encouragement and understanding. Without them I would be lost, and seriously lacking in coffee.

Contents

List of Figures

List of Tables

Abbreviations

PD	Parkinson's Disease
PD-N	Parkinson's Disease with Normal cognition
PD-MCI	Parkinson's Disease with Mild Cognitive Impairment
PDD	Parkinson's Disease Dementia
ASL MRI	Arterial Spin Labelling Magnetic Resonance Imaging
PET	Positron Emission Tomography
FBB	[^{18}F]Florbetaben
PDDRS	Parkinson's Disease Dementia Risk Score
DICOM	Digital Imaging and Communications in Medicine
NIFTI	Neuroimaging Informatics Technology Initiative
CBF	Cerebral Blood Flow
TOFAC	Time-Of-Flight Attenuation-Corrected
SUVR	Standard Uptake Value Ratio
3D SPGR	3D Spoiled Gradient Recalled echo
SPM	Statistical Parametric Mapping
rBPM	robust Biological Parametric Mapping
FSL	FMRIB Software Library
GLM	General Linear Model
PCA	Principal Component Analysis
TFCE	Threshold-free Cluster Enhancement
FWE	Family-wise Error rate
FDR	False Discovery Rate
LOO	Leave-One-Out cross-validation

Chapter 1

Introduction

1.1 Research Rationale

Parkinson's disease (PD) is the second most common neurodegenerative disorder behind Alzheimer's disease (AD) (Alves et al., 2008), increasing in prevalence with age. PD affects an estimated 1% of those over 60 and 4% of individuals in the oldest age group (de Lau & Breteler, 2006). PD currently affects roughly 10,000 people in New Zealand (T. J. Anderson, 2013), with an average age at diagnosis of 59[1]. Demographic trends predict this number to double by 2035 and quadruple by 2050 (Bach et al., 2011).

The clinical features of PD are dominated in the early disease stages by motor symptoms of rigidity, postural instability, bradykinesia and resting tremor (Dickson, 2012). These primary motor symptoms have been attributed to the loss of dopaminergic neurons in the substantia nigra and small mid-brain structures, which was thus commonly regarded as the epicentre of PD neuropatholgy for many years. Treatment of the motor symptoms targets the dopaminergic nigrostriatal pathway and is typically effective in early disease stages, thus disease burden is more heavily influenced by dysfunction in non-motor aspects of patient health. Over the last decade, the observation that the heterogeneous motor symptoms are often accompanied by several non-motor features has driven much broader research concerning the etiology, pathogenesis and treatment of PD (Docherty & Burn, 2010). What has emerged is a continually evolving disease picture wherein the non-motor

[1] http://www.parkinsons.org.nz/

features are becoming an increasingly significant source of disability and carer burden (T. J. Anderson, 2013).

In particular, cognitive decline and conversion to Parkinson's disease dementia (PDD) is known to greatly reduce patient quality of life, and often necessitates full time or nursing home care. Of the roughly 7 million people affected by PD globally, 80% are expected to progress to PDD anywhere from 2-20 years after clinical diagnosis (Aarsland & Kurz, 2010). Mild cognitive impairment in PD (PD-MCI) is considered to confer higher risk of conversion to PDD, however dementia onset is also variable within this group. Ideally, all PD-MCI would be offered the opportunity for inclusion in trials for preventative therapies, however this is impractical at early trial stages and inclusion of those with a natural preservation of cognition may mask trial results. The goal thus becomes the elucidation of any core neuropathological features driving conversion to PDD, that may be preserved in those PD-MCI subjects exhibiting sustained cognitive status. This thesis is but one part of a wider HRC funded study with the New Zealand Brain Research Institute (NZBRI) that aims to identify genetic, clinical and imaging biomarkers to this effect (T. J. Anderson, 2013).

1.1.1 Thesis aims

This thesis focuses on the use of neuroimaging techniques in the evaluation of cognitive status and dementia risk, specifically imaging brain perfusion in those classified as PD-MCI. The aim is to construct an informative model, based on perfusion data, that may be used to predict cognitive status in individuals and perhaps help to identify those at risk of imminent conversion to PDD. The model is constructed based on the perfusion data of 50 PD subjects taking part in the HRC funded study at NZBRI. Data was obtained using arterial spin labelling MRI (ASL MRI), a well established method of perfusion imaging, and early-phase PET imaging of the Amyloid tracer Florbetaben (FBB). This second method is investigated as a novel method of imaging perfusion, and compared against the images obtained using ASL MRI through voxel wise statistical analysis. All subjects underwent an extensive neuropsychological battery to produce an overall cognitive score and Parkinson's disease dementia risk score (PDDRS) prior to scanning. This thesis investigates if there exists any correlation within the data provided by both modalities

with the cognitive scores and PDDRS of the subject group, with the aim to form perfusion networks predictive of cognitive status and conversion risk using these data.

1.2 Neuropathology and imaging of cognition

The neuropathological basis of cognitive dysfunction in PD is not well understood, and research into the underlying causes of cognitive deterioration is ongoing. The observation of metabolic abnormalities in PD has provided valuable insight and enabled the development of an analysis framework that may be applied to data concerning other aspects of brain function, such as cerebral blood flow.

1.2.1 Metabolic changes

Deficiencies in both dopaminergic and non-dopaminergic neurotransmitters, such as serotonin, norepinephrine, and acetylcholine, are frequently implicated in the pathogenesis of non-motor features in PD (Scatton et al., 1983) (Hasselmo, 2006), notably cognition. As such, these possible biomarkers of cognition in PD have provided the impetus for several pharmacological interventions for the treatment of cognitive impairment and mood (Diaz & Waters, 2009). Underlying the deficiencies in these neurotransmitters is neuronal dysfunction. A properly functioning neuron utilises cerebral glucose in the production of ATP, which is in turn used by the cell in neuronal maintenance and production of neurotransmitters (Mergenthaler et al., 2013). Thus, measuring the regional cerebral metabolic rate of glucose (rCMRglc) provides a useful measure of neuronal function. Imaging rCMRglc with ^{18}F-fluorodeoxyglucose (FDG) PET has therefore been understandably well explored as an avenue of disease severity assessment in neurodegenerative disorders (Eidelberg et al., 1995).

Cortical hypometabolism has been linked to cognitive changes in PD in several independent studies using FDG PET (Huang, Mattis, et al., 2007) (Ma et al., 2007) (Liepelt et al., 2009). However, due to the substantial variability in metabolic activity between brain regions, it is difficult to use regional estimates of metabolism to adequately describe response to treatment in a clinical setting. A more clinically relevant measure has been provided by network analysis, wherein multivariate analysis is used to extract regions of abnormal metabolic activity in PD vs controls, that correlate significantly with motor

dysfunction and the results of neurological testing. Independent metabolic networks of spatial covariance relating to motor and cognitive aspects of the disease have provided unique insight into the areas of the brain implicated in PD (Huang, Tang, et al., 2007). The efficacy of a cognition-related metabolic spatial covariance pattern (PDCP) in the evaluation of cognition in PD has been previously validated (Huang et al., 2008), wherein expression of the network was seen to increase stepwise with worsening cognitive impairment ($p < 0.01$). This method is not limited to metabolic information, and it is of clinical interest to explore network analysis with other measures of brain function. One such objective measure also known to correlate with neuronal function is cerebral blood flow.

1.2.2 Network analysis of cerebral blood flow

The network approach of Huang et al. may also be used to examine patterns of cerebral blood flow (CBF), or brain perfusion, in PD.

Perfusion refers to the capillary blood supply delivering oxygen and nutrients to brain tissue, in units of ml/min/100g (T. R. Melzer, 2011). While technically a measure of simple flow rate (ml/min), the term CBF is somewhat synonymous with perfusion in the literature. Similarly to rCMRglc, measuring regional CBF is a useful method of inferring neuronal function, such that decreases in ATP production and consumption due to neuronal damage are concomitant with changes in cerebral perfusion. Blood flow to the damaged region may decrease, while other regions may see compensatory increases. This same effect may also indicate disease- or age-related vasoconstriction, which must be corrected for in study designs including older subjects.

There is a close coupling between rCMRglc (μmol/min/100g) and regional CBF (rCBF) at rest, measured consecutively in the same individuals with FDG PET and $H_2^{15}O$ PET respectively (Jueptner & Weiller, 1995). Imaging rCBF using PET or single-photon emission computed tomography (SPECT) does not yield absolute, quantitative values, but rather relative values normalised to a reference region or global mean. This can introduce bias if there is a systematic increase or reduction in blood flow across the subject group, either globally or in the chosen reference region. ASL provides an alternative method of imaging CBF that yields absolute perfusion values in a completely non-invasive manner (T. Melzer et al., 2011), and has shown to accord well with perfusion studies using $H_2^{15}O$ PET (Ye et al., 2000). ASL offers faster scan times over tracer techniques, deposits no

radiation dose to the patient, and is an easily repeatable addition to existing MRI routines (T. R. Melzer, 2011). Little processing is required to extract absolute perfusion values from these data.

A previous study conducted at the NZBRI explored the efficacy of ASL MRI data in the construction of a disease-related network in PD, relating to motor and cognitive aspects of the disease (T. Melzer et al., 2011). Areas found to be involved in the network included decreases in posterior and lateral posterior parietal areas and dorsolateral prefrontal cortex, with preserved perfusion in globus pallidus. Areas of decreased perfusion indicated by the network were found to be significantly related to cognition as measured by MoCA score (P=0.001, $\beta = 0.41$), but no other variables.

It will be useful to construct a spatial covariance network of perfusion using novel early-phase PET and compare this to ASL-derived networks. Replication of the previous results may validate the pre-processing chain and analysis used in this thesis, such that results from early-phase PET imaging may be regarded as correct for this subject group.

1.2.3 Early-phase PET imaging using an amyloid tracer

Early-phase PET imaging involves obtaining PET data immediately following injection, such that the uptake of the radiotracer is imaged. This contrasts with late-phase PET, where much of the radioactivity has been eliminated and what remains is related to the biological process of interest.

Early-phase PET has been seen to correlate highly with metabolic information obtained using FDG PET in the same individuals (Hsiao et al., 2012). Given the high correlation between CBF and glucose metabolism, it may be that this data is providing perfusion-like information and could be used in a similar fashion to ASL MRI data in spatial covariance network analysis. Should this hypothesis prove true, the clinical implications may be highly significant as one tracer may be used to image multiple aspects of PD pathology in one PET session. This is valuable in the case of limited scanner availability, and would reduce cost and patient exposure to ionising radiation. Using a tracer that binds to amyloid plaques for this purpose enables the investigation of amyloid deposition in PD using late-phase PET.

The aggregation of misfolded β-amyloid (Aβ) proteins into plaques within the brain is a diagnostic hallmark of Alzheimer's disease (AD), and has been implicated particularly in early AD as a precursor to neuronal damage and cortical atrophy (Nordberg, 2004). The deposition of amyloid in AD has been shown to precede cognitive impairment, and may continue to accumulate as subjects move into the disease stage, namely memory loss, cerebral atrophy and dementia (Villain, 2012). It is not much of a step to extend this investigation of Aβ to include cognitive decline in PD. Amyloid deposition has been shown to occur in PD-MCI and PDD, with a greater point prevalence in PDD (Petrou et al., 2015).

The potential link of Aβ with cognition in PD will be investigated under the wider study at NZBRI, and may provide another indication of dementia risk in PD. While outside the scope of this thesis, the Aβ study nonetheless influences the choice of tracer used here in order to achieve the clinical benefit of informative early *and* late-phase PET in the same session.

1.2.3.1 Choice of amyloid PET tracer

Historically, the PET tracer of choice for imaging amyloid deposition has been [^{11}]C Pittsburgh Compound B (PiB) (Klunk et al., 2004). For most practical applications, imaging Aβ plaques using PiB PET is unfeasible due to the short half life of ^{11}C ($\sim$ 20 minutes), necessitating an in-house cyclotron for tracer production. Longer-lived fluorine-18 labeled radiotracers (half-life $\sim$ 110 minutes) have been developed that achieve comparable levels of binding to Aβ plaques, and may be produced commercially off-cite and delivered to the PET-scanning facility. There have been three such tracers labelled with ^{18}F approved by the US Food and Drug Administration (FDA) for imaging Aβ plaques: florbetapir, flutemetamol and florbetaben (Jeffrey, 2014). Florbetaben (FBB) in particular displays excellent linear correlation with global PiB standard uptake value ratio (SUVR) in AD (r=0.97, p$<$ 0.0001) with a similar effect size to PiB (Cohen's d, Pib: 3.3; FBB: 3.0)(Villemagne et al., 2012), and tracer binding matches well with Aβ distribution given by post-mortem biopsy (T. J. Anderson, 2013). FBB may be readily produced and transported in a timely manner from Cyclotek Pty Ltd in Melbourne, for use in PET scanning at Southern Cross Hospital, Christchurch. Thus, FBB was the radiotracer of choice for this study.

1.2.3.2 Florbetaben pharmacokinetics

FBB is a fluorine-18 labeled stilbene derivative that has demonstrated high binding affinity to Aβ plaques in the brain of AD patients (Sabri et al., 2015). FBB binds highly to plasma proteins, with an unbound fraction of 1.6%, making this radiotracer well suited for imaging arterial blood supply. Uptake within the brain is rapid, reaching a maximum ^{18}F radioactivity concentration of ∼6% injected dose/L at 10 minutes post intravenous injection of 300 MBq of FBB. PET imaging is thus conducted over the immediate 10 minutes post injection in an effort to image the initial radiotracer uptake within the brain (early-phase).

FBB is eliminated from blood plasma with a mean biological half-life of ∼1 hour, and is completely eliminated from the body within 24 hours post injection. The mean effective radiation dose a typical patient will receive from administration of 300 MBq FBB is 5.8 ± 0.42 mSv, which has been shown to be well tolerated (Sabri et al., 2015).

Chapter 2

Imaging principles

In this chapter, I will discuss the operational and physical principals behind the imaging modalities used in this study, namely positron emission tomography (PET) and arterial spin labeling magnetic resonance imaging (ASL MRI). Both modalities are employed to obtain perfusion data, with the aim to compare the two and extract characteristic perfusion networks relating to cognition and dementia risk in our subjects. ASL MRI has been shown previously to yield networks of abnormal perfusion relating to cognitive decline in PD-MCI(T. Melzer et al., 2011), thus this study determines if PET perfusion imaging may yield comparable results within our subject group.

2.1 Positron Emission Tomography

Positron emission tomography (PET) is an imaging modality based on the detection of annihilation coincidence photons, following injection of a positron-emitting tracer substance. Depending on the pharmaceutical attached to the radionuclide, the tracer may be used to examine a variety of biologic functions and processes. In this case, the initial up-take and flow of the amyloid tracer, [^{18}F]Florbetaben (FBB), will be imaged immediately following injection to obtain the early-phase information. The scanner used in this study is a GE Discovery 690 PET-CT scanner.

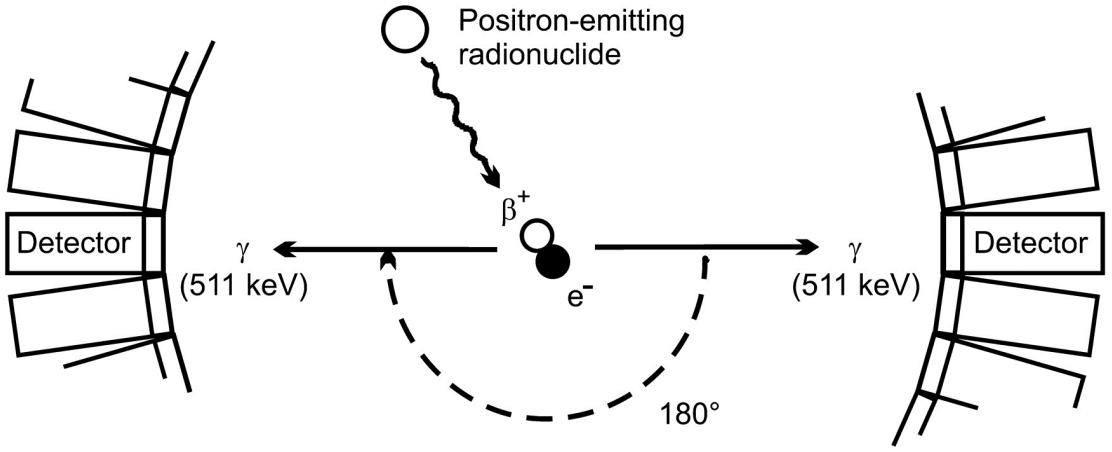

FIGURE 2.1: Emission of two 511-keV photons by electron-positron annihilation following positron emission by the radionuclide. Figure adapted from (Verel et al., 2005).

2.1.1 Principals of Operation

Annihilation coincidence photons are produced when a positron emitted from the decay of a proton-rich radionuclide interacts with an electron, causing annihilation. This annihilation converts the entire mass of the electron-positron pair into two 511-keV photons, travelling in nearly-opposite directions. Positrons travel only very short distances in matter before annihilation occurs, thus detection of the position of the interaction provides the approximate location of the tracer substance within the patient at the time of emission (see figure 2.1). Transverse images of the activity distribution within the patient may then be reconstructed from the acquired data by the PET system computer. Annihilation photons must escape the patient to be detected, and are thus affected by attenuation and scatter that serve to reduce image quality. Modern PET scanners are almost always coupled with x-ray CT systems to allow on-board attenuation correction, while energy-discrimination and timing circuits attempt to separate true coincidences from random coincidences and those affected by scatter (Bushberg et al., 2012, Chapter 19).

2.1.1.1 True Annihilation Coincidence Detection

The detector geometry encircles the patient and is designed to detect annihilation photons produced at approximately the same time. The line connecting these detected photons is termed the line of response (LOR), along which an annihilation interaction is presumed to have occurred. Annihilation coincidence detection (ACD) thus establishes the trajectories of detected photons without the use of collimation, avoiding the loss of sensitivity

and reduced spatial resolution that occurs with collimated detector systems. However, the detected LOR's may provide inaccurate information as a result of scatter and random coincidence detection. Figure 2.2 depicts true, scatter and random coincidence detection. A *true coincidence* is given by the nearly simultaneous detection of two annihilation photons resulting from a single interaction, and gives the correct LOR. A *scatter coincidence* is a true coincidence resulting from a single interaction, but gives an incorrect LOR as a result of photon scatter within the patient shifting the apparent origin of the annihilation photons. A *random coincidence* detection gives a false LOR as a result of the nearly simultaneous detection of two annihilation photons produced from separate interactions, mistakenly identified as coincidence photons. Scatter and random coincidences thus reduce image contrast and increase statistical noise in PET data; to combat this, PET systems use detectors capable of energy discrimination and highly accurate timing circuits to detect true coincidence pairs.

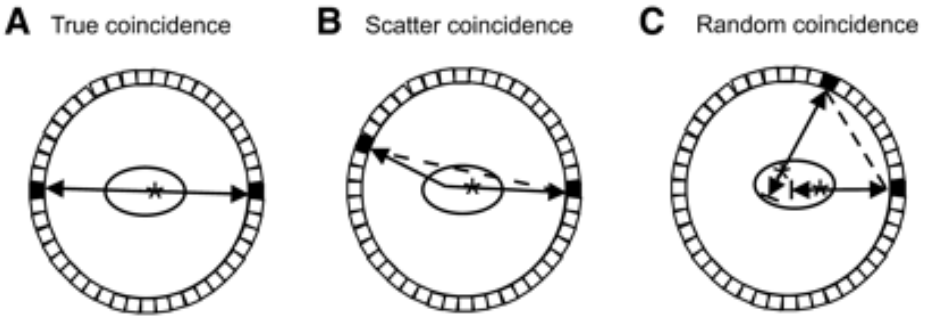

FIGURE 2.2: True, scatter and random coincidence detection. Figure adapted from (Verel et al., 2005).

2.1.2 PET Detector System

A typical PET detector system consists of several rings of detectors surrounding the patient. Scintillation detectors are used in PET systems over gas-filled or semi-conductor detectors, as these have comparatively low intrinsic efficiency for the detection of 511-keV photons. Scintillation detectors generally consist of large scintillator crystals coupled to several photomultiplier tubes (PMTs). Scintillation materials absorb the energy of incident ionising radiation and re-emit it in the form of visible or ultraviolet light in a process known as luminescence (Bushberg et al., 2012, Chapter 17). Luminescence occurs as an electron drops from an excited energy state, provided by the incident 511-keV photon, to a lower energy state, ideally releasing a photon of light with energy equal

to the transition. The emitted photon is converted into electrical current and amplified by the PMT electronics, and the location of the scintillation event determined from the relative magnitudes of the signals produced by the PMTs. The accuracy of the signal obtained by this detector is thus dependent on the many different components and the various efficiencies of each component in detecting and converting the deposited energy between forms.

The PMTs operate in pulse-mode such that each scintillation interaction is processed separately from other interactions, yielding the time signal, deposited energy, and location of each interaction. The scintillation material used in PET systems is chosen to give a high detection and conversion efficiency for 511-keV photons, with a short decay time between electron energy states, decreasing the dead-time at high count rates. The material is also ideally transparent to it's own emissions. High detection and conversion efficiency for 511-keV photons is particularly important for use in timing circuits and energy resolution in the PET system electronics. Historically, bismuth germanate ($Bi_4Ge_3O_{12}$), abbreviated BGO) has been the material of choice for PET scintillation detectors due to it's high density and high detection efficiency, but is now being passed over in favour of recently developed inorganic materials with comparable detection characteristics and shorter decay times. The material used in the GE Discovery 690 PET/CT Scanner is cerium-doped lutetium yttrium oxyorthosilicate ($Lu_2Y_{2-x}SiO_4O$, abbreviated LYSO). The light emitted by the LYSO crystals is converted to an electrical signal and amplified by the PMTs. The signal collected by each PMT is rejected or accepted according to an acceptable energy window around the 511-keV annihilation energy, and passed through timing circuits which generate a time signal for each pulse. Coincidence circuitry then determines coincidence pairs and LOR's based on this information.

The rate of random coincidence detection is dependent on the coincidence time window τ and the actual count rates S_1 and S_2 at the corresponding detectors, given by:

$$R_{random} = \tau S_1 S_2$$

At higher count rates, the rate of random coincidence detection increases and will decrease the signal-to-noise ratio of the resulting images. In systems able to employ a sufficiently small time window, considerations for time-of-flight (TOF) of emitted photons can be

made. Without TOF information, the probability of interactions along the LOR is assumed to be uniform. TOF information allows localisation of interaction events along the LOR within a Gaussian distribution of width Δx, reducing noise correlation between two emission events (Surti, 2015). This serves to increase the SNR and reduce artifacts, and is particularly useful for high count rates and when imaging larger volumes. In this study, TOF corrections are made by the on-board scanner software for early-phase PET data to due the very high count rates incident on the detector directly following injection.

2.1.2.1 GE Discovery 690 PET/CT detector components

The GE Discovery 690 PET/CT detector system consists of 24 concentric detector rings 81 cm in diameter, with a total detector width along the z-axis of 40 mm. 64 image slices may be obtained simultaneously across a 157 mm axial field of view (FOV). The entire detector system contains 13824 cerium-doped lutetium yttrium oxyorthosilicate ($Lu_2Y_{2-x}SiO_4O$, abbreviated LYSO) scintillation crystals. LYSO is an inorganic scintillation material developed as an alternative to BGO, discussed previously. LYSO has attenuation properties that are very similar to those of BGO, and also has a much higher rate of decay from the excited state, providing prompt emission of light. The coincidence time window for this system is 4.9ns, allowing corrections for TOF.

2.2 Magnetic Resonance Imaging - the basics

Magnetic resonance imaging (MRI) is an imaging technique based on the magnetic properties inherent to the nucleus of an atom. Protons and neutrons within a nucleus possess nuclear 'spin', which can be understood as magnetic dipoles. In stable nuclei containing equal numbers of protons and neutrons, these magnetic dipoles sum to zero and cancel out. When there are uneven numbers of protons and neutrons, a nuclear magnetic moment exists about the nucleus, often visualised as an arrow vector with magnitude and direction. Under the influence of an external magnetic field B_0, a large number of nuclei possessing random magnetic orientation will assume a non-random alignment in either the direction of the applied magnetic field (parallel) or in the opposite direction (anti-parallel). There will be a slightly higher proportion of spins aligned in the parallel direction, thus producing a net magnetisation within the sample. By convention, the

magnetic field B_0 is applied in the z-direction of a three-dimensional cartesian coordinate system; the net magnetisation in the direction of the applied magnetic field is thus denoted M_z and is known as the longitudinal magnetization. This magnetisation is maximal under equilibrium conditions and is denoted M_0, the equilibrium magnetisation.

An applied external magnetic field B_0 also causes a magnetic spin to have a certain precessional frequency about it's axis, proportional to the strength of the magnetic field and determined by the gyromagnetic ratio unique to each element. This relationship may be written as:

$$\omega = \gamma B_0 \tag{2.1}$$

where ω is the resonant or Larmour frequency and γ is the gyromagnetic ratio (for hydrogen, ω = 127.7 MHz at 3T, γ = 42.57 MHz T^-). Equation 2.1 describes the behaviour of a magnetic spin within an external magnetic field, and is thus the key relationship underpinning MRI (T. R. Melzer, 2011).

The net magnetisation of spins within a magnetic field is not sufficient to produce signal in MR. To obtain signal, the net longitudinal magnetisation must be tipped into the transverse plane. Application of a radio frequency (RF) electromagnetic pulse perpendicular to B_0 and tuned to the resonant frequency promotes spins from the lower energy parallel direction to the higher energy anti-parallel direction, and causes brief phase coherence (Bushberg et al., 2012). This phase coherence generates a perpendicular magnetisation vector rotating at the applied RF frequency, known as the transverse magnetisation M_{xy}. Immediately following a 90° RF pulse, M_z is at a minimum and M_{xy} is at a maximum. The gradual return of the excited spins to equilibrium, where M_z is maximal and M_{xy} is zero, results in the emission of energy equal to the energy of the applied RF pulse. This energy emission is detected by receiver coils and generates the all-important MR signal. The rate at which the transverse and longitudinal magnetisation decay occur are dependent on the structural and magnetic characteristics of the sample, and enable the large amount of tissue selectivity available using MR. These characteristics determine the so-called T1 and T2 relaxation times of tissues, and relate to longitudinal magnetisation recovery and transverse magnetisation decay respectively.

2.2.1 T1 and T2 relaxation

T1: spin-lattice

Immediately following the excitation pulse, longitudinal magnetization M_z will begin to recover as a result of excitation energy being released from the spin back to the lattice of molecules surrounding it; it is thus termed *spin-lattice relaxation*. T1 is the time taken for the exponential recovery of M_z to reach 63% of equilibrium following a 90° excitation pulse. Spin-lattice relaxation is highly dependent on the molecular structure and composition of tissue; long T1 times are given by dense structures and watery fluids, while viscous fluids possess the shortest T1 times. The recovery of longitudinal magnetisation may be described by the following equation (Brown et al., 2014):

$$M_z = M_z(0)e^{-t/T1} + M_0[1 - e^{-t/T1}] \tag{2.2}$$

where $M_z(0)$ is the longitudinal magnetisation at the time of the excitation pulse and t is the elapsed time from the excitation pulse.

T2: spin-spin

The initial transverse magnetisation M_{xy} induces a damped sinusoidal signal in the receiver coil, known as the free induction decay (FID) envelope. T2 relaxation is the time taken for the FID envelope to exponentially decay to 37% of the peak level following the excitation pulse. Transverse magnetisation decay occurs due to macromagnetic inhomogeneities in the local magnetic field of the tissue causing the excited spins to gradually dephase, thus earning the moniker, *spin-spin relaxation*. The decay of transverse magnetisation due to T2 effects may be described by the following equation (Brown et al., 2014):

$$M_{xy} = M_{xy}(0)e^{-t/T2} \tag{2.3}$$

Dephasing of spins occurs faster in tight structures able to support local magnetic field variations, and slower in free moving amorphous structures. Thus, dense structures such as bone exhibit very short T2, while fluids such as cerebrospinal fluid (CSF) exhibit long T2. Dephasing may also be caused by inhomogeneities in the applied magnetic field B_0,

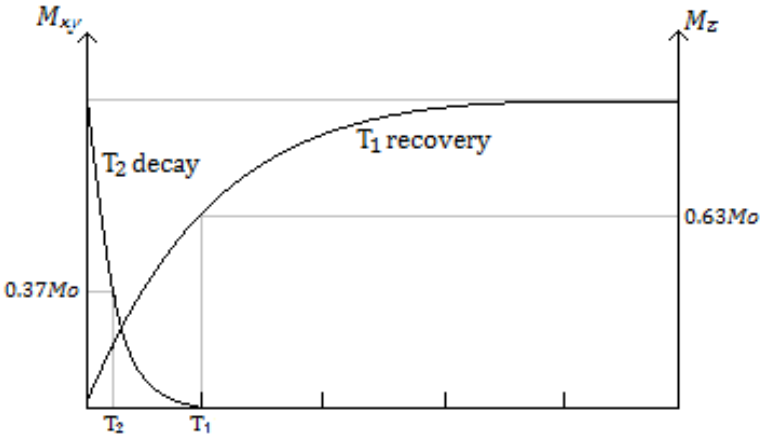

FIGURE 2.3: T1 and T2 decay for the same tissue. T1 recovery is on the order of 5-10 times longer than T2, although they both occur simultaneously. Figure adapted from (McRobbie et al., 2003).

characterised by the time constant T'. The transverse magnetisation decay constant due to both intrinsic and extrinsic inhomogeneities is termed T2*, and is always shorter than T2. T2* is related to T2 and T' by

$$\frac{1}{T2^*} = \frac{1}{T2} + \frac{1}{T2'} \tag{2.4}$$

T1 is typically on the order of 5 to 10 times longer than T2 (see table 2.1); the difference in decay time of longitudinal and transverse magnetisation in the same tissue is depicted in 2.3. While both longitudinal recovery and transverse decay occur simultaneously, M_{xy} can be seen to decrease significantly faster.

The tuning of various imaging parameters in an MR pulse sequence makes use of these differences in the T1 and T2 constants of different tissues in order to obtain the desired tissue contrast.

Tissue	T1 (ms)	T2 (ms)
Grey matter	1820	100
White matter	1084	70
Cerebrospinal fluid	4163[a]	500[b]
Fat	371	133
Blood	1932	275

a. Value retrieved from (Lin et al., 2001)
b. Value retrieved from (Piechnik et al., 2009)

TABLE 2.1: Approximate values for T1 and T2 at B_0 =3T and 37° (Stanisz et al., 2005).

2.2.2 MRI pulse sequence parameters

There are many different pulse sequences used in MRI to emphasise differences in proton density, T1 times, and T2 times of tissues. There are several important parameters employed to this effect that vary depending on the imaging objective.

The *repetition time* (TR) is the period of time between excitation pulses, during which T1 recovery and T2 and T2* decay occur. The length of TR varies depending on the pulse sequence employed, and may be on the order of milliseconds to thousands of milliseconds.

The *echo time* (TE) is the time between the excitation pulse and the peak amplitude of the FID echo. The echo is produced by applying a 180° inversion pulse at TE/2, causing rephasing of the spins and subsequent regrowth of the FID envelope, producing an 'echo' with peak amplitude at time TE. This is known as a *spin echo* pulse sequence (figure 2.4). Some pulse sequences use magnetic field gradients in place of an inversion pulse to produce an echo; in these sequences, a negative magnetic field gradient applied directly after the 90° RF pulse causes rapid loss of phase coherence, which is then reversed by switching the polarity of the applied gradient. When the effects of the negative gradient have been completely reversed by the positive gradient, an echo is produced; however, this and subsequent echoes will decay exponentially according to T2*, as the gradients do not correct for the effects of intrinsic and extrinsic magnetic field inhomogeneities (T2 and T2* effects). This sequence is known as a *gradient echo* sequence.

The *inversion time* (TI), employed in *inversion recovery* sequences, is the time between the 180° inversion pulse and a 90° readout pulse that converts the recovered longitudinal magnetisation to transverse magnetisation. Subsequently, an additional 180° pulse is required at TE/2 to refocus the transverse magnetisation and generate the echo of the readout pulse. Careful selection of the TI may be used to nullify the signal of certain tissues, and is selected according to the T1 relaxation time of the undesired tissue.

2.2.3 Spatial localisation

MR signal localisation is achieved through the use of magnetic field gradients superimposed over the main field B_0, that induce position-dependent changes in precessional frequency and phase of the spins within that gradient. Magnetic field gradients are produced within the magnet bore by a 3-axis gradient system (figure 2.6), wherein three

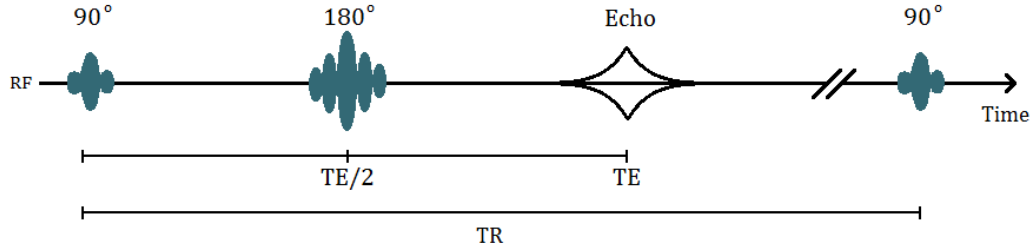

FIGURE 2.4: Spin echo pulse sequence diagram, demonstrating the repetition time TR between excitation pulses and the echo time TE. A 180° pulse is applied at time TE/2 to produce the echo at TE. Figure adapted from (T. R. Melzer, 2011).

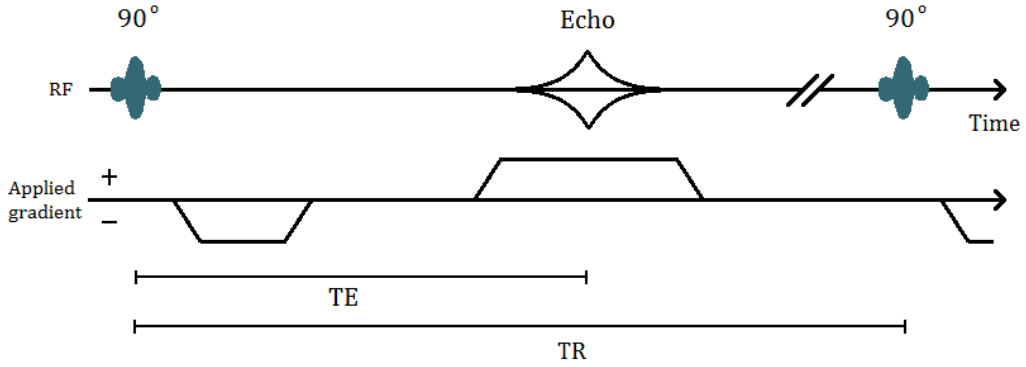

FIGURE 2.5: Gradient pulse sequence diagram, demonstrating the creation of an echo using reversed polarity magnetisation gradients. The magnetisation gradients decrease or increase the precessional frequency of the spins depending on their spatial position within the gradient, causing rapid loss of phase coherence. Phase coherence is re-established using a magnetic field gradient of reversed polarity applied for an equal amount of time, producing an echo. Figure adapted from (T. R. Melzer, 2011).

magnetic coils directed along each of the x, y and z directions produce magnetic gradients G_x, G_y and G_z, which spatially modify the magnetic field within the bore. The magnetic field strength in the z-direction experienced by a spin at position (x,y,z) within this net gradient is thus (T. R. Melzer, 2011):

$$\bar{B} = (B_0 + G_x x + G_y y + G_z z)\hat{z} \tag{2.5}$$

This is useful, as the position of spins within a gradient may be determined by their resultant change frequency and phase. There are three gradients applied over the course of a pulse sequence; the slice select gradient (SSG), the frequency encode gradient (FEG) and the phase encode gradient (PEG).

Slice select gradient - G_z

The slice select gradient is applied concurrently and in the same direction as the RF

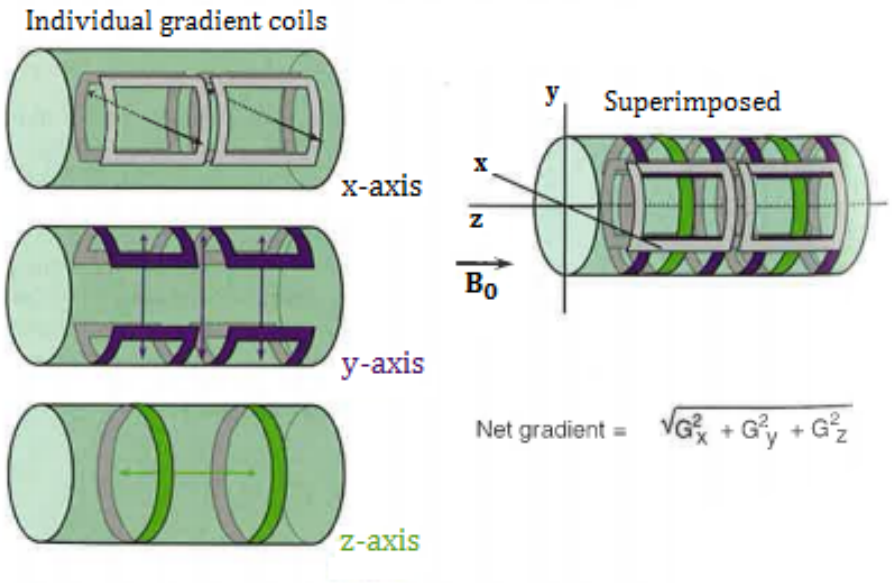

FIGURE 2.6: Orientation of magnetic gradient coils and main magnetic coil within an MR bore. Figure adapted from (Bushberg et al., 2012).

excitation pulse to select an imaging slice in the z-direction. Application of G_z causes a shift in resonant frequency of the spins in the z-direction following the linear variation of the SSG. Given that the RF pulse confers energy only to those spins precessing at the defined centre frequency, the frequency shift will result in spin excitation limited to a specific slice within the SSG. The following equation describes the spatial dependency of the spin resonant frequency (MHz T^{-1}) within the SSG (McRobbie et al., 2003):

$$\begin{aligned} f(z) &= \gamma B(z) \\ &= \gamma(B_0 + z \cdot G_z) \end{aligned} \tag{2.6}$$

The width of the slice is determined by the strength of the magnetic gradient across the field of view and the bandwidth (BW) of the excitation pulse:

$$width = \frac{BW}{\gamma G_z} \tag{2.7}$$

Thus the same slice width may be achieved using a narrow BW as a wide BW, by altering the SSG strength accordingly. A narrow bandwidth is generally desired, due to the inverse relationship of bandwidth with signal to noise ratio (SNR $\propto \frac{1}{\sqrt{BW}}$). However, the wide slice widths required to image a desired volume would necessitate a low gradient strength, which may result in chemical shift artifacts (Bushberg et al., 2012). The width of the SSG

is thus a matter of trade-off between the desired SNR and the propensity for chemical shift artifacts in the image volume.

Frequency encode gradient - G_x

The frequency encode gradient, or readout gradient, is applied perpendicular to the SSG during the growth and decay of the induced echo. Either of the orthogonal directions may be chosen, but here it is defined in the x-direction as G_X. The FEG causes the precessional frequency of the spins within the selected slice to vary according to their position on the x-axis. Acquiring the signal of the echo simultaneously with application of the readout gradient thus assigns spatial information in the x-direction to detected signal intensities.

Phase encode gradient - G_y

Lastly, the phase encode gradient induces a frequency shift in the y-direction, resulting in a spatially dependent phase-shift when the PEG is turned off and all spins revert to the resonant frequency. Applied prior to signal acquisition, this enables readout of spatial information in y based on the degree of phase shift experienced by the spins. A 'rewinder' gradient of opposite polarity is generally applied after signal acquisition to re-establish phase conditions prior to the next excitation. Multiple PEG steps may be applied with incremental changes in field strength to provide spatial information at different points within the field of view (FOV) (Bushberg et al., 2012).

2.3 Factors affecting image quality in MR

Spatial resolution, SNR and contrast to noise ratio (CNR) go hand in hand in terms of MR image quality, and a great deal of parameter juggling is often required to find the optimum balance. SNR is generally regarded as the greatest limiting factor in MRI, dependent on the choice of pulse sequence, voxel volume, field of view (FOV), slice width, phase and frequency encode matrix size, number of signal averages, RF bandwidth and receiver coil quality. Many of these parameters are also directly related to spatial resolution and contrast sensitivity.

It is easiest to examine the interplay of these factors by looking at the maths involved. The CNR of two tissues A and B in a sample image is dependent on noise in the image and the difference in signal intensities S_A and S_B, such that:

$$\mathrm{CNR}_{AB} = \frac{S_A - S_B}{noise}$$

Both CNR and SNR are thus inherently dependent on the factors determining signal and noise in MR. The signal achievable in a particular sequence is primarily dependent on spatial resolution, and is also scaled by a relaxation factor $F_{sequence}$ specific to the pulse sequence employed. The signal intensity in MR is therefore given by:

$$signal \propto \Delta x \cdot \Delta y \cdot \Delta z \cdot F_{sequence} \tag{2.8}$$

The relaxation factors for spin echo and gradient echo pulse sequences (used in this study) are as follows (McRobbie et al., 2003):

$$F_{SE} \propto \left[1 - e^{(-TR/T1)}\right] \cdot e^{(-TE/T2)} \tag{2.9}$$

$$F_{GE} \propto \frac{sin\alpha \cdot (1 - e^{(-TR/T1)} \cdot e^{(TE/TE^*)})}{1 - cos\alpha \cdot e^{-TR/T1}} \tag{2.10}$$

Both of these factors are dependent on the acquisition parameters TE and TR and the tissue characteristics T1 and T2. When optimising parameters in the pursuit of image quality, TE and TR are usually decided upon first, as they relate directly to the tissue characteristics. The T2* dependence of F_{GE} is a consequence of using applied gradients instead of a 180° inversion pulse to produce an echo, as these do not eliminate transverse magnetisation relaxation caused by magnetic field inhomogeneities.

Noise in MR is proportional to the RF bandwith and inversely proportional to the number of excitations (NEX), the frequency encode matrix size (N_{FE}), and the phase encode matrix size (in two directions for 3D, N_{PE1} and N_{PE2}). Thus, image noise may be expressed as (McRobbie et al., 2003):

$$noise \propto \frac{\sqrt{BW}}{\sqrt{NEX \cdot N_{FE} \cdot N_{PE1} \cdot N_{PE2}}} \tag{2.11}$$

Dividing equation 2.8 by equation 2.11 yields the SNR:

$$SNR \propto \frac{\Delta x \cdot \Delta y \cdot \Delta z \cdot F_{sequence} \cdot \sqrt{NEX \cdot N_{FE} \cdot N_{PE1} \cdot N_{PE2}}}{\sqrt{BW}} \tag{2.12}$$

The SNR can be improved by increasing the voxel size, decreasing the number of excitations and the number of frequency and phase encode steps, or by decreasing the RF bandwidth. However, increasing the SNR by continuing to change these parameters ceases to be beneficial past a certain point, as image artifacts may appear due to other factors.

2.4 Relevant MRI techniques

Pulse sequences

The pulse sequences relevant to this thesis are gradient-recalled echo (GRE) and proton-density weighted fast spin echo (FSE) sequences. These sequences are similar, but differ in that GRE uses applied gradient fields to generate transverse magnetisation rather than a 180° RF inversion pulse.

A modified GRE sequence is used to produce the T1-weighted images for spatial co-registration within subject, while FSE sequences are used in ASL to produce images of labelled arterial blood water and un-labelled controls; the difference between the labelled and control images is then used to calculate a quantified measure of cerebral blood flow.

2.4.1 Structural T1 weighted MRI

T1-weighted acquisitions such as 3D spoiled gradient recalled echo acquisition (3D SPGR) typically have a short TR and short TE, to maximise the differences in T1 characteristics of tissues and minimise the differences in T2 characteristics (see figure 2.7). Due to the short TR, T2* effects dominate and allow a build up of transverse magnetisation to occur in tissues with long T2 times. These steady-state contributions are prevented in 3D SPGR by introducing a semi-random phase change in subsequent RF excitation pulses in the acquisition. This shifts the residual transverse magnetisation components out of phase, preventing build up of the transverse steady-state signal and effectively removing T2* effects from the acquisition(Bushberg et al., 2012, Chapter 12). This leaves a T1-weighted image with 1 mm isotropic resolution and good contrast rendition of grey and white matter acquired over a very short TR, with very low contribution from CSF.

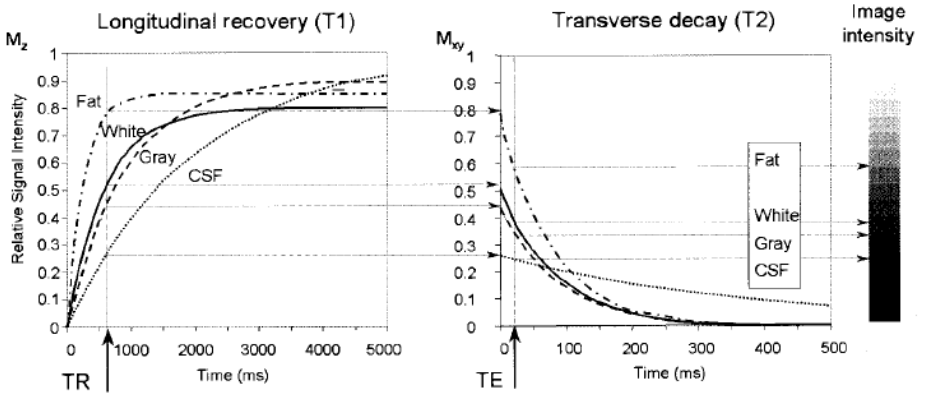

FIGURE 2.7: T1 weighting is achieved using a relatively short TR to maximise signal differences from T1 characteristics, and a short TE to minimise transverse decay. Figure adapted from (Bushberg et al., 2012).

2.4.2 Proton density weighted MRI

Proton density weighted MR imaging highlights the differences in the number density of protons in magnetised tissues. This is done by minimising the differences in signal caused by the T1 and T2 characteristics of the different tissues in the imaging slice (see figure 2.8). Choosing a long TR allows the longitudinal magnetisation to recover for all tissues, thus reducing the effect of T1 characteristics. Choosing a short TE minimises T2 and T2* effects as it does not allow enough time for significant transverse magnetisation decay to occur.

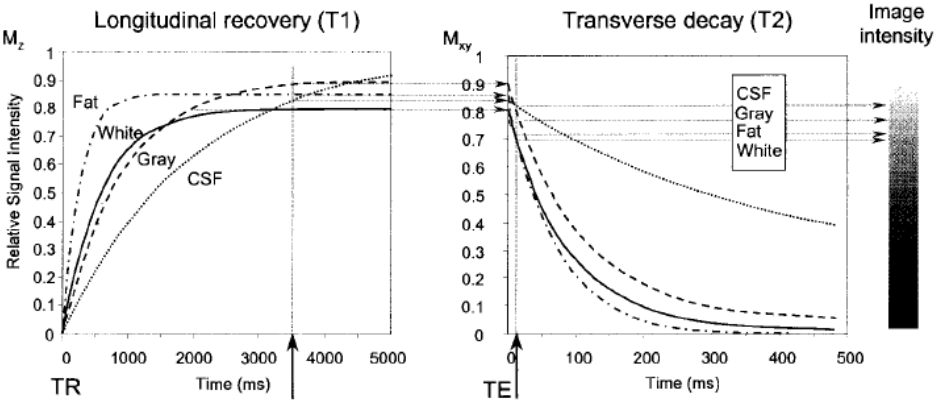

FIGURE 2.8: Proton density weighting is achieved using a long TR to minimise signal differences from T1 characteristics, and a short TE to minimise T2 (transverse decay) influence. Figure adapted from (Bushberg et al., 2012).

2.4.3 Arterial Spin Labelling

Arterial spin labelling (ASL) has previously been mentioned as a non-invasive method for quantitative measurement of perfusion, eliminating the need for potentially harmful exogenous or intravenous radiotracers such as those used in PET imaging (Dai et al., 2008).

ASL methods acquire perfusion data through the use of external RF and magnetic field gradient pulses applied across a chosen labelling plane. The RF and gradient pulses invert the magnetic spins of water molecules in the feeding arteries within the labelling plane, which then flow into the imaging volume. The longitudinal magnetisation of the tagged blood water entering the image volume acts in the opposite direction to the non-labelled tissue magnetisation M_0, causing a reduction of the longitudinal magnetisation in that region. Areas of high perfusion thus see a greater reduction in signal. The difference between this tagged image and a proton-density weighted image acquired without any labelling is used to produce a quantified measure of the cerebral blood blow through the volume. The quantification process will be detailed further in Chapter 4.

There are several methods in use to carry out ASL, which mainly differ in the way the in-flowing blood water is labelled. Pulsed ASL (PASL) uses a single RF pulse to invert the the spins in the blood water volume that will flow into the imaging field, while continuous ASL employs a continuous RF field across the labelling plane, inverting spins through flow-driven adiabatic passage. Continuous labelling offers better signal-to-noise ratio (SNR) than pulsed ASL, but suffers from reduced efficiency, lack of multi-slice imaging capability and the mechanical limitations of standard MR hardware preventing continuous-mode operation of RF pulses (Dai et al., 2008). This study employs a modification of CASL using pulsed RF and gradient fields (pseudo-continuous ASL), and is able to achieve the flow-driven adiabatic inversion strategy without the need for specialist hardware.

There are some disadvantages associated with ASL, including relatively low signal acquisition over a long scan time and large voxel sizes, resulting in a relatively low SNR achievable using ASL. ASL is also sensitive to state changes (opening/closing eyes, caffeine ingestion etc.), which may introduce variation across the subject data. This variation cannot be corrected for in this study as information regarding such state changes was not acquired. Additionally, vascular differences between subjects may result in incorrect timing of signal acquisition when using a constant delay time between labelling and acquisition. These

factors, while not inconsiderable, do not outweigh the potential benefits of non-invasive perfusion imaging using MRI.

Chapter 3

Study Design and Participants

Why study PD-MCI?

Patients with worsening cognition in the category of PD-MCI are considered to have high risk of conversion to PDD, however dementia onset is still variable within this group. It is possible that those at greater risk of conversion within the greater PD-MCI group may display certain pathological differences, evidenced by changes in cerebral blood flow. Participants were therefore selected from the wider progression study based on the fulfilment of the requirements for mild cognitive impairment, following completion of a comprehensive neuropsychological battery. These tests across five cognitive domains determine whether the individual has PD with normal conition (PD-N), mild cognitive impairment (PD-MCI) or dementia (PDD). Only those individuals who fell into the PD-MCI category, as defined by the *Movement* Disorders Society Task Force (*M*DSTF) Level II criteria (Litvan et al., 2012), were included in the initial cohort, however the study was extended to include PD-N and PDD patients after additional funding was secured. This chapter gives an overview of the methods employed at the NZBRI to determine the subject group and the overall study design.

3.1 Neuropsychological battery

The five cognitive domains examined are executive function, attention and working memory, learning and memory, visuo-spatial performance and language. The results of each

test are given in terms of z-score, or the number of standard deviations of the result from the mean in age, education, and gender normative data for that test.

Impairment on neuropsychological tests is demonstrated if the patient scores at least 1.5 standard deviations (SDs) below normative data, as per the methods described by (Wood et al., 2016). PD-N is indicated if a patient does not meet this impairment criteria from the results of neuropsychological testing, and does not report significant change in cognition. Scoring 1.5 SDs below normative data in two tests within a single domain is sufficient to classify the patient as PD-MCI. Significant impairment sufficient for diagnosis of PDD is demonstrated if the patient scores at least 2 SDs below normative data in any single test within two of the five domains, and also has impaired daily living as indicated by their significant other. An individual may satisfy the impaired test requirements for PDD but still be classified as PD-MCI if they can still function in daily life unassisted, however this is unlikely. The impaired daily living tests consist of questions answered by the individual's significant other.

The tests included within each domain are given in table A.1. Secondary measures of cognition are provided by the Montreal Cognitive Assessment (MoCA, a global cognitive screen), the Dementia Rating Scale (DRS-2), and the Alzheimer's Disease Assessment Scale - cognition (ADAS-Cog) tests, while measures of functional and psychiatric status are provided by Instrumental Activities of Daily Living (IADL), Clinical Dementia rating (CDR) status, Global Deterioration Scale (GDS), Parkinson's Disease Questionnaire (PDQ-39), Neuropsychiatric Inventory (NPI) and Geriatric Depression Scale (GDS) (T. J. Anderson, 2013).

3.2 Study participants

Inclusion Criteria

1. Diagnosis of PD-MCI at baseline, as defined by the level II *M*DSTF criteria (Litvan et al., 2012):
    a) PD according to the UK Brain Bank Criteria;
    b) Gradual decline in cognitive ability reported by patient or caregiver, or observed in serial clinical testing;

c) Cognitive deficits on the neuropsychological test battery consistent with mild cognitive impairment as above;

d) Cognitive deficits not sufficient to interfere significantly with functional independence;

2. Community living with a significant other, who can accompany the patient as an informant.

Exclusion Criteria

Patients were initially excluded from participation in the study based on fulfilment of any of the following criteria (T. J. Anderson, 2013):

1. PD-N at baseline.
2. PDD at baseline, as defined by the MDSTF criteria.
3. Dementia with Lewy Bodies (DLB).
4. Presence of other explanations for cognitive impairment.
5. Other PD-associated comorbid conditions that, in the opinion of the clinician, significantly influence cognitive testing.
6. Prior neurosurgery as treatment for PD.

Note that exclusion criteria 1) and 2) were removed some time after scanning began due funding being awarded to include PD-N and PDD. The inclusion of PD-N and PDD patients in the study will provide a better representation of the full cognitive spectrum present in PD.

Possible participants were recruited from an existing group of PD patients that had previously taken part in a longitudinal study at the NZBRI. At that time, 85 were classified as PD-N, 54 were PD-MCI and 46 were PDD. The 46 PDD patients were automatically excluded, while the PD-N and PD-MCI patients were re-screened using the MoCA test. Those who scored < 28 (100% sensitivity for PD-MCI; 40% specificity) were invited to undergo comprehensive neuropsychological testing to evaluate cognitive status. Additional patients were recruited from public and private PD clinics using the same screening process. Following testing, those who met the inclusion criteria as defined above were

invited to participate in the study. Table 6.1 in the results gives the demographics of the 50 subjects included in this study.

The results of the neuropsychological testing battery for all 50 participants are included in table A.2. This table summarises each domain as an average z-score. The average score across all five domains represents the overall cognitive ability of the participant, hereafter referred to as the cognitive z-score.

3.2.1 Parkinson's disease dementia risk score

Conversion to dementia in PD was previously investigated in a longitudinal study conducted at the NZBRI, following 119 PD patients over 4 years (T. Anderson et al., n.d.). Over this time, 26 subjects developed dementia, with age, MoCA, Stroop Interference, Map Search, and Trails B found to be most predictive of conversion. These assessments were used in a Bayesian probabilistic Gaussian process model to give individualised probabilities of developing dementia within 4 years, forming the Parkinson's disease dementia risk score (PDDRS). The PDDRS displayed a high sensitivity for discriminating between converters and non-converters to dementia within 4 years (AUC=0.92, 95% CI 0.85-0.98).

PDDRS scores are formed for all study participants taking part in the longitudinal conversion study at the NZBRI. This thesis determines if any correlation exists between perfusion changes in the subject group and the PDDRS score, such that the presence of specific regional changes may be used to evaluate the risk of imminent conversion to dementia in future subjects.

3.3 PET and MRI imaging protocols

FBB PET imaging protocol

Amyloid PET scanning was performed at Southern Cross Radiology in Christchurch using a GE Discovery 690 scanner. [^{18}F]Florbetaben (FBB) was employed to image both dynamic brain perfusion and amyloid deposition. Approximately 6.7 GBq of FBB was produced in Melbourne by Cyclotek Pty Ltd and flown to Christchurch for scanning, with a remaining activity of ∼1 GBq, sufficient for three patient doses. Participants underwent 10 minutes of scanning acquired in list mode (continuous acquisition) immediately following injection of 300 MBq (± 20 MBq) of FBB. The raw data was reconstructed using an iterative time of flight plus SharpIR algorithm. A low dose CT scan acquired using the GE scanner immediately prior to PET acquisition enabled attenuation correction of the PET data by the on-board GE software.

T1-weighted structural MRI protocol

Structural brain images were acquired using a T1-weighted, 3D spoiled gradient recalled echo acquisition (3D SPGR, echo time = 2.8 ms, repetition time = 6.6 ms, inversion time = 400 ms, flip angle = 15°, acquisition matrix = $256 \times 256 \times 170$, field of view = 250 mm, slice thickness = 1 mm, voxel size = $0.98 \times 0.98 \times 1.0$ mm^3).

The structural T1-weighted images were used as a gold standard to which all other images in the study were co-registered. As such, these images maintained their initial orientation throughout pre-processing to ensure this co-registration was consistent across all acquired and created images. Accuracy in this step was vital, as any errors in co-registration may have a significant effect on the results of statistical analysis.

ASL MRI perfusion imaging protocol

Quantified whole brain perfusion was acquired by removing background contributions (proton density weighted images) from spiral, fast spin echo images prepared using psuedo-continuous arterial spin labelling (repetition time = 6 s, echo spacing 9.2 ms, post-labelling delay = 1.525 s, labelling duration = 1.5 s, eight interleaved spiral arms with 512 samples at 62.5 kHz bandwidth and 30 phase encoded 5mm thick slices, NEX = 5, total scan time = 6 min 46 s, units: ml/100 g/min) (Dai et al., 2008). These images were acquired with the subject at rest with their eyes closed.

3.4 Image Pre-processing

FBB PET

The summed 10 minute perfusion images, corrected for time-of-flight and attenuation corrected, were co-registered to the structural MR (3D SPGR) images using SPM12, a statistical parametric mapping software package in Matlab[1]. The SPGR image was segmented into grey matter (GM), white matter (WM) and cerebrospinal fluid (CSF) tissue segments. Structural SPGR images were then warped into standardised space using DARTEL (Ashburner, 2007). The images were then smoothed using an 8mm FWHM Gaussian kernel. A possible measure of grey matter perfusion was provided by the standard uptake value ratio (SUVR) image, created by dividing all global grey matter voxel values by the mean of the cerebellar grey matter voxels. SUVR images normalised to global grey matter were also created for use in direct voxel by voxel comparison of FBB derived perfusion and ASL derived perfusion.

ASL MRI

Quantified ASL perfusion images of cerebral blood flow were co-registered, normalised, and smoothed using parameters derived from the structural MRI processing, following the same protocol as the FBB-derived perfusion preprocessing. The mean perfusion measurements for select cortical and sub-cortical grey matter regions were extracted for use in further analysis.

3.5 Statistical analysis

Linear regression

All voxel-wise comparisons and linear regression were performed using a permutation-based inference tool for non-parametric thresholding. For each contrast, the null distribution was generated over 5000 permutations at alpha level α <0.05, correcting for multiple comparisons using threshold-free cluster enhancement (Winkler et al., 2014). Linear regression was employed for both imaging modalities using cognitive z score and PDDRS as regressors, correcting for age and sex. The results of this linear regression were used

[1]http://www.fil.ion.ucl.ac.uk/spm/software/spm12/

to identify whether any significant correlation with cognition or PDDRS exists for either FBB or ASL derived perfusion, and to determine the validity of further enquiry into these measures using network analysis.

Voxelwise comparison

Voxel-based multiple linear regression was used, following the method described above, to assess the spatial association between the two perfusion modalities. This model was used to determine the extent of the spatial association between FBB-derived perfusion and ASL-derived perfusion should it exist. Extracted mean voxel values within select cortical and sub-cortical regions were used to verify the results of the voxelwise comparison.

Network analysis

Voxel-based principal component analysis was used to identify sources of grey matter perfusion variation in the subject data. Logistic regression methods were used to isolate any components shown to correlate significantly with cognition or PDDRS, as per the method described by (Spetsieris et al., 2009). Principal components that were significantly associated with clinical measures of cognition and dementia risk ($p < 0.05$) were used in linear combination to create a cognition-related perfusion network. The reliability of these networks was assessed using a bootstrap estimation procedure and leave-one-out cross validation.

Chapter 4

Pre-Processing Methods

Before any analysis could take place, the PET and MR raw image data were pre-processed to bring all images into the same normalised space, accounting for individual differences in brain shape, size and location in the scanner geometry. The pre-processing steps also attempted to reduce the effect of patient movement during image acquisition.

The raw PET and MRI data for each individual was sent in DICOM format to the NZBRI DICOM store from the servers at Hagley Radiology. Each individual has a PET series number and an MRI series number; these were kept together with the individual's clinical and neuropsychological testing results in an excel spreadsheet. All incoming MRI and PET data was backed up on CD, a dedicated hard-drive, and the NZBRI servers.

4.1 Statistical Parametric Mapping

Pre-processing of PET and MR images for analysis was carried out using SPM12, the most recent Statistical Parametric Mapping software package in MATLAB, designed specifically for the analysis of brain imaging data sequences. The SPM PET graphical user interface (GUI) includes options tailored specifically for spatial pre-processing of PET/MRI images. This GUI can be found in Appendix A. These functions can be run in batches using the SPM Batch Editor and saved for later use. The batches may also be called in MATLAB using the matlabbatch function.

4.1.1 DICOM to NIFTI conversion

Once retrieved from the Hagley workstation, the relevant DICOM files were first converted to single file NIFTI (.nii) format, which contains both image and header information for that individual. This is the format that was used exclusively in pre-processing and analysis. This could be done using DICOM Import in SPM12, or by using the built-in *dcm2nii* application in the Linux window. The DICOM Import routine is designed to convert a set of DICOM files into an SPM compatible 3D image volume, either in separate img and hdr files or as a single NIFTI file. DICOM to NIFTI conversion using SPM was not always reliable for this study dataset, perhaps as a result of the complexity of the DICOM image format or the use of image fields set by the scanner manufacturer which are not recognised by this version of SPM. For this reason, the *dcm2nii* application was used to import and convert the patient data to NIFTI format in this study. While this method requires manual file selection, it is much more reliable, and also gives the option of converting to 4D image volumes.

4.1.1.1 Naming Conventions

The relevant PET and MR images for this study were identified by calling specific elements of the DICOM header information using MATLAB. Header information was obtained using the function *gems_dicominfo.m*. The header element SeriesDescription gave the name of the series as set by the technician prior to acquisition. The required PET series was named '10 Min TOFAC Brain' and gave the average 10 minute attenuation corrected image, corrected for time-of-flight. The required MRI series were named '3D SPGR', '3D ASL (non contrast)' and 'Cerebral Blood Flow'. Conversion of the 3D ASL DICOM files to NIFTI format yielded two separate images, namely the labelled 'difference' image and the non-labelled 'control' image. All imported images were checked visually and labeled for each individual according to their PET and MRI series numbers.

Using the series numbers 15434 (PET) and 38356 (MRI) as an example, the naming conventions were as follows:

- 10 Min TOFAC Brain - 'perf_tofac_15434.nii'
- 3D SPGR - 's_38356.nii'

- 3D ASL - 'control_38356.nii', 'diff_38356.nii'
- Cerebral Blood Flow - 'cbf_38356.nii'

Correct and accurate was important to allow MATLAB scripts to be used to carry out pre-processing. The PET and MR images were placed in dedicated folders for pre-processing, ordered by series number.

4.1.2 Downsampling and Unified Segmentation

The structural MR images were interpolated to a higher resolution by the scanner and therefore required to be downsampled to the acquisition resolution ($256 \times 256 \times 170$). This was done using MATLAB, and creates a 'ds' image against which all other images are spatially aligned. Segmentation of the 'ds' image can then occur.

Unified Segmentation in SPM segmented, bias corrected and spatially normalised each downsampled structural brain image according to pre-defined tissue probability maps and generalised registration models created from averaging many structural brain images. Tissue probability maps (A.4) depicting grey matter, white matter, cerebrospinal fluid, bone, skin and air were imported into the routine and a non-linear deformation field was applied to best fit the map to each individual. Generalised registration information for each tissue was included to provide prior information on the tissue locations based on images from other subjects, rather than assuming stationary prior probabilities based on mixing proportions (Ashburner et al., 2015).

Segmentation was carried out separately for each individual, with one input ds image per segmentation. The routine was defined to output a native tissue class image for each of the selected tissues, with the prefixes 'c1ds' to 'c5ds'. These are the images of the distribution of each tissue type specific to the input 'ds' image and thus retain the same dimensions. For grey and white matter, these images were also given in a form that was later used within the Dartel toolbox in spatial normalisation ('rc1ds' and 'rc2ds' for grey and white matter respectively). The 'dartel imported' images provided the first estimation for size to use in the normalisation of PET FBB to MRI scans (121x145x121).

4.1.3 Coregister - Estimate

Before any statistical analysis could occur, all images across multiple modalities had to be brought into alignment. The fist step in this process was coregistration. Within-modality coregistration was relatively simple, and was achieved using a least squares approach to optimise a 6 parameter rigid body spatial transformation (Ashburner et al., 2015). The 6 parameters of the affine transformation were estimated to best match each successive input image to the selected reference image. The 'goodness of fit' of the transformation in spatially matching the images was based on an objective optimization function or matching criterion, in this case the mean squared difference between the images. For between-modality registration, a rigid body transformation within subject required more complex matching criterion. The SPM routine Corgister - Estimate used a registration method based on information theory introduced by Collignon et al. (1995). This method employs mutual information (MI) of voxel pairs as matching criterion, where MI is a measure of the mutual dependence of two variables and is assumed to be maximised when the two images are in register. The MI, also known as Shannon information, of two random variables X and Y is given by:

$$S(X;Y) = \sum_{x,y} p(x,y) log\left(\frac{p(x,y)}{p(x)p(y)}\right) \tag{4.1}$$

where p(x,y) is the joint probability distribution function of intensities of X and Y, and p(x) and p(y) are the marginal probability distribution functions of intensities of X and Y respectively. S(X,Y) is zero when the two images are completely independent of each other and maximised when they are completely inter-dependent, such that there exists a one-to-one mapping of the voxels in each image. This can also be thought of as zero dispersion between the 2D grey-value histograms of the common voxel pairs of each image when the images are in perfect register (Collignon et al., 1995). In multi-modality registrations the images will rarely be completely inter-dependent. The MI objective function was maximised by 6 rigid body parameters determined using Powell's method for optimisation (Press, Teukolsky, Vetterling, & Flannery, 1992). In order to obtain faster convergence, the images and the histogram were smoothed slightly by the routine to make the cost function as smooth as possible (Ashburner et al., 2015). This also reduced the chance of the algorithm getting caught within local minima.

There are three input options that designate the reference image and the images to be brought into register. The 'reference' image remains fixed in it's original orientation, while the 'source' image is spatially transformed to best fit the reference image. 'Other' images may be selected to remain in alignment with the source image. The T1-weighted SPGR images were used as the reference images for co-registration, to which all other images were aligned. Coregistration was run separately for each source image, of which there were two: the PET 10 minute TOFAC image and the control image obtained by ASL MRI. The CBF and difference images were defined as 'other' images to remain in alignment with the control image. The routine realigned the original images rather than creating new ones, and registration parameters were stored in the headers of the coregistered images.

4.1.4 Dartel Normalisation and MNI space

Dartel (Diffeomorphic Anatomical Registration Through Exponentiated Lie Algebra) is a method for between-subject registration based on the application of a single computed flow field for each individual, considered to be constant in time. The Dartel algorithm takes one or two images, in this case the grey and white matter Dartel images created during segmentation, and warps them to a set of standard brain templates. The deformation applied to the images is output as a flow field that may be used to warp the scans for that individual to normalised space, in this case the average brain coordinate system defined by the Montreal Neurological Institute, known as MNI space. The MNI standard brain was defined by averaging a large number of MRI scans of normal controls in order to create a standard space that was representative of the population. The previously used standard brain was defined from the dissection of a single human brain by the neurosurgeon Jean Talairach, who formed the well known Talairach Atlas. The current standard MNI template used in this study is ICBM152 (figure 4.1), an average brain template of 152 MRI scans of normal brains registered by a 9-parameter affine transformation to the previous MNI template, MNI305[1] (created from the average of 305 normal brains registered to the Talairach Atlas). MNI space has largely replaced Talairach coordinates as the standard template for brain image normalisation.

In this step, the dartel grey and white matter images created during segmentation were used within Dartel to create a flow field for each individual ('u_rc1ds'). The ICBM152 grey

[1] http://www.nil.wustl.edu/labs/kevin/man/answers/mnispace.html

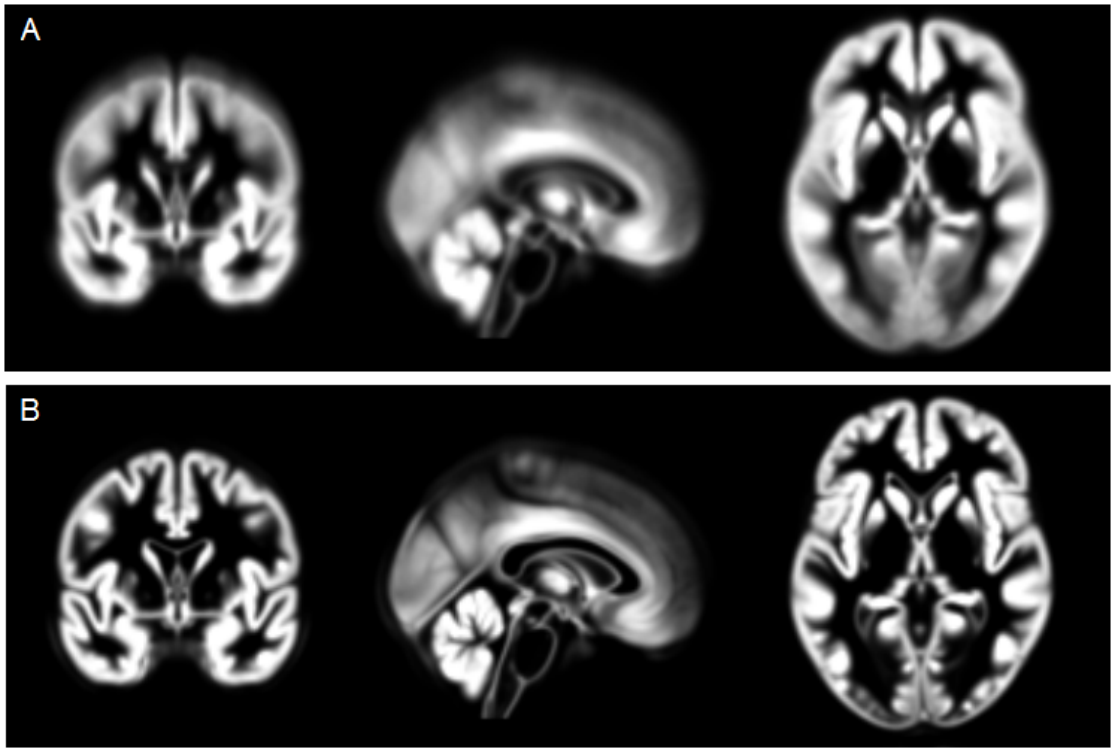

FIGURE 4.1: Two of the ICBM152 grey matter tissue templates, depicting a) the smoothest template used in the first outer iteration and b) the sharpest template used in the final outer iteration. The templates also contain standard white matter images (not shown).

matter tissue templates were selected and used at each outer iteration, starting relatively smooth and becoming steadily sharper with each iteration. The earlier iterations required more regularisation to ensure the deformations were smooth, while the later iterations applied less to give closer matching of details (Ashburner et al., 2015). The created flow fields were applied after quantification to warp the processed scans into the same normalised space.

4.1.5 Quantification of ASL Cerebral Blood Flow

Once the control and difference images given by the ASL acquisition were coregistered to the structural (ds) image, they were then used to give a quantified image of the cerebral blood flow (CBF) (4.2).

The quantification of the CBF images is based on the equation:

$$cbf = 6000 \cdot \left(\frac{\lambda \cdot \left(1 - e^{(-2/1.2)}\right) \cdot e^{(w/T1)}}{2 \cdot T1 \cdot \left(1 - e^{(-1.5/T1)}\right) \cdot \epsilon} \right) \cdot \left(\frac{diff}{(g \cdot nex) \cdot cont} \right) \tag{4.2}$$

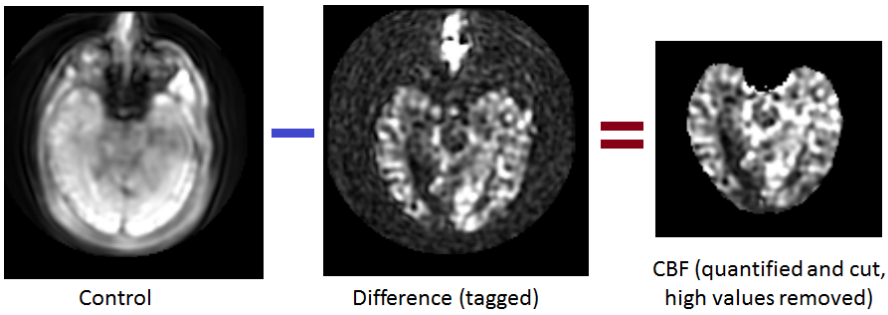

FIGURE 4.2: A very simple representation of the ASL quantification process. The difference between the control and tagged image given by ASL yields a quantified measure of perfusion, cut to include only the brain volume. This process includes the consideration of many factors not represented here.

where λ is the brain-blood partition coefficient of water, set to the whole brain average of 0.9; w is the post-labelling decay time, set to 1.525 seconds; $T1$ is the spin-lattice relaxation time of blood, set to 1.6 seconds at 3T; ϵ represents the combined efficiency of labelling and suppression in the acquisition sequence, defined as 0.8*0.75; the constants 1.5 and 2 represent the labelling and background saturation/suppression time in seconds respectively, with the suppression time corrected for the T1 time of grey matter (1.2 seconds); $diff$ and $cont$ are image matrices containing the voxel values of the difference and control images; NEX is the number of excitations or signal averages, set to 5. The quantified perfusion values were scaled by a factor of 6000 to convert L/kg/s to ml/100g/min.

The quantified perfusion images were cut according to an extracted brain mask, acquired using the Brain Extraction Tool (BET) (Smith, 2002) within the FMRIB Software Library (FSL) (Jenkinson et al., 2012). The thresholding parameters were modified for each individual following an initial check of the mask - the mask was made more stringent if too much undesired tissue (skull, eyes) remained, and less stringent if the initial mask cut regions of cerebral grey matter and cortical ribbon.

Extremely high artefactual voxel values were then *eliminated* from the *quantified* and *cut* CBF images, yielding the final perfusion image for each individual. Using the same scan number as before as an example, these images were thus named 'ecqCBF_38356.nii'. Figure 4.2 demonstrates the typical appearance of the control, difference and quantified CBF images.

4.1.6 Warp to normalised space

The 'create warped' batch within SPM contains input fields for the dartel flow field and the images to be warped, and allows warping with and without modulation. This modulation allows the spatially normalised images to be rescaled by the Jacobian determinants of the deformations (Ashburner et al., 2015).

The quantified and cut CBF images and the coregistered FBB tofac images were warped using the subject-specific flow fields generated by the Dartel routine (see section 4.1.4). The dartel grey matter (c1ds) images created during segmentation were also warped to MNI space, as they were used in the next step to normalise the grey matter intensities in the FBB and ASL images to the cerebellar grey matter (FBB) and global grey matter (both FBB and ASL). The images were input separately into the 'create warped' batch, selecting warp with modulation for the dartel grey and white matter images and no modulation for the ASL and FBB images.

4.1.7 Normalise to Cerebellum and global grey matter

Images of the standard uptake value ratio (SUVR) from the 10 minute FBB TOFAC images were created in this step. The same process was used to normalise both the TOFAC and the ecqCBF images to the whole brain grey matter for use in voxelwise analysis.

A standard brain mask of the reference region was input and combined with the subject-specific grey matter image (c1ds) to form a mask of the grey matter within the reference region for that subject. This mask was used to obtain mean values within this region from the selected image to be normalised. Prior to normalisation, any voxels not containing a signal intensity value were set to zero. These 'not-a-number's arose in the outer edges of the image matrix as a consequence of coregistration. The normalised images were created by dividing the input image by the extracted mean voxel value in the reference region, and were then smoothed using an 8mm Gaussian smoothing kernel. Smoothing was necessary in order to reduce the proportion of residuals exhibiting non-normal distribution, such that parametric methods could be used in statistical analysis (T. R. Melzer et al., 2012). Smoothing also helps to account for slight image misalignment, as may still be present despite pre-processing and coregistration. The amount of smoothing applied is a matter

of trade-off between spatial resolution and normality of the data. Residuals, parametric methods and non-parametric methods are discussed in section 5.1.

FBB TOFAC images were normalised to grey matter in the cerebellum and global grey matter, creating two different SUVR images (denoted FBB_{cer} and FBB_{GM} for clarity). The ecqCBF images from ASL were either left un-normalised (ASL_{non}) or were normalised to global grey matter (ASL_{GM}). Measures relative to global grey matter were created for both FBB and ASL datasets in order to allow direct voxelwise comparison in later analysis. Global grey matter was chosen for this purpose as the ASL data could not be normalised to the cerebellum, as values within this region may be missing or unreliable due to the geometry of the acquisition (T. R. Melzer, personal communication). The FBB_{GM} and ASL_{GM} data will not be used in linear regression with cognition as they may contain bias associated with systematic global reductions.

4.1.8 Convert 3D to 4D

The final pre-processing step was more a matter of convenience than necessity. The perfusion images of the 50 subjects, having been coregistered, quantified, warped, normalised and smoothed, were grouped by order of MRI series number and combined into a 4D file using SPM's 3D to 4D batch option. This enabled easy selection of the images for use in analysis.

The filenames of the pre-processed data are summarised in table 4.1.

TABLE 4.1: Pre-processed image data filenames, in 3D, 4D and abbreviation (to be referred to henceforth).

3D file name	4D file name	Abbreviation
ssuvr_wperf_tofac_(scan#).nii	AB_FFBperf_4D.nii	FBB_{cer}
ssuvr_GMnorm_wperf_tofac_(scan#).nii	AB_FFBperf_GMnorm_4D.nii	FBB_{GM}
swecqCBF_(scan#).nii	AB_ASLperf_4D.nii	ASL_{non}
swecqCBF_GMnorm_(scan#).nii	AB_ASLperf_GMnorm_4D.nii	ASL_{GM}

Chapter 5

Analysis Methods

A common issue with tracer-based imaging modalities, such as FBB PET, is the prevalence of noise in the data due to absorption or scatter effects within tissues, reducing the proportion of true coincidences detected. Development of faster scintillation materials and optimised detector systems has helped to increase the signal-to-noise ratio (SNR) of PET, however it is still an inherently noisy modality. ASL MRI suffers from relatively low difference in signal between the labeled and control image frames, acquired over a shorter period of time than PET. While increasing SNR, the use of larger voxels in ASL also has the effect of decreasing image resolution. Methods of statistical analysis must then be employed that are powerful enough to extract significant results, regardless of low SNR or image resolution. Additionally, PET and MRI data have high dimensionality, with each image composed of around 10^5 voxels on average. High dimensionality of samples combined with low sample sizes is generally undesirable, as it limits simple exploration of the data and makes discerning trends difficult.

This chapter details various methods of statistical analysis that were used to make meaningful inferences about the data, accounting for high data dimensionality. The implementation of linear regression and voxelwise regression analysis using the general linear model is discussed, as is correction for multiple comparisons. This type of analysis was used to determine the extent of any spatial correlation between FBB derived perfusion and ASL derived perfusion, and any regions of abnormal perfusion that related significantly to cognitive z-score or PDDRS in either imaging modality. Data reduction is also discussed as a method of separating relevant characteristics from noise. This thesis employed

principal component analysis (PCA) to extract components of image variance that were significantly related to cognition or PDDRS, from which perfusion networks were formed.

5.1 The General Linear Model - Background

The general linear model (GLM) refers to a group of statistical analysis methods centred on inferential tests of hypothesis or analysis of variance (Friston et al., 2007). The GLM is alternately known as analysis of variance or multiple regression analysis, and may be used to carry out a number of types of analyses; these include simple t-tests, one-way ANOVA or more complex correlation and linear regression analyses. While the GLM subsumes many different processes for statistical inference, they are all mathematically similar.

5.1.1 Mathematical basis of the GLM

The core idea behind the GLM is that an observed response variable Y may be expressed in terms of a linear combination of independent explanatory variables X, weighted by an optimised coefficient β, plus a well behaved error term ϵ, usually representative of noise in the dataset (Friston et al., 2007). The basic form of the GLM for the i^{th} observation in Y, in the case of p multiple regressors, is as follows:

$$Y_i = \beta_0 + \beta_1 X_{i,1} \cdots + \beta_p X_{i,p} + \epsilon_i \tag{5.1}$$

where β_0 is a dummy variable providing an intercept. This equation can be visualised as yielding a plane in p-dimensional space, known as the regression surface. The objective of linear regression is to fit a regression surface to the observed surface through a linear combination of the independent variables, such that the difference between the regression surface and the observed surface is minimised by the least squared difference between them. The deviation between two points in the regression and observed surfaces is called the residual value.

The goal is thus to compute the coefficient values that minimise the residuals, achieving the best fit of the regression surface to the observed surface. The model can be written in matrix form as in Rawlings et al. (1998), where $\mathbf{Y}$ is a $1 \times n$ column of observations on the

dependent variable, $\mathbf{X}$ is a $n \times (p+1)$ matrix of observations on the independent variables, $\boldsymbol{\beta}$ is a $(p+1) \times 1$ column vector including the intercept and p correlation coefficients to be estimated, and $\boldsymbol{\epsilon}$ is a $n \times 1$ vector of well behaved error terms. Thus:

$$\mathbf{Y} = \boldsymbol{\beta}\mathbf{X} + \boldsymbol{\epsilon} \tag{5.2}$$

or:

$$\begin{pmatrix} Y_1 \\ Y_2 \\ \vdots \\ Y_n \end{pmatrix} = \begin{bmatrix} 1 & x_{1,1} & x_{1,2} & \dots & x_{1,p} \\ 1 & x_{2,1} & x_{2,2} & \dots & x_{2,p} \\ \vdots & \vdots & \vdots & \ddots & \vdots \\ 1 & x_{n,1} & x_{n,2} & \dots & x_{n,p} \end{bmatrix} \begin{pmatrix} \beta_0 \\ \beta_1 \\ \vdots \\ \beta_p \end{pmatrix} + \begin{pmatrix} \epsilon_1 \\ \epsilon_2 \\ \vdots \\ \epsilon_n \end{pmatrix}$$

Note that the first column of $\mathbf{X}$ is populated by ones, providing the intercept β_0. The matrix $\mathbf{X}$ is a matrix of known constants, $\boldsymbol{\beta}$ is a vector of unknown constants, and $\mathbf{Y}$ and $\boldsymbol{\epsilon}$ are vectors of random variables. $\mathbf{X}$ is known as the design matrix, and contains all available knowledge about experimentally controlled factors or confounds, and determines the form the analysis will take (t-test, linear regression, etc.). Within $\boldsymbol{\beta}$ containing elements $j = 0, \dots, p$, each element $\boldsymbol{\beta_j}$ can be regarded as a partial correlation coefficient relating the independent variable or confound X_j to the corresponding element of the dependent variable Y_j, providing the other elements of the independent variable remain constant (Rawlings, Dickey, & Pantula, 1998). Regarding the error terms, it is common to assume that the elements $\boldsymbol{\epsilon_j}$ are identically and independently distributed (IID assumptions), with a variance of σ^2. Under these assumptions, the probability density function of the errors follows a Gaussian distribution, thus having spherical iso-contours. Errors following this assumption are said to obey sphericity. Non-sphericity in the data arises due to regional changes in error variance and interdependencies within the error terms, and are typically accounted for by introducing variance and smoothness estimators within the model (Friston et al., 2007).

Looking at equation 5.2, it follows that for some estimate of the correlation parameters $\widehat{\boldsymbol{\beta}}$, the random errors or residuals of the model e are given by the difference between the predicted values and the observed output values:

$$e = \mathbf{Y} - \mathbf{X}\widehat{\boldsymbol{\beta}}$$

A solution may be obtained by minimising the sum of the squared residuals with respect to some estimate of the correlation parameters $\widehat{\boldsymbol{\beta}}$ - in other words, forming the normal equations for the model. By definition, these equations minimise the sum of the square differences between the left and right sides of equation 5.2. The process is known as Ordinary Least Squares estimation (OLS), and assumes error sphericity. The first step is to derive a relationship for the sum of the squared residuals $\sum e_i^2$, which will then be minimised with respect to $\widehat{\boldsymbol{\beta}}$. It is useful to realise that $\sum e_i^2$ is equal to the inner product of the error vector with itself, $e'e$:

$$\begin{aligned}\sum e_i^2 = e'e &= (\mathbf{Y} - \mathbf{X}\widehat{\boldsymbol{\beta}})'(\mathbf{Y} - \mathbf{X}\widehat{\boldsymbol{\beta}}) \\ &= \mathbf{Y'Y} - \mathbf{2}\widehat{\boldsymbol{\beta}}\mathbf{'X'Y} + \widehat{\boldsymbol{\beta}}'\widehat{\boldsymbol{\beta}}\mathbf{X'X}\end{aligned} \tag{5.3}$$

Minimising equation 5.3 with respect to $\widehat{\boldsymbol{\beta}}$, using the vector differentiation identity $\frac{\partial x'x}{\partial x} = 2x$, yields the normal equations for the relationship 5.2 in matrix form:

$$\begin{aligned}\frac{\partial}{\partial \boldsymbol{\beta}}[e'e] &= 0 \\ &= -2\mathbf{X'Y} + 2\widehat{\boldsymbol{\beta}}\mathbf{X'X} \\ \therefore \mathbf{X'Y} &= \widehat{\boldsymbol{\beta}}\mathbf{X'X}\end{aligned} \tag{5.4}$$

Solving equation 5.4 yields the correlation parameters $\widehat{\boldsymbol{\beta}}$ relating the covariates to the observed data, and is thus the relationship underpinning regression analysis. A unique solution to the normal equations exists only if the matrix $\mathbf{X}$ is of full column rank (contains no linear dependencies) such that the inverse $\mathbf{X'X}$ exists. The normal equations are always constant, thus an estimate of the solution will take the form

$$\widehat{\boldsymbol{\beta}} = (\mathbf{X'X})^{-1}(\mathbf{X'Y}) \tag{5.5}$$

This yields an estimate of the coefficient values $\widehat{\boldsymbol{\beta}}$ that may be used to construct an estimate of the regression surface $\widehat{\mathbf{Y}}$, as given by:

$$\widehat{\mathbf{Y}} = \mathbf{X}\widehat{\boldsymbol{\beta}} \tag{5.6}$$

It is clear that the GLM is heavily dependent on the form of the design matrix $\mathbf{X}$, wherein the columns of explanatory variables correspond to experimental confounds or covariates, to be removed or examined by the model respectively. Columns are defined as confounds or components of interest by the form of the contrasts applied within the GLM. For example, a linear regression of the perfusion data with subject cognitive score may be performed removing any variation in voxel intensity related to age and sex, as these are known confounds in brain perfusion. Within a contrast C1, assigning a value of 0 to the columns containing subject age and sex will remove any related experimental effects. Assigning the component of interest, in this case cognitive score, a value of +1 will direct the GLM to search for any positive correlation with that covariate. Significance on the contrast C1 would thus indicate a positive correlation of the data with cognitive score, accounting for age and sex. Similarly, assigning -1 to the covariate column will direct the GLM to search for any negative correlation with cognitive score. The GLM determines the appropriate statistical test based on the form of the design matrix and contrasts.

5.1.2 Parametric and non-parametric statistical inference

This study used both parametric and non-parametric methods for statistical inference. The difference between the two rests on certain distributional assumptions (or lack thereof) made by each method, the fulfilment of which affects the power of each method to obtain significant results. Parametric methods assume that the data and model residuals come from a population that follows a Gaussian probability distribution, described by a fixed set of parameters. Non-parametric methods do not make distributional assumptions and allow these parameters to change, and thus may supervene in terms of sensitivity when distributional assumptions are violated. This may occur when degrees of freedom are small and voxel sizes are large in relation to smoothness. Should the assumptions remain true, parametric methods yield greater accuracy and sensitivity and require less computing power, but are regarded as somewhat less robust in a general sense.

5.2 The General Linear Model - Implementation

Implementation of the GLM was accomplished using robust Biological Parametric Mapping (BPM) (Casanova et al., 2007), SPM (Friston et al., 2007), or FSL's Randomise function (Winkler et al., 2014). The choice of method was dependent on the type of analysis being carried out. BPM is a software package developed to be used specifically in multi-modal image analysis, and was used in this study to carry out direct voxelwise correlation analysis between FBB_{GM} and ASL_{GM} image data. SPM was used to run simple linear regression analysis of the FBB_{cer} and ASL_{non} data with discrete explanatory variables (EVs) and confounds. FSL was used to carry out both voxelwise and correlation analysis, and differs from BPM and SPM in the use of non-parametric methods and permutation testing in order to make inferences about the data. Traditional BPM is closely integrated with SPM, and as such both employ parametric methods to carry out analysis.

All three methods required corrections to be made for multiple comparisons. Depending on the image resolution, a typical MR image may contain hundreds of thousands of voxels, with an associated statistical inference at each voxel. The significance level is set to $\alpha = 0.05$ for most statistical tests, corresponding to a 5% probability of incorrectly rejecting the null hypothesis and falsely identifying a voxel as significant. While this is acceptable in the analysis of small datasets, this translates to potentially thousands of false-positives when making many comparisons across MR images. False-positives resulting from multiple comparisons were dealt with by controlling either the family-wise error rate (FWE) or the false discovery rate (FDR) through various methods, discussed here. FWE controls the expected *absolute number* of false positives, while FDR controls the expected *fraction* of identified positives that may be false (T. R. Melzer, 2011). FWE is therefore more stringent, but may result in some loss of true positive results.

5.2.1 FSL

FSL corrects for FWE, or the chance of one or more false positives, by making use of spatial neighbourhood information surrounding significant voxels in conjunction with permutation testing. Threshold-free cluster enhancement (TFCE) presents the significant voxels in terms of the extent of cluster-like spatial support surrounding it, without the prior definition of a cluster-forming threshold (Smith & Nichols, 2009). FSL obtained voxelwise

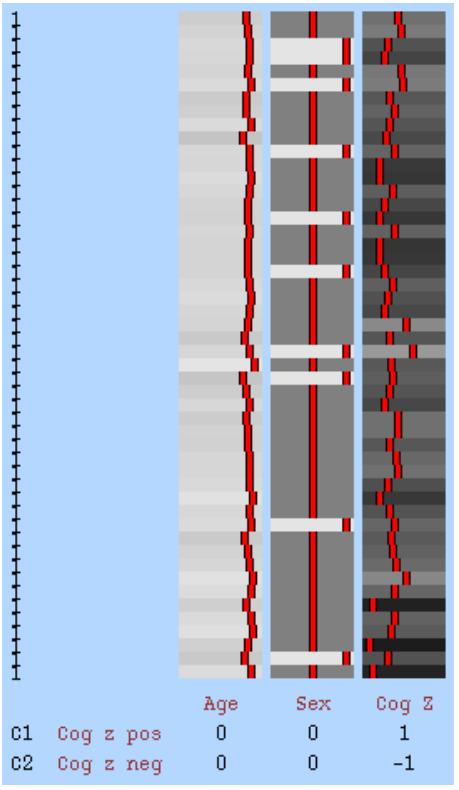

FIGURE 5.1: This design matrix, created using FSL's GLM graphical user interface, specifies cognitive z-score as the tested effect, with age and sex (binary: F=1, M=0) as the confound effects. The applied contrasts direct the GLM to search for a positive or a negative correlation of the data input into Randomise with the tested effect. Testing correlation of perfusion with PDDRS used a design matrix of the same form, with PDDRS as the tested effect instead of cognitive z-score. The design matrix was the same for both FBB and ASL related perfusion analysis.

p-values for the data by repeating the TFCE statistic over a set number of permutations, employing resampling without replacement at each permutation using the Randomise function (Winkler et al., 2014). In this way, cluster-like structures were enhanced while the image remained fundamentally voxelwise (Webster, 2015).

The Randomise function carries out permutation testing based on several input parameters and a specified design matrix. Figure 5.1 demonstrates the design matrix used in this thesis to carry out linear regression analysis of the image data with cognitive z-score, accounting for age and sex. The contrasts defined in this matrix directed Randomise to test for positive (+1) and negative (-1) correlation of the data with the tested effect (cognition), taking into account the confound effects (age and sex). Confound-only residuals were formed by fitting the data to the specified confounds alone, which were then permuted to form an estimation of the confound-related signal. The data including the estimated confound signal was then fitted within the GLM, and the TFCE statistic

performed for each voxel, examining those voxels that fall within an applied whole brain grey matter mask. This process was repeated over the desired number of permutations to build a distribution of the voxelwise TFCE statistics under the null hypothesis. The resultant image may be thresholded to view only the voxels that significantly reject the null hypothesis. These voxels are said to correlate significantly with the tested effect for this data, corrected for multiple comparisons.

5.2.2 BPM and SPM

BPM permits voxelwise comparison in neuroimaging by allowing a different design matrix to be tested by the GLM at each voxel; each design matrix contains the tested covariate, defined as the image data at that particular voxel, along with the standard discrete confounds (age and sex) (Casanova et al., 2007). SPM employs the same design matrix at each voxel, and is well applied to linear regression studies involving discrete explanatory variables.

SPM implements the GLM using parametric methods, assuming normal distribution of error terms following the method described in section 5.1.1. The regression is optimised by minimising the least squared difference between the regression surface and the observed surface. Traditional BPM follows this same method. This thesis used an extension of BPM titled robust BPM, wherein the regression was carried out minimising M-estimates of the data rather than the least squared difference (Yang et al., 2011). The M-estimates account for outliers by assuming non-normal distribution of error terms, thus rBPM is a non-parametric method of statistical inference. The regression is carried out by solving the M-estimates using an iteratively re-weighted least squares method (Yang et al., 2011), and thresholded to control the family-wise error rate. Aside from this difference, SPM and robust BPM are closely linked, as BPM relies upon SPM for statistical inference and visualisation.

Statistical inference within SPM was carried out using a two-step method, wherein false positives were controlled by the clusterwise false discovery rate (FDR_c). An initial alpha level of $\alpha = 0.001$ identified those voxels that were significant in the regression according to a P-value of $p < 0.001$, uncorrected for multiple comparisons. The spatial neighbourhood information of these 'significant' voxels was then examined to form a clusterwise FDR_c corrected threshold. This cluster threshold corresponds to an alpha level of $\alpha = 0.05$

(automatically set by SPM), and defines how many voxels a cluster must contain to be termed significant, controlling the FDR. Clusters that survived the FDR_c threshold were said to be significant at $p< 0.05$, corrected for multiple comparisons.

5.2.3 Methods - correlation and regression analysis

1. Both FSL and SPM were used to carry out multiple linear regression analysis with the FBB_{cer} and ASL_{non} image data, where cognitive z-score and PDDRS were tested effects, accounting for age and sex. Individual domain score was also applied in separate linear regression using SPM, providing a break down of the overall cognitive z-score correlation into its constituent domains.

2. Direct voxelwise comparison between FBB_{GM} and ASL_{GM} was initially carried out using FSL, where the ASL_{GM} data were input as a voxel-dependent explanatory variable into the GLM. The design matrix is given in figure A.7. The voxelwise component of FSL's permutation testing method is still undergoing beta testing, thus comparison using robust BPM was also employed using the same form for the design matrix, as an alternative method of voxelwise correlation analysis. The design matrix used within BPM is the same as that used in the previous analysis.

3. Mean values were extracted from a range of cortical and sub-cortical areas using regional brain masks applied to the FBB_{GM} and ASL_{GM} data. The mean regional voxel values were directly compared between the two imaging modalities in support of the voxelwise correlation results given by (1), yielding correlation coefficients and associated P-values for each region.

An example of the command to call FSL's Randomise function, carrying out linear regression using TFCE, is as follows:

- randomise -i AB_FBBperf_4D.nii -o FBB_cog_cor -d cog_age_sex.mat -t cog_age_sex.con -n 5000 -m maskGM_s4_m0wrp1ds_cut.nii -T -D

where -i specifies the input 4D image file; -o specifies the output filename of the correlation image; -d specifies the design matrix file (.mat); -t specifies the contrast file (.con); -n specifies the number of permutations, set to 5000; -m inputs an optional brain mask, here

defined as the global grey matter; -T directs Randomise to employ the TFCE statistic at each voxel; -D directs Randomise to de-mean the data at each permutation. This last parameter is necessary as the mean was not modelled in the design matrix (see figure 5.1).

5.3 Principal Component Analysis

Principal component analysis (PCA) is a data reduction method based on orthogonal linear transformation, wherein a large number of correlated variables are transformed to give a smaller number of uncorrelated principal components. The objective when using PCA is to achieve accurate dimension reduction by extracting a few principal components that describe most of the variance with the least loss of information (Razifar et al., 2009). The expression of these components in varying degrees can reveal statistically independent patterns of perfusion, or networks, within our subjects.

The data is shifted onto an axis that best fits the variance, and a set of uncorrelated eigenvectors are formed to describe the data according to this new axis. The eigenvectors along which the variation in the data is maximal are known as the principal components (Ringnèr, 2008), each of which can be expressed as a linear combination of the original variables in the dataset. Relatively few of these principal components may then be used in linear combination to represent the original samples in the dataset, greatly reducing the number of variables and allowing for more efficient and visually assessable comparison between samples. PCA is best used with data that fits a Gaussian distribution.

5.3.1 Mathematical basis of PCA

Consider the $n \times m$ data matrix

$$X = [x_1, x_2, x_3, ..., x_m]^T \tag{5.7}$$

where the m columns represent each observed voxel value x_i, and each of the n rows represents a different subject (Jolliffe, 2002). The principal components are obtained by extracting the eigenvectors of the sample covariance matrix $C = E\{XX^T\}$, a matrix wherein the element i, j describes the covariance of the i^{th} and j^{th} elements of X. The

principal diagonal gives the variance of each voxel value within our dataset. The transformation is defined by the m-dimensional set of eigenvectors $w_i = (w_1, ..., w_m)_i$ that map each row vector x_i to a new vector $s_i = (s_1, ..., s_n)_i$ such that each individual variable of s_i inherits the maximum possible variance of the columns of X. The principal components are given by

$$s_i = w_i^T X$$

Which can be written in matrix form as:

$$S = WX \tag{5.8}$$

where $S = [s_1, ..., s_n]^T$ and $W = [w_1, ..., w_n]^T$.

5.4 Principal Component Analysis - Implementation

All perfusion images were preprocessed according to the methods described in Chapter 4, additionally applying a study specific grey matter mask to remove any voxels with a $< 10\%$ chance of being grey matter. Image data were then log-transformed and de-meaned twice to remove the group mean and individual mean across all voxels.

The eigenvectors and corresponding eigenvalues of the PET and ASL perfusion datasets were calculated from their covariance matrices by PCA. Scaling each eigenvector by the square-root of its corresponding eigenvalue produced components of unit variance; these were the principal components of the dataset. The inverse scaled eigenvectors indicated the expression of each component in each individual, while the relative size of each eigenvalue quantified the total variance encompassed by that particular spatially fixed principal component (T. Melzer et al., 2011).

The principal components were ordered by how much of the variance they represent, with the first principal component capturing the most variance. The first few principal components may account for a large amount of the total variance in the data, in which case the remaining components may be rejected to reduce dimensionality without significant loss of data (Razifar et al., 2009). The choice of how many principal components to include

in linear regression with cognitive z-score and PDDRS was made based on the amount of variance contained within the components. Those components that represented 67% of the variance were used in a linear regression with cognitive z-score and PDDRS. Perfusion networks relating specifically to these measures were formed by linear combination of the resultant significant ($p< 0.05$) principal components, using the correlation coefficients given by the regression. The networks were then z-scored by removing the mean and dividing by the standard deviation of the group voxel values. The z-score images were thresholded according to $|z| > 1.96$; this relates to an alpha level $\alpha = 0.05$, thus the surviving voxels were deemed to relate significantly to cognition or PDDRS ($p< 0.05$).

The direction of the correlations represented by positive ($z > 1.96$) and negative ($z < 1.96$) voxel loadings were determined by comparing the absolute mean values from the ASL_{non} data within these regions. The extracted mean values from positive and negative loadings were ordered according to subject cognitive z-score or PDDRS and split into two groups by the median. A higher mean in one group indicated increased perfusion in that region relative to the median, and was thus associated with higher or lower cognitive z-score or PDDRS. The direction of the perfusion changes within the positive and negative voxel loadings were determined and classified as representing increased, decreased or preserved perfusion relating to the examined covariate.

5.4.1 Bootstrapping of cognition and PDDRS related perfusion networks

In order for the perfusion networks created in the previous step to be more easily applicable as a possible prediction measure, it was necessary to create a z-score image that was more representative of the population. The z-score was created by dividing the network image by the standard deviation of the population, which was obtained using a bootstrap estimation procedure.

The bootstrap procedure obtained an approximate population standard deviation by re-sampling the data with replacement over 5000 iterations of PCA. Linear regression at each iteration determined those PC's that correlated significantly ($p< 0.05$) with the dependent variable, in this case cognitive z-score or PDDRS. The PC's were used in linear combination as before to form a cognition or PDDRS-related perfusion network specific to the resampled group at that iteration. The voxel loadings of the 5000 networks were

then used to approximate the mean and standard deviation of the resampled population intensity values per voxel. The population z-score image was created by dividing the original principal component network by the bootstrap population standard deviation.

5.4.2 Validation of cognition and PDDRS related perfusion networks

The ability of the created perfusion network to predict cognition in subjects outside of this group was assessed using leave-one-out (LOO) cross validation. This involves removing 1 subject, and creating a cognition or PDDRS related network from the remaining 49. The expression of this network in the removed subject was then calculated to give a predicted cognition-related or PDDRS-related network score. This process was repeated for all 50 subjects, and the predicted network scores compared against the actual network scores. The strength of the correlation represents how accurately the network may perform in practice as a predictive model.

Chapter 6

Results and Discussion

6.1 Participants

Table 6.1 gives the demographics of the 50 subjects included in this study. There were considerably more PD-MCI (n=41) subjects than PD-N (n=4) and PDD (n=5), due to time constraints restricting the number of subjects able to be included in the analysis. Education and age were reasonably equal across PD-N, PD-MCI and PDD, displaying no significant difference across the groups. Symptom duration was variable, particularly in PD-MCI (range, 1-23 years), but not significantly different across the subject groups. MoCA scores within each group decreased with worsening cognition, with significant ANOVA across all groups at $p<0.001$. Cognitive z-score and PDDRS also displayed significant ANOVA across all groups, at $p<0.00001$ and $p<0.01$ respectively.

TABLE 6.1: Demographics and clinical assessments of the study participants.

	PD-N	PD-MCI	PDD
n	4	41	5
Female:male	1:3	9:32	0:5
Age, years	75.5 (5.0); 71-84	72.3 (5.7); 59-86	77.6 (5.2); 68-84
Education, years	14.0 (1.6); 12-16	12.4 (2.7); 9-19	12.4 (1.5); 11-15
MoCA**	26.3 (0.8); 25-27	22.0 (3.2); 15-28	16.8 (3.0); 12-20
PD symptom duration, years	13 (4.0); 10-20	8 (5.2); 1-23	8 (4.7); 3-15
UPDRS-III	49.5 (16.0); 25-68	38.7 (12.3); 16-65	52.4 (10.9); 38-65
Hoehn and Yahr	median 2.5; 2-4	2.5; 1.5-4	3; 2.5-3
Cognitive z-score***	0.17 (0.51); -0.37 to 0.62	-0.98 (0.62); -2.44 to -0.12	-1.83 (0.44); -2.3 to -1.1
PDDRS*	0.25 (0.14); 0.10-0.49	0.64 (0.33); 0.048-0.99	0.99 (0.01); 0.96-0.99

Values are Mean (Standard Deviation) : Range.
Significant ANOVA across all groups *p<0.01, **p<0.001, ***p<0.00001.

6.2 Linear regression analysis - Cognition

6.2.1 FSL

Linear regression analysis carried out using FSL's randomise function found extensive significant positive correlation ($p < 0.005$, FWE corrected using TFCE) within the ASL_{non} perfusion data with cognitive z-score, accounting for age and sex in the model (figure 6.1). There was found to be no significant correlation of FBB_{cer} voxel values with cognition using the same model.

The results found from analysis of the ASL_{non} data follow the same pattern seen in other works studying the correlation of perfusion and metabolism with cognition, namely significant positive correlation located in the precuneus, frontal, prefrontal and bilateral parieto-occipital cortical regions (T. Melzer et al., 2011)(Huang, Mattis, et al., 2007). Cognitive

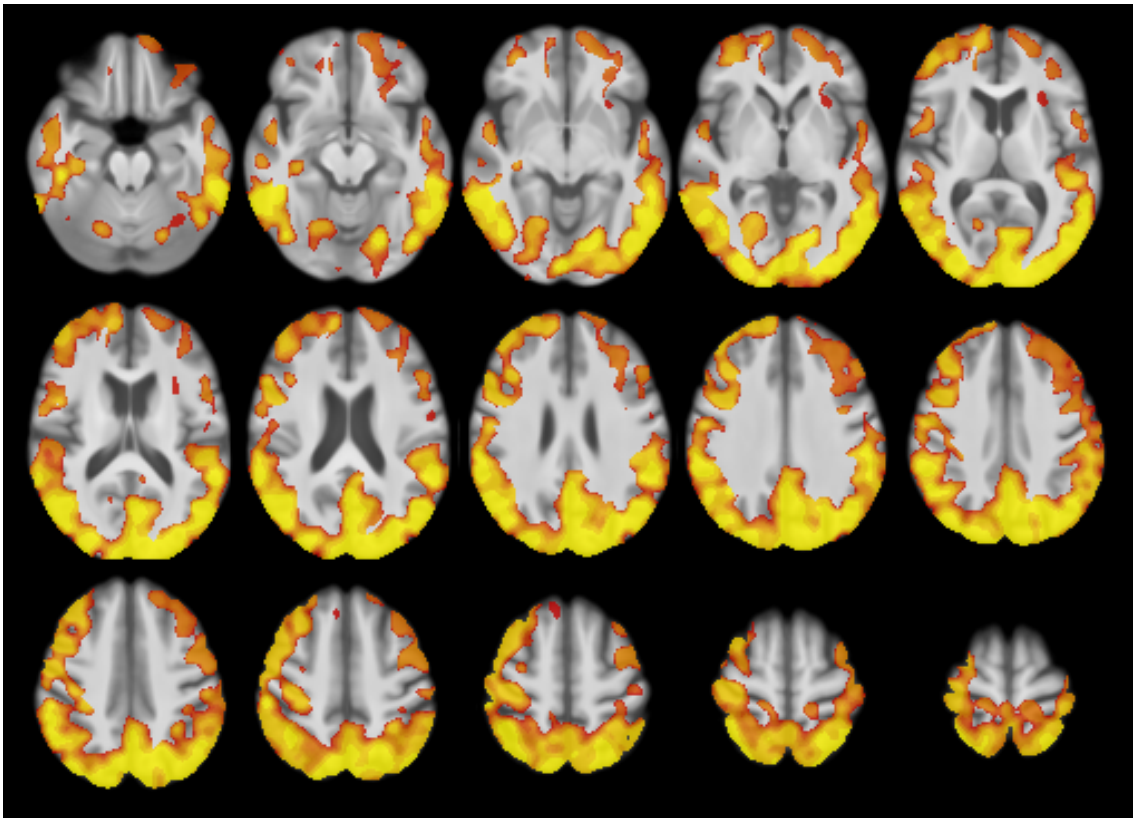

FIGURE 6.1: Axial view of the correlation map output by FSL's Randomise, looking at ASL_{non} positive correlation with cognition, removing age and sex. Areas containing voxels that were significant ($p < 0.005$, FWE corrected using TFCE) in the positive correlation with cognitive z-score are shaded from red to yellow according to the strength of the correlation. Decreases in perfusion with cognition were found in the precuneus, lateral occipital lobes, superior parietal lobes and the prefrontal cortex.

dysfunction has been shown to be particularly associated with metabolic and perfusion deficits in posterior cortical regions (Firbank et al., 2003)(Nobili et al., 2009)(Liepelt et al., 2009). At this stage, the significant correlation of ASL_{non} with cognition in these regions, supported in the literature, helps to verify the pre-processing chain and methodology employed with this subject group.

The FBB_{cer} and ASL_{non} images theoretically represent a similar physiological aspect of brain function; thus it was surprising to find no significant correlation of voxel values with cognition in the FBB_{cer} data, given the strong positive result seen with ASL_{non}. It may be reasonable to attribute a small disparity in the results to the fact that the ASL_{non} data was not normalised to a reference region, while the FBB_{cer} data was normalised to the cerebellum. Whole brain grey matter, white matter and cerebellum as reference regions for intensity normalisation of perfusion images have been shown to produce different results in the comparison of MCI, AD and healthy controls (Lacalle-Aurioles et al., 2013), such that significant differences between the groups were only found when normalising to the whole brain grey matter as a reference region. In separate linear regression analysis, the choice of reference region is not as important, as inherent properties of the data should still be apparent in the analysis.

It may be that this application of early-phase FBB PET imaging does not represent a measure of perfusion as was originally thought, but rather yields a measure of blood pool in the brain as a result of radiotracer activity reaching a constant level before the end of the scanning period. FBB activity reaches a maximum concentration of $\sim 6\%$ injected dose/L within the brain at 10 minutes post-injection (Sabri et al., 2015). The time taken for injection and patient set-up is around 2-3 minutes, thus maximum uptake is reached before the end of the 10 minute scan period. It may be incorrect to include the final 2-3 minutes of continuous scan data in the summed 10-minute image, as the constant concentration may cloud perfusion information. Creating a summed image from the first 6-7 minutes post injection may give a more physiologically relevant image in terms of perfusion, removing the potential blood pool effect. This may be a worthwhile area of future study concerning early-phase PET imaging.

Typical ASL_{GM} and FBB_{GM} images for the same subject are presented in figure 6.2, for the purpose of direct visual comparison. The ASL_{GM} images (A) exhibit a large amount of variation, and often show a marked signal deficit in the posterior parietal region, an

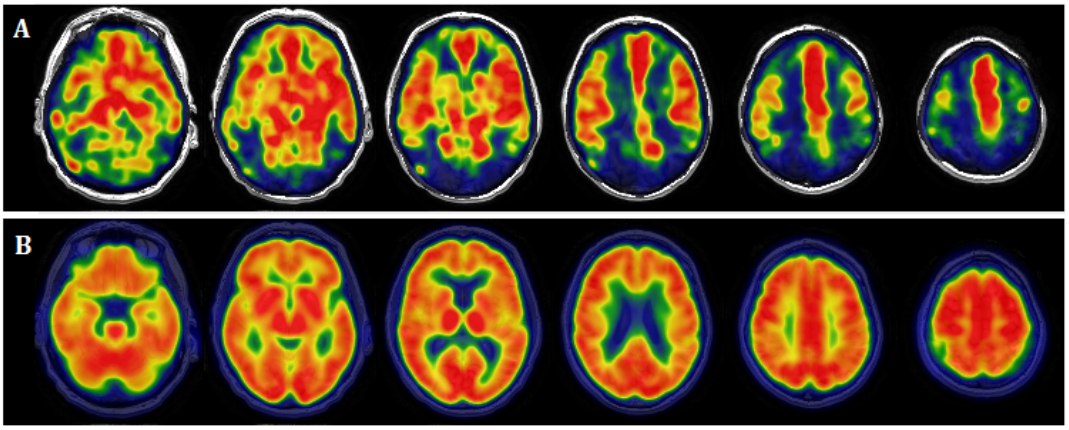

FIGURE 6.2: Sample axial brain slices of A) quantified and cut ASL cerebral blood flow normalised to global grey matter, with high values removed, and B) standard uptake value ratio from early-phase FBB PET, normalised to global grey matter. 'Hot' areas of high signal (red) theoretically relate to increased perfusion in these areas.

area known to display hypoperfusion in PD-MCI and PDD (Nobili et al., 2009)(Firbank et al., 2003). This may indicate that the problem does indeed lie with the interpretation of early-phase PET FBB as a measure of perfusion, rather than the result of pre-processing misjudgement or error. Visually, the FBB_{GM} images (B) display strong signal across the entirety of the brain, which may support the 'blood pool' hypothesis. Direct voxelwise comparison of the ASL_{GM} and FBB_{GM} data, normalised to the whole brain grey matter for the same relative measure (Lacalle-Aurioles et al., 2013), was used in a later section to verify the lack of agreement seen here (see section 6.4).

6.2.2 SPM

Multiple linear regression correlation analysis using SPM supported the results obtained using FSL: the cluster-wise FDR_c corrected cognitive z-score correlation with the ASL_{non} data was significant in the precuneus, posterior parietal and prefrontal regions (FDR_c = 2608 voxels, $p < 0.05$), while analysis of the FBB_{cer} data yielded no significant correlation. A summary of the SPM correlation analysis with the ASL_{non} data is included in figure 6.3, where the correlation map has been FDR^c corrected. Figure 6.4 gives a summary of the FBB_{cer} correlation statistics, showing no significant voxels or voxel clusters that survive FDR^c correction.

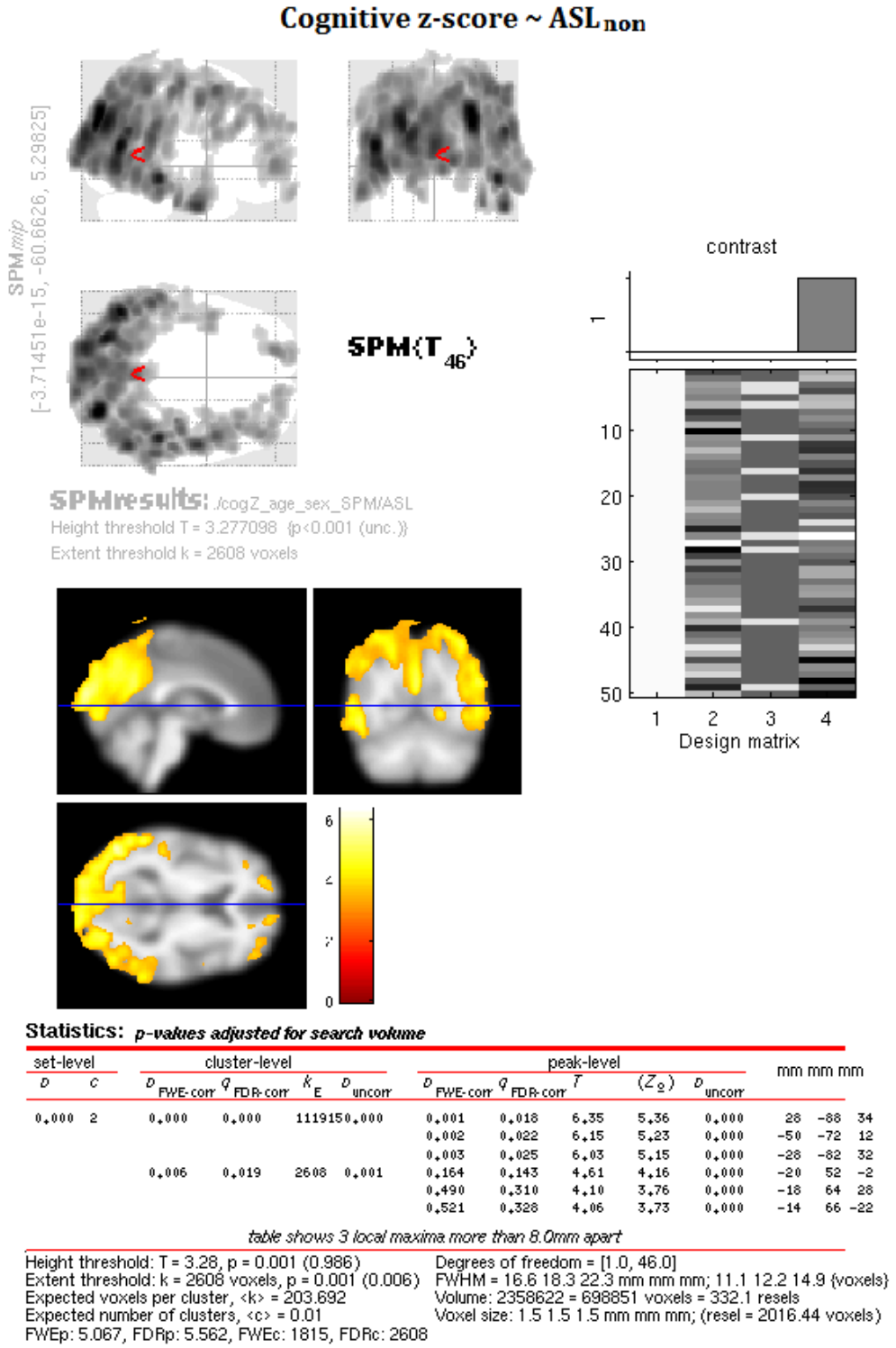

Statistics: *p-values adjusted for search volume*

set-level		cluster-level				peak-level					mm mm mm		
p	c	$p_{FWE\text{-}corr}$	$q_{FDR\text{-}corr}$	k_E	p_{uncorr}	$p_{FWE\text{-}corr}$	$q_{FDR\text{-}corr}$	T	(Z_e)	p_{uncorr}			
0.000	2	0.000	0.000	1119	150.000	0.001	0.018	6.35	5.36	0.000	28	-88	34
						0.002	0.022	6.15	5.23	0.000	-50	-72	12
						0.003	0.025	6.03	5.15	0.000	-28	-82	32
		0.006	0.019	2608	0.001	0.164	0.143	4.61	4.16	0.000	-20	52	-2
						0.490	0.310	4.10	3.76	0.000	-18	64	28
						0.521	0.328	4.06	3.73	0.000	-14	66	-22

table shows 3 local maxima more than 8.0mm apart

Height threshold: T = 3.28, p = 0.001 (0.986)
Extent threshold: k = 2608 voxels, p = 0.001 (0.006)
Expected voxels per cluster, <k> = 203.692
Expected number of clusters, <c> = 0.01
FWEp: 5.067, FDRp: 5.562, FWEc: 1815, FDRc: 2608

Degrees of freedom = [1.0, 46.0]
FWHM = 16.6 18.3 22.3 mm mm mm; 11.1 12.2 14.9 {voxels}
Volume: 2358622 = 698851 voxels = 332.1 resels
Voxel size: 1.5 1.5 1.5 mm mm mm; (resel = 2016.44 voxels)

FIGURE 6.3: There was a widespread significant positive correlation of voxel values with cognitive z-score within the ASL_{non} perfusion data ($p < 0.05$, FDR^c corrected), found using SPM. The extent threshold is here defined by the significant cluster extent determined by FDR_c correction (k=2608 voxels). Areas of significant positive correlation are shaded red to yellow according to the strength of the correlation. This correlation follows a very similar pattern as that seen using FSL to carry out the regression (figure 6.1).

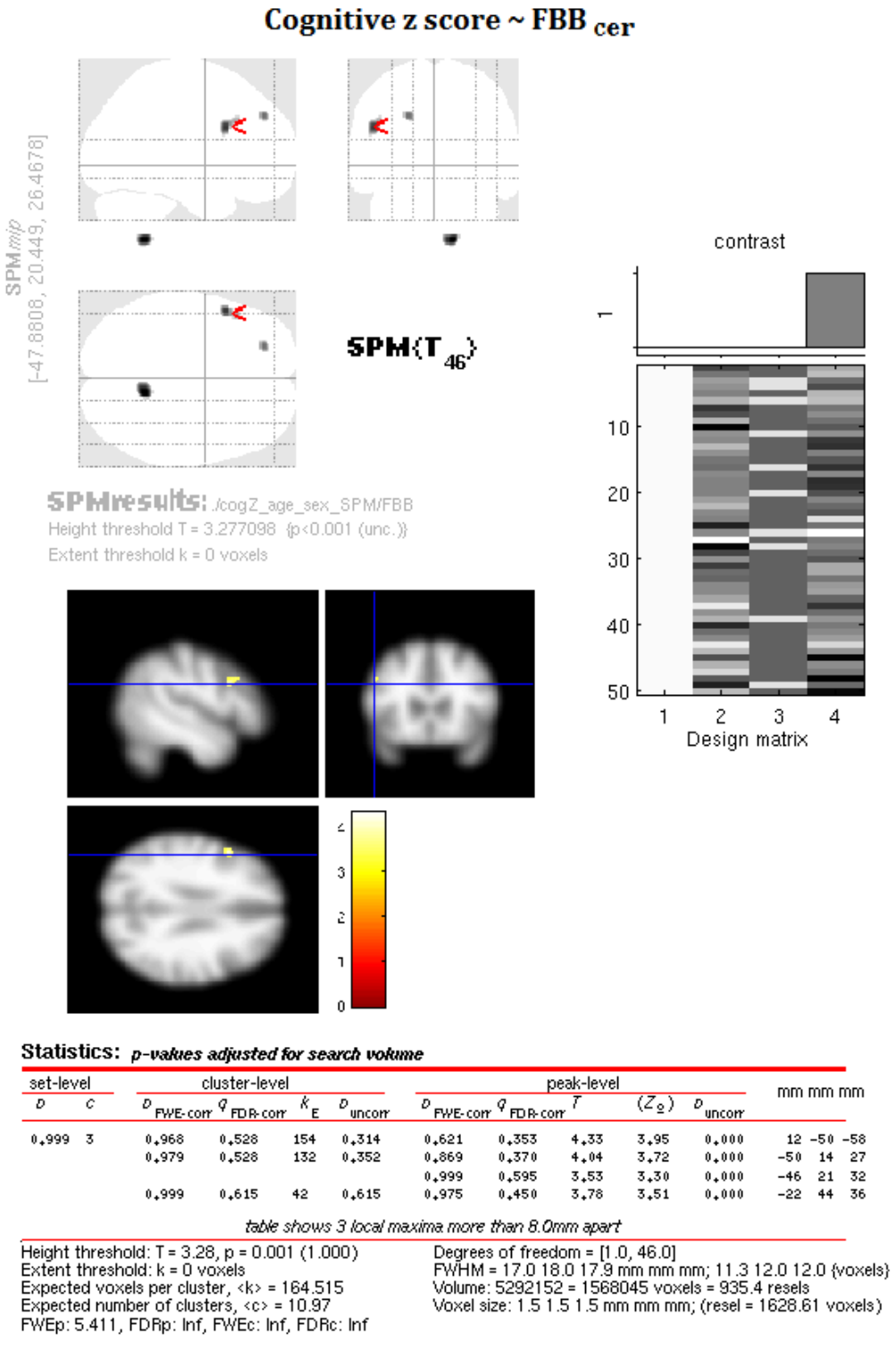

FIGURE 6.4: There was found to be no surviving positive correlation between FBB_{cer} voxel values and cognitive z-score using SPM (FDR_c corrected for multiple comparisons). The required voxel extent for significance was $FDR_c = inf$, relating to no surviving voxel clusters ($p < 0.05$ uncorrected). This result supports the finding obtained from the same analysis using FSL.

6.2.3 Domain results

The specific neuropsychological domain scores, used to compute overall cognitive Z-score, were then input into separate linear regression analyses with the FBB_{cer} and ASL_{non} image data. This may provide further insight as to the particular cognitive domains associated with changes in perfusion, and the regional extent of this correlation. SPM was employed for this purpose, as it is less computationally expensive than FSL.

As expected, FBB_{cer} displayed no correlation with any of the domain scores, surviving FDR^c correction. This was not surprising due to the lack of correlation with overall cognitive z-score seen previously.

The ASL_{non} data was found to correlate significantly ($p< 0.05$, FDR_c-corrected) with three of the five domains, namely executive function, attention and working memory, and visuo-spatial performance. Figures 6.5, 6.6 and 6.7 present a summary of the results for each regression. Executive function and attention were found to correlate with voxels values primarily in the precuneus and posterior parieto-occipital regions, while visuo-spatial performance was involved with voxels in the lateral parietal and temporal lobes. These areas are involved in somatosensory and visual association, and the integration of various sensory interpretations for the formation of thought based on sensory input (Tortora & Derrickson, 2012). The precuneus is known to be associated with a number of higher-order cognitive functions, such as episodic memory, self-processing and perception, and the processing of visuo-spatial information (Cavanna & Trimble, 2006).

6.3 Linear regression analysis - PDDRS

Linear regression analysis was again carried out on both FBB_{cer} and ASL_{non} data, this time with subject PDDRS score as the explanatory variable, accounting for age and sex. The design matrix for this regression, carried out using Randomise, is given in figure A.6.

There was found to be no significant correlation of FBB_{cer} voxel values with PDDRS in this subject group. This null result was not surprising as PDDRS is closely related to cognitive z-score, and so further supports the finding of no significant correlation between FBB_{cer} data and cognition.

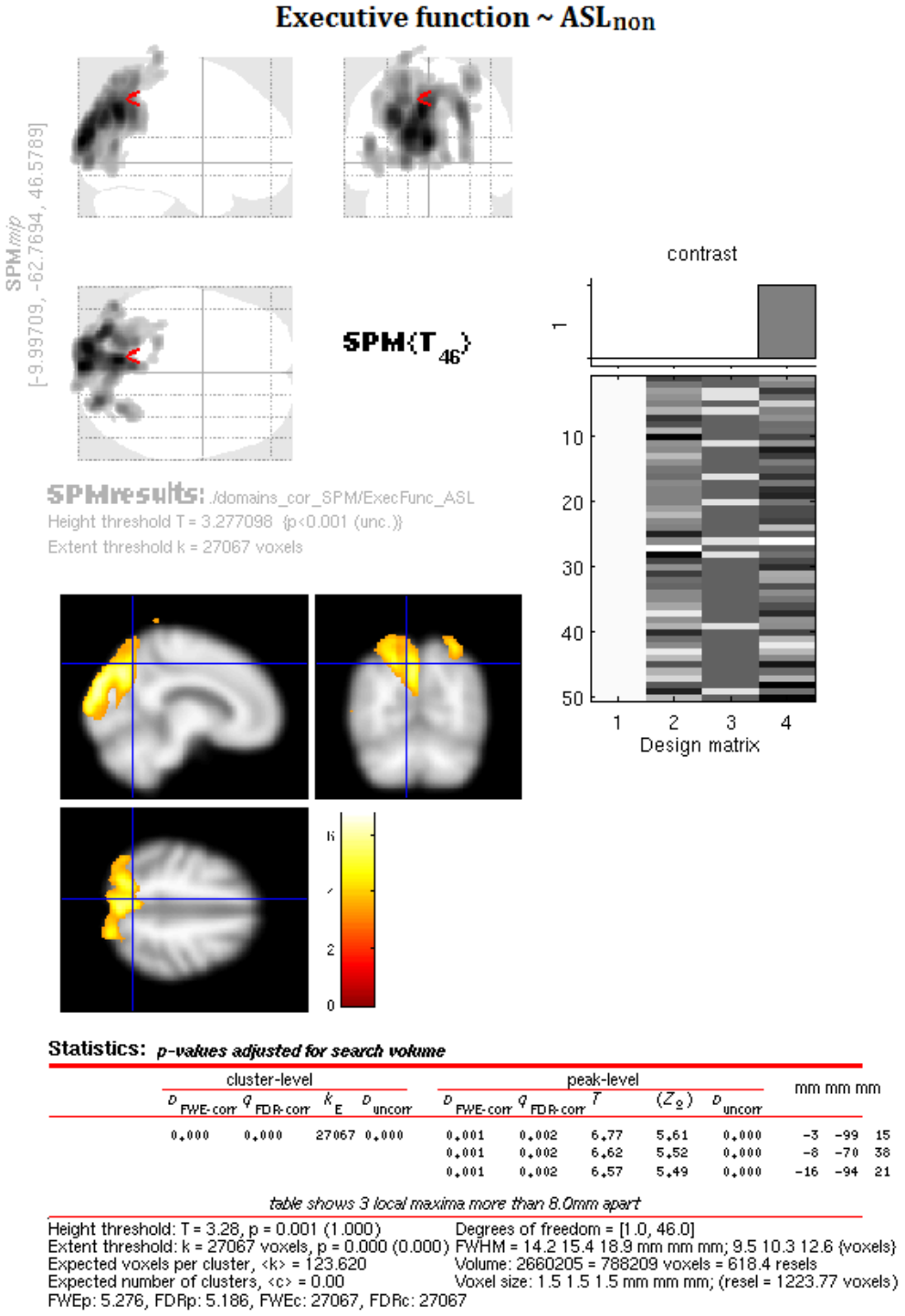

Statistics: *p-values adjusted for search volume*

cluster-level				peak-level					mm mm mm		
$p_{FWE\text{-}corr}$	$q_{FDR\text{-}corr}$	k_E	p_{uncorr}	$p_{FWE\text{-}corr}$	$q_{FDR\text{-}corr}$	T	(Z_e)	p_{uncorr}			
0.000	0.000	27067	0.000	0.001	0.002	6.77	5.61	0.000	-3	-99	15
				0.001	0.002	6.62	5.52	0.000	-8	-70	38
				0.001	0.002	6.57	5.49	0.000	-16	-94	21

table shows 3 local maxima more than 8.0mm apart

Height threshold: T = 3.28, p = 0.001 (1.000)
Extent threshold: k = 27067 voxels, p = 0.000 (0.000)
Expected voxels per cluster, <k> = 123.620
Expected number of clusters, <c> = 0.00
FWEp: 5.276, FDRp: 5.186, FWEc: 27067, FDRc: 27067
Degrees of freedom = [1.0, 46.0]
FWHM = 14.2 15.4 18.9 mm mm mm; 9.5 10.3 12.6 {voxels}
Volume: 2660205 = 788209 voxels = 618.4 resels
Voxel size: 1.5 1.5 1.5 mm mm mm; (resel = 1223.77 voxels)

FIGURE 6.5: There was a significant positive correlation of voxel values with executive function domain score within the ASL_{non} perfusion data ($p< 0.05$, FDR^c corrected), primarily in the precuneus and parieto-occipital cortex. The extent threshold applied here was defined by the significant cluster extent determined by FDR_c correction (k=23119 voxels). Areas of significant positive correlation are shaded red to yellow according to the strength of the correlation.

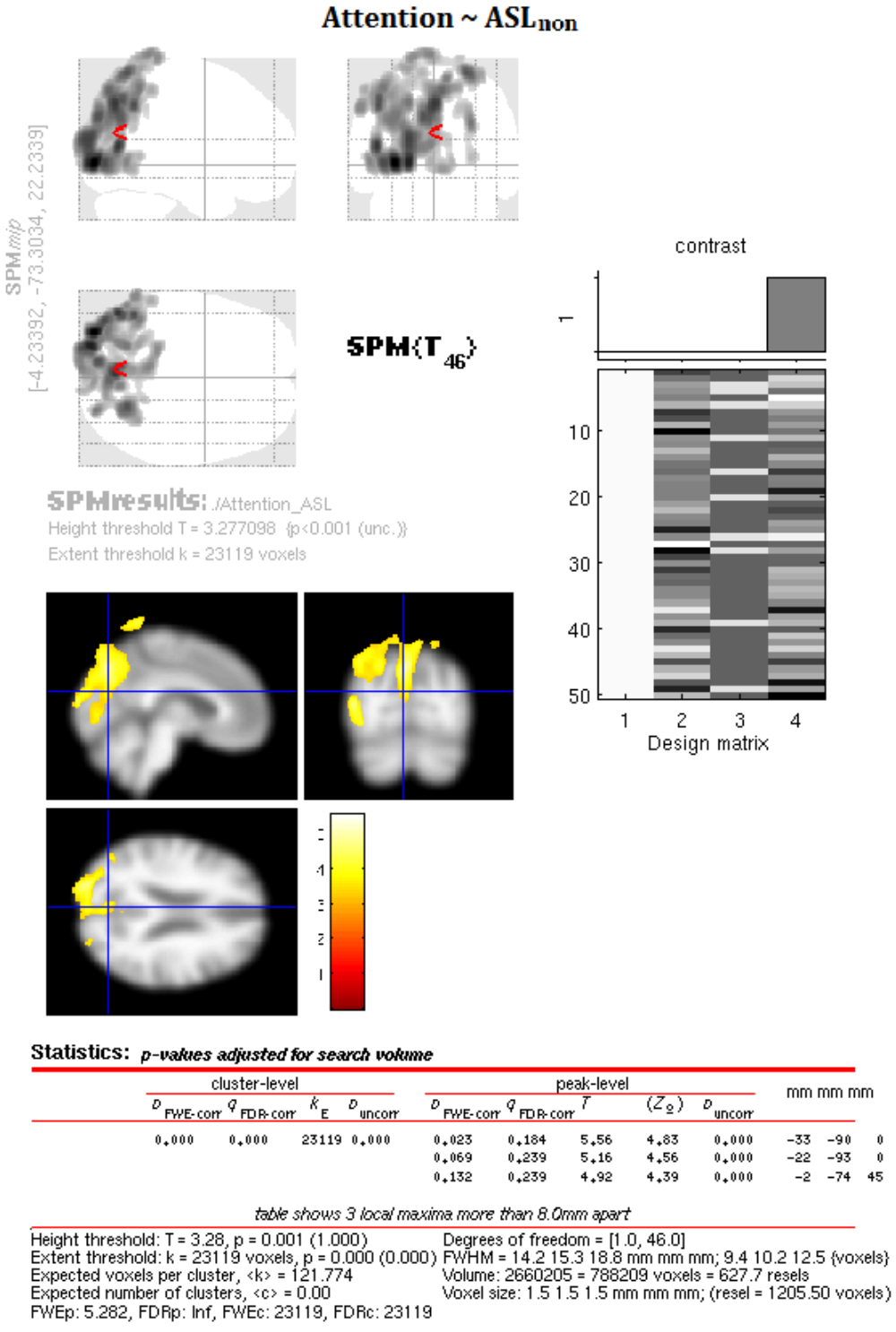

FIGURE 6.6: There was a significant positive correlation of voxel values with attention domain score within the ASL_{non} perfusion data ($p < 0.05$, FDR^c corrected), primarily in the precuneus and left parieto-occipital cortex. The extent threshold applied here was defined by the significant cluster extent determined by FDR_c correction (k=27067 voxels). Areas of significant positive correlation are shaded red to yellow according to the strength of the correlation.

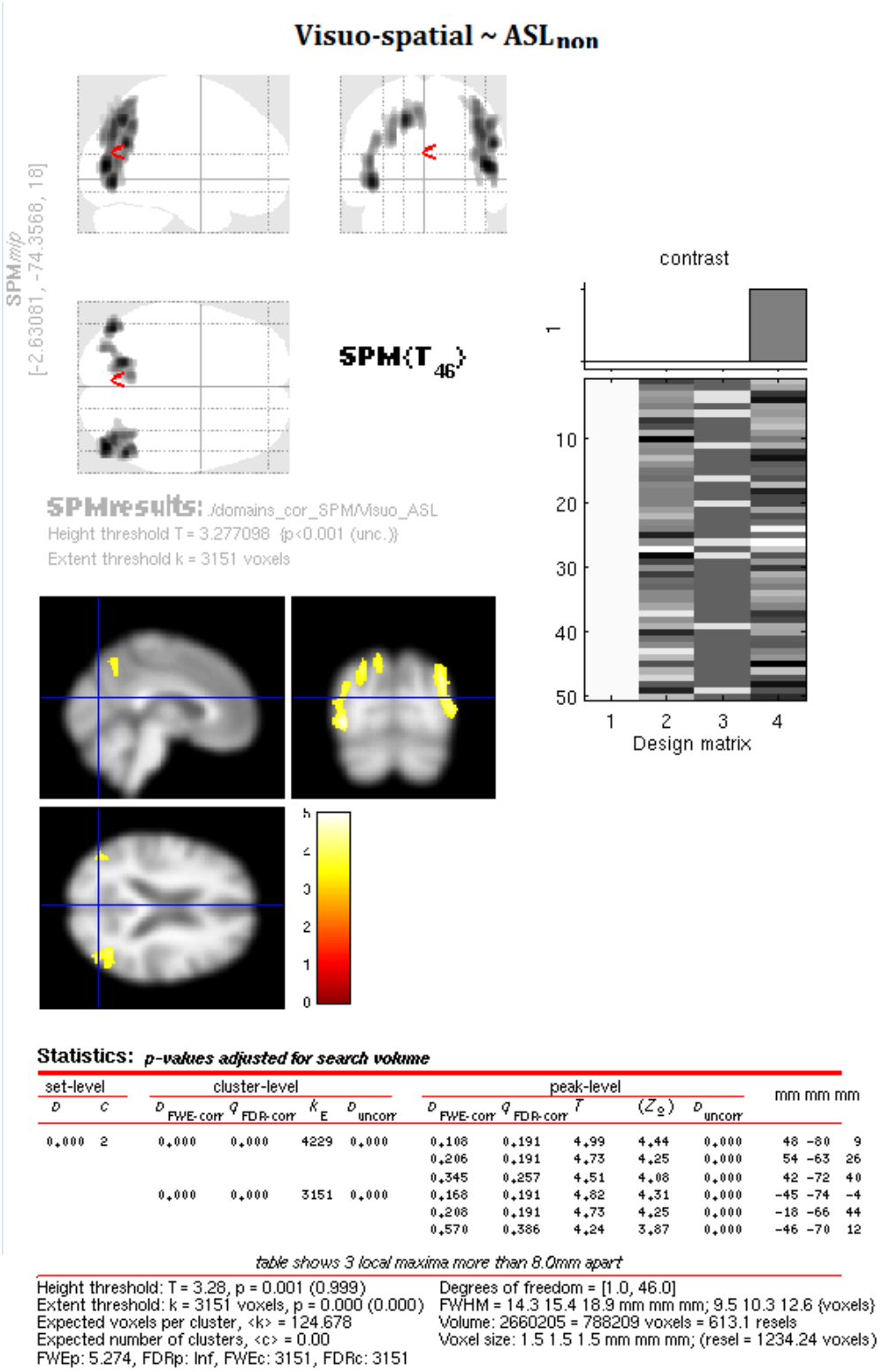

Statistics: *p-values adjusted for search volume*

set-level		cluster-level				peak-level					mm mm mm		
p	c	$p_{FWE\text{-}corr}$	$q_{FDR\text{-}corr}$	k_E	p_{uncorr}	$p_{FWE\text{-}corr}$	$q_{FDR\text{-}corr}$	T	(Z_e)	p_{uncorr}			
0.000	2	0.000	0.000	4229	0.000	0.108	0.191	4.99	4.44	0.000	48	-80	9
						0.206	0.191	4.73	4.25	0.000	54	-63	26
						0.345	0.257	4.51	4.08	0.000	42	-72	40
		0.000	0.000	3151	0.000	0.168	0.191	4.82	4.31	0.000	-45	-74	-4
						0.208	0.191	4.73	4.25	0.000	-18	-66	44
						0.570	0.386	4.24	3.87	0.000	-46	-70	12

table shows 3 local maxima more than 8.0mm apart

Height threshold: T = 3.28, p = 0.001 (0.999)
Extent threshold: k = 3151 voxels, p = 0.000 (0.000)
Expected voxels per cluster, <k> = 124.678
Expected number of clusters, <c> = 0.00
FWEp: 5.274, FDRp: Inf, FWEc: 3151, FDRc: 3151

Degrees of freedom = [1.0, 46.0]
FWHM = 14.3 15.4 18.9 mm mm mm; 9.5 10.3 12.6 {voxels}
Volume: 2660205 = 788209 voxels = 613.1 resels
Voxel size: 1.5 1.5 1.5 mm mm mm; (resel = 1234.24 voxels)

FIGURE 6.7: There was a significant positive correlation of voxel values with visuo-spatial domain score within the ASL_{non} perfusion data ($p < 0.05$, FDR^c corrected), primarily in the bilateral temporo-parietal cortical areas. The extent threshold applied here was defined by the significant cluster extent determined by FDR_c correction (k=3151 voxels). Areas of significant positive correlation are shaded red to yellow according to the strength of the correlation.

ASL_{non} was found to display a significant negative correlation with PDDRS ($p < 0.001$, FWE-corrected), following a very similar pattern as that seen previously with cognitive z-score. Significant results on the negative contrast indicated negative correlation of voxel intensity with PDDRS sufficient to reject the null hypothesis, i.e. a decrease in perfusion within a significant region corresponded to an increased dementia risk score, or vice versa. This would seem to indicate that decreased perfusion in these regions (shaded blue/green in figure 6.8) is a significant indicator of imminent conversion to dementia, as given by the PDDRS. Linear regression analysis using SPM also exhibited extensive negative correlation in these regions (figure 6.9, $FDR^c = 111685$ voxels, $p < 0.05$), which supports the finding obtained using FSL. The spatial extent and direction of the perfusion changes in the ASL_{non} data relating to increased PDDRS were determined using network analysis (see section 6.5.2).

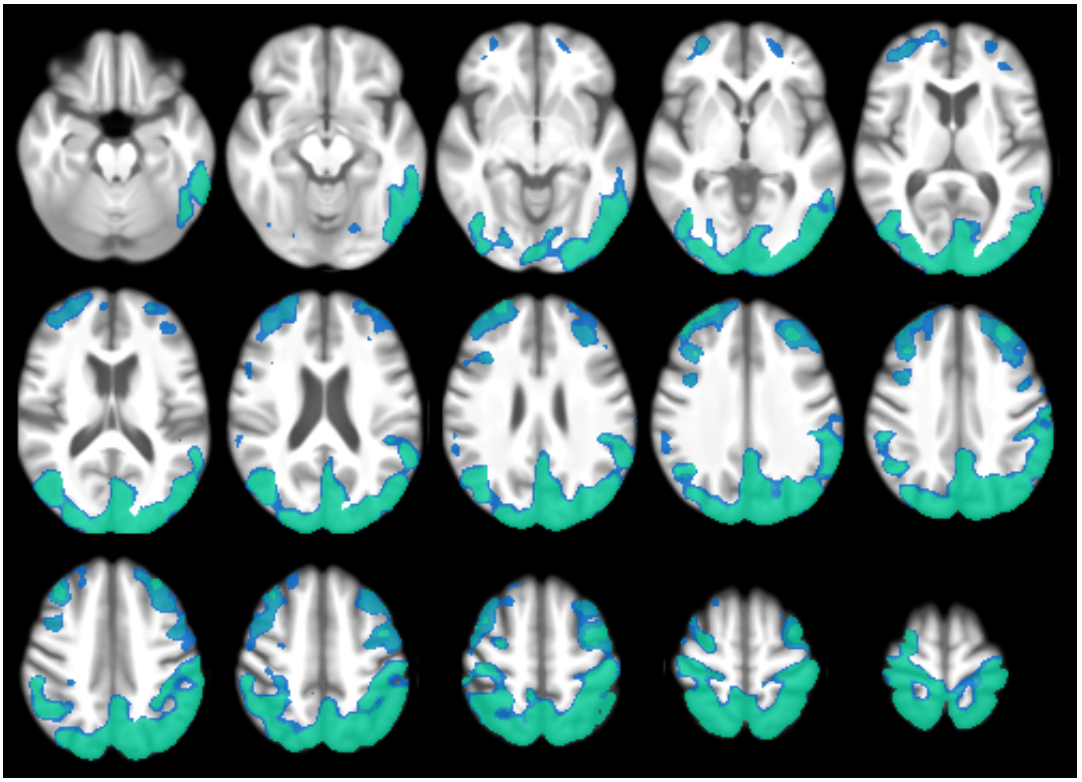

FIGURE 6.8: There was a widespread significant negative correlation of voxel value with PDDRS within the ASL_{non} perfusion data ($p < 0.001$, FWE corrected). Areas of significant negative correlation are shaded blue to green according to the strength of the correlation. This correlation follows a very similar pattern as that seen with cognition, a reflection of the close relationship of the PDDRS with cognitive z-score.

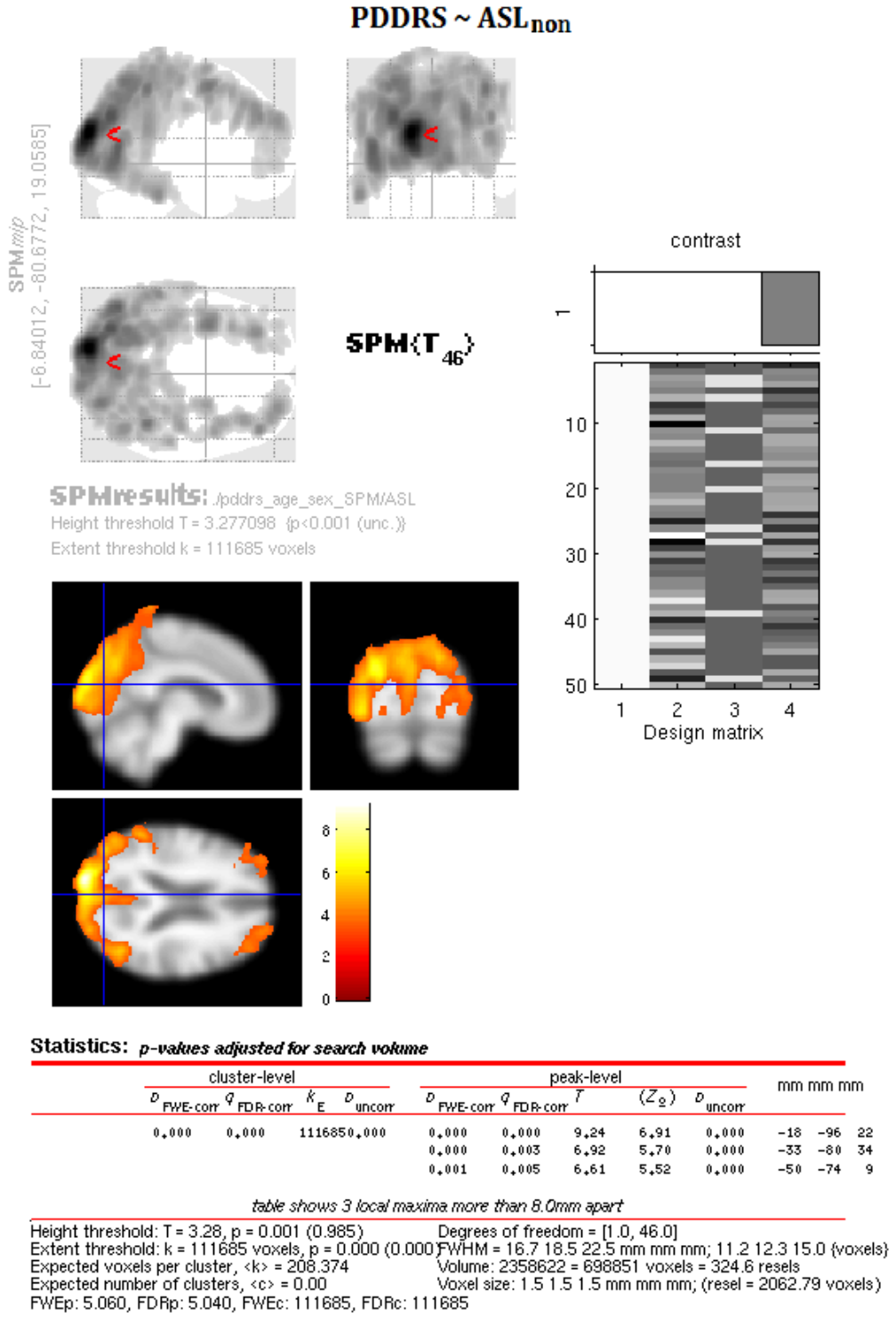

Statistics: *p-values adjusted for search volume*

cluster-level				peak-level					mm mm mm		
$p_{FWE-corr}$	$q_{FDR-corr}$	k_E	p_{uncorr}	$p_{FWE-corr}$	$q_{FDR-corr}$	T	(Z_e)	p_{uncorr}			
0.000	0.000	1116850	0.000	0.000	0.000	9.24	6.91	0.000	-18	-96	22
				0.000	0.003	6.92	5.70	0.000	-33	-80	34
				0.001	0.005	6.61	5.52	0.000	-50	-74	9

table shows 3 local maxima more than 8.0mm apart

Height threshold: T = 3.28, p = 0.001 (0.985) Degrees of freedom = [1.0, 46.0]
Extent threshold: k = 111685 voxels, p = 0.000 (0.000) FWHM = 16.7 18.5 22.5 mm mm mm; 11.2 12.3 15.0 (voxels)
Expected voxels per cluster, <k> = 208.374 Volume: 2358622 = 698851 voxels = 324.6 resels
Expected number of clusters, <c> = 0.00 Voxel size: 1.5 1.5 1.5 mm mm mm; (resel = 2062.79 voxels)
FWEp: 5.060, FDRp: 5.040, FWEc: 111685, FDRc: 111685

FIGURE 6.9: There was a widespread significant negative correlation of voxel values with PDDRS within the ASL_{non} perfusion data ($p < 0.05$, FDR^c corrected). The extent threshold is here defined by the significant cluster extent determined by FDR_c correction. Areas of significant negative correlation are shaded red to yellow according to the strength of the correlation. This correlation follows a very similar pattern as that seen using FSL to carry out the regression (figure 6.8).

6.4 Voxelwise Correlation Analysis

Voxelwise correlation analysis between the ASL_{GM} and FBB_{GM} image data was performed, first using FSL's Randomise function and then using the rBPM toolbox. The results of this analysis determined if there exists any correlation between the PET and ASL-derived images for this subject group, such that they can be said to demonstrate the same relative measure of brain perfusion.

6.4.1 FSL

FSL was initially used to carry out voxelwise correlation analysis of FBB_{GM} with ASL_{GM} perfusion image data. The design matrix employed here is given in Appendix A (figure A.7). The permutation produced a map of the voxelwise correlation coefficients, which was thresholded according to an alpha level $\alpha = 0.05$, corresponding to significant correlation ($p < 0.05$). No voxels survived this threshold, indicating no significant correlation between the FBB_{GM} and ASL_{GM} perfusion data.

The extensive lack of significant correlation seems to support the hypothesis that FBB_{GM} and ASL_{GM} do not in fact show the same relative measure of grey matter perfusion. It would be reasonable to expect significant correlation across almost all brain regions, if early-phase amyloid PET and ASL MRI were in fact both measures of perfusion. As the option to add voxelwise EVs to the GLM in FSL was still in development at the time of this analysis, it was deemed prudent to check that these results were correct. This was achieved by running voxelwise correlation of the FBB_{GM} and ASL_{GM} image sets with themselves. Randomise uses resampling without replacement in the permutation, so this is a viable approach to verify the permutation inference method used by FSL. From this analysis, we would expect complete correlation across the whole brain; however, that was not found. Figure 6.10 displays axial mean brain slices overlaid with the correlation between ASL_{GM} and itself, where red areas represent significant positive correlation and blue areas represent significant negative correlation ($p < 0.05$).

The presence of negative correlation in the image indicates that there was some error in the current work's implementation of FSL's algorithm, used to test voxelwise image correlation. Furthermore, the correlation of FBB_{GM} with itself did not present as significant. This may be due to an error in the permutation, as the option to add voxelwise EVs as

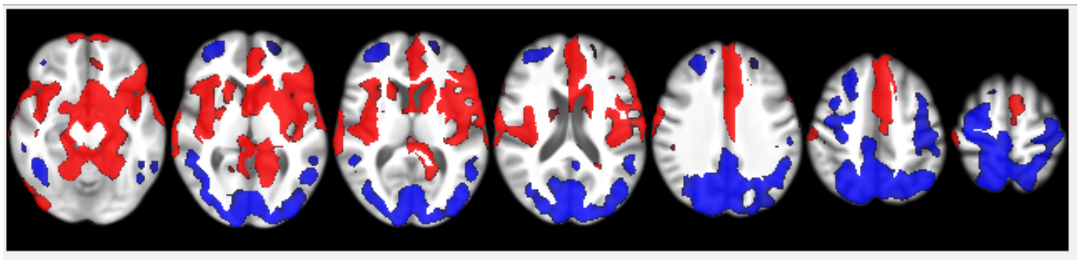

FIGURE 6.10: This figure shows the voxelwise correlation map output by FSL's Randomise, where ASL_{GM} was compared against itself in order to verify results of the permutation. Red areas represent areas of significant positive correlation ($p< 0.05$); blue areas represent areas of significant negative correlation. The results of this correlation indicate error in the permutation employed by FSL to conduct voxelwise analysis, which is still under development.

confounds in the FSL GLM is still in development. This issue may be addressed in future work by examining the code used to conduct voxelwise correlation analysis within the Randomise function. For the purpose of this thesis, voxelwise analysis using rBPM was employed as an alternative to FSL, on the basis that rBPM was developed specifically for voxelwise multi-modality analysis and should yield representative results.

6.4.2 Results using rBPM

Verification of the rBPM voxelwise analysis was first carried out in the same manner as with FSL. The resulting correlation image displayed significant voxels ($p< 0.05$, FWE corrected) across the whole brain, with a correlation coefficient of r=1 as expected (see figure 6.11). Interpretation of the results given by rBPM may thus be carried out with confidence that the procedure is correct.

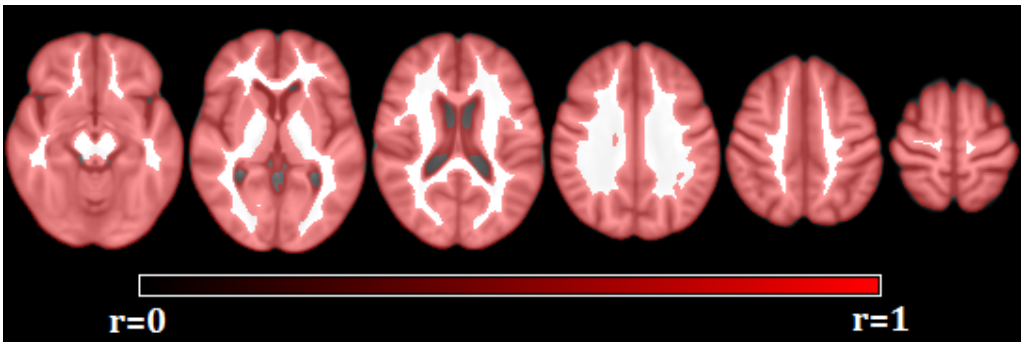

FIGURE 6.11: The voxelwise correlation map output by FSL's Randomise, where ASL_{GM} was compared against itself in order to verify results of the permutation. There is significant correlation ($p< 0.05$ FWE corrected, r=1) across the entire brain, within the confines of the grey matter mask applied in the regression.

The design matrix employed by rBPM in the voxelwise analysis of FBB_{GM} with ASL_{GM} is the same as that used previously within FSL (figure A.7). There was very little significant correlation found between the two image sets, with only one small cluster surviving correction for multiple comparisons (figure 6.12 A; $p<0.05$ FWE corrected), corresponding to a moderate correlation of $r=0.6$. The uncorrected correlation image (figure 6.12 B; $p<0.001$ uncorrected) presents a larger number of significant voxels; however, these correspond to a low R-value ($r=0.4$), far below that which may be regarded as a strong correlation ($r>0.7$). Further relaxation of the statistical threshold revealed more voxels involved in the correlation (figure 6.12 C; $r=0.3$, $p<0.01$ uncorrected), but these can not be regarded as being truly significant. It can be concluded that there exists no evidence of any voxel intensity correlation between the FBB_{GM} and ASL_{GM} image data for this subject group.

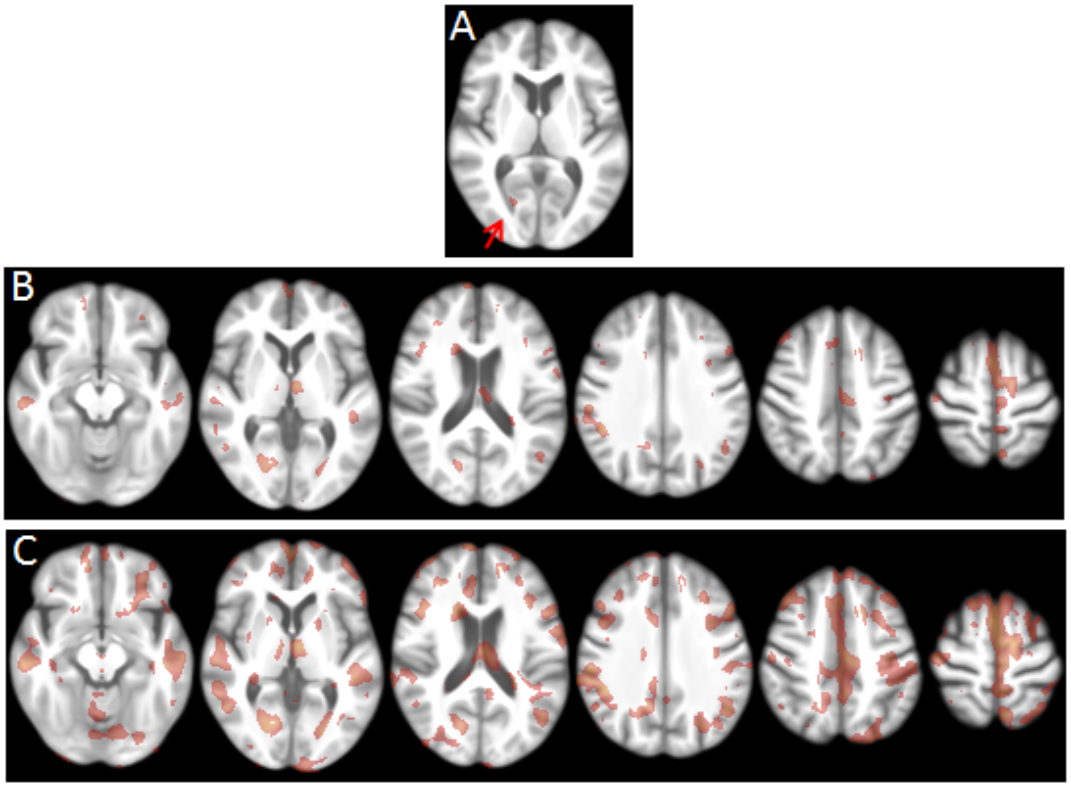

FIGURE 6.12: The results of the voxelwise correlation between FBB_{GM} and ASL_{GM} using robust BPM found very little association; **(A)** A single voxel cluster (red arrow) was deemed significant by the analysis ($r=0.6$, $p<0.05$, FWE corrected), visible in one axial slice; **(B)** A less stringent statistical threshold of $p<0.001$ uncorrected revealed greater voxelwise association, however the correlation was quite weak ($r=0.4$); **(C)** Further relaxation of the statistical threshold revealed more voxels involved in the correlation, but these may not be regarded as significant ($r=0.3$, $p<0.01$ uncorrected).

6.4.3 Comparison of regional mean values

The null result given by the previous voxelwise analysis was supported by comparison of mean regional voxel values, extracted from various cortical and subcortical brain regions using the script 'mean_vals.m'. The regions chosen for comparison were the global grey matter, whole brain, precuneus, thalamus, midfrontal gyrus and putamen.

The regional mean values obtained from the FBB_{GM} and ASL_{GM} data for each subject were entered into a simple correlation analysis, yielding Pearson's correlation coefficients for each region (table 6.2). The midfrontal gyrus (MFG) was the only region that displayed a significant correlation between the regional mean values from each dataset, and even then, the correlation was not strong (p=0.009, r=0.4). The scatter plots representing each of the regional correlations are included in Appendix B (figures B.1, B.2 and B.3). The lack of correlation is apparent from visual assessment of these scatter plots, with the exception of the MFG scatter plot, which do not follow a linear slope but rather take on a 'shotgun' pattern.

These findings support the results of the voxelwise correlation; however, at this stage early-phase FBB PET should not be disregarded as a potential measure of perfusion. Further examination of FBB employing only the first 6-7 minutes may avoid the blood pool phenomenon proposed in this thesis. This may be a valuable avenue of future enquiry with this same subject group under the longitudinal study at the NZBRI.

	Grey matter	Whole brain	Precuneus	Thalamus	Midfrontal gyrus	Putamen
P-value	0.6	0.5	0.2	0.8	0.009*	0.5
R-value	-0.07	0.1	0.2	-0.03	0.4	0.1

TABLE 6.2: P and R-values obtained from comparison of mean regional values, extracted from select cortical and subcortical regions of ASL_{GM} and FBB_{GM} data. There was found to be no significant correlation within the examined regions, except for the midfrontal gyrus*.

6.5 Principal component analysis

Principal component analysis (PCA) was performed on the ASL_{non} perfusion data only, given the distinct lack of correlation within FBB_{cer} data with either cognition or PDDRS. The first 10 principal components were selected for further investigation, on the basis that they explained ~67% of the variance. These 10 z-scored principal components (PCs) were then examined for any correlation with cognitive z-score and PDDRS by linear regression analysis.

6.5.1 Cognition-related network

PCs 1, 3, 4 and 7, explaining 23.8, 10.1, 4.1 and 2.8% of the variance respectively, were found to relate significantly with cognitive z-score ($p<0.05$). Figure 6.13 illustrates these components, thresholded at $|z| >1.96$, corresponding to a two-tailed $p<0.05$.

The PC's were used in linear combination to form a characteristic cognition-related ASL perfusion network, using the correlation coefficients from the regression (1, 3, 4 and 7; β = -2.23, -1.82, 3.1381, 3.71). The direction of the correlation represented by positive ($z > 1.96$) and negative ($z < -1.96$) voxel loadings was determined by comparing the absolute mean values from the ASL_{non} data within these regions. Positive loadings in the cognition-related network were found to relate to decreased perfusion, while negative loadings were found to indicate preserved perfusion.

Network reliability and validation

In order for the ASL_{non} cognitive network to be reliable as a predictor of cognition outside of this subject group, the network was z-scored according to a derived population standard deviation. This was done using the bootstrap estimation procedure described in the method (see section 5.4.1). The resulting cognition-related network, representative of the resampled population, is given in figure 6.14, where red and blue regions denote preserved and decreased perfusion respectively, thresholded according to $|z| > 1.96$. It is important to remember that regions coloured red indicate preservation and not relative increases (as is the usual convention in neuroimaging). Perfusion deficits were located in the left lateral occipital cortex (superior and inferior), posterior parieto-occipital regions, left inferior temporal gyrus, and the right lateral occipital cortex, to a lesser degree. The

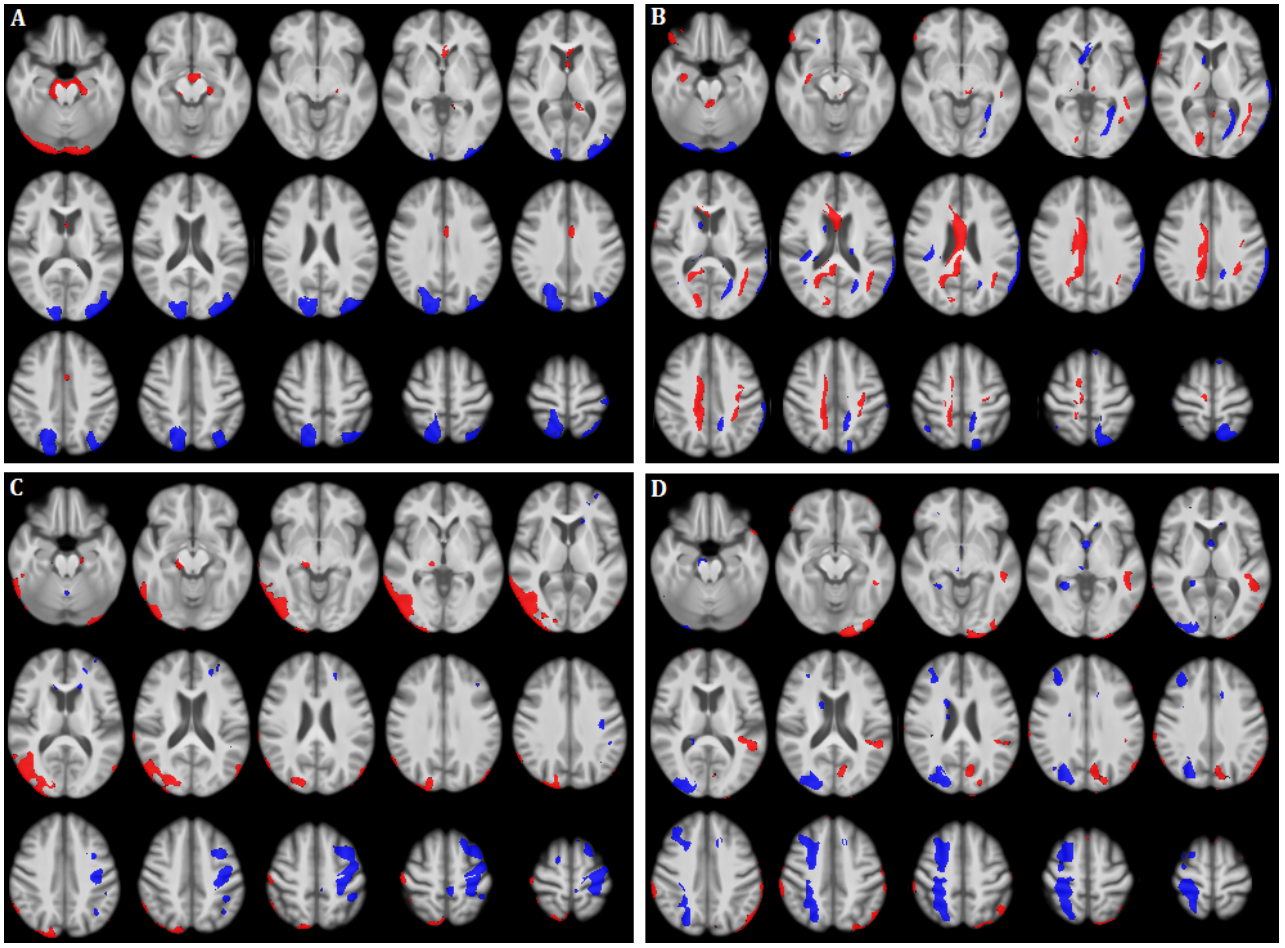

FIGURE 6.13: Principal components found to relate to cognition and PDDRS, overlaid on a mean brain image. **(A)** Principal component 1 was significantly related to cognitive z-score and PDDRS, demonstrating decreased perfusion (blue) in posterior-parietal regions, with preserved perfusion in anterior cingulate (red). **(B)** Principal component 3 was significantly related to cognitive z-score and PDDRS, demonstrating decreased perfusion in the left superior parietal lobule, precuneus and left intracalcarine cortex, with preserved perfusion in the right intracalcarine cortex. **C** Principal component 4 was significantly related to cognitive z-score, demonstrating decreased perfusion in left superior parietal lobule, lateral occipital cortex, and left pre-central, post-central and middle frontal gyri, with preserved perfusion in inferior right lateral occipital cortex, and right middle temporal, angular and post-central gyri. **(D)** Principal component 7 was significantly related to cognitive z-score, demonstrating decreased perfusion in right post-central and middle frontal gyri, and right lateral parieto-occipital regions, with preserved perfusion in precuneus , left lateral occipital cortex and superior temporal gyrus. Components 2, 5, 6, 8, 9 and 10 were not significantly related to the tested covariates.

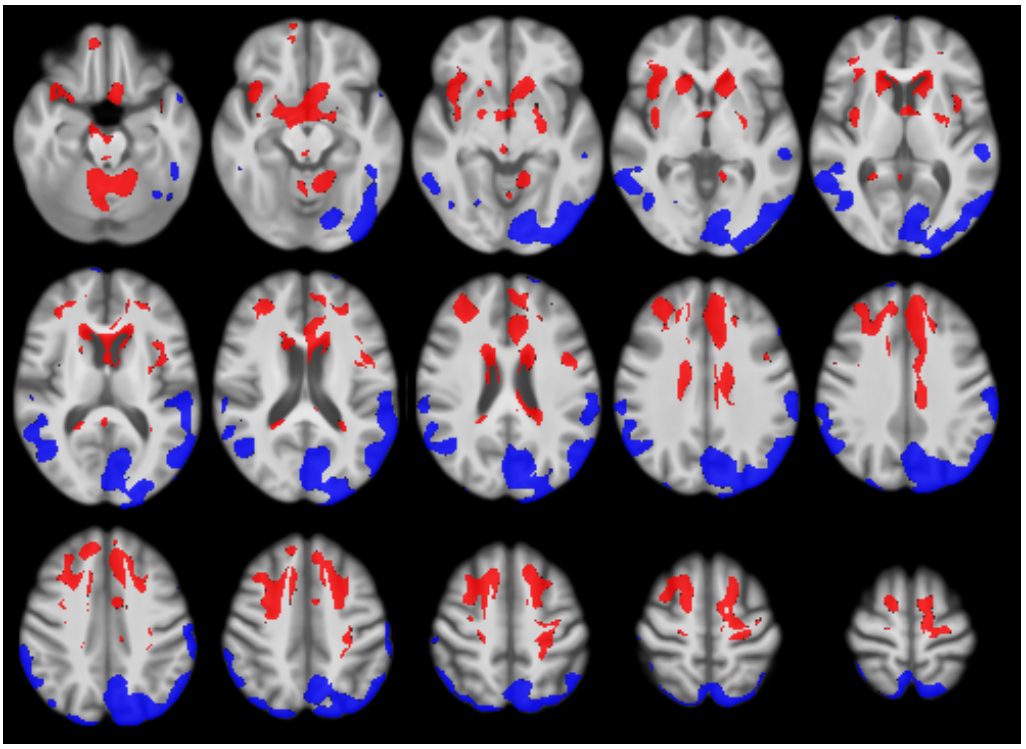

FIGURE 6.14: Cognition-related perfusion network created by the bootstrap estimation procedure. Perfusion deficits were located in the left lateral occipital cortex (superior and inferior), posterior parieto-occipital regions, left inferior temporal gyrus, and the right lateral occipital cortex, to a lesser degree. Preserved perfusion was located in the anterior paracingulate and cingulate gyrus, caudate, thalamus and bilateral superior frontal gyrus.

particular involvement of the posterior parieto-occipital region in the network is supported by previous network analysis conducted by Melzer et al (2011), which identified this region as relating significantly with cognition and age. Preserved perfusion was located in the anterior paracingulate and cingulate gyrus, caudate, thalamus and bilateral superior frontal gyrus.

LOO cross-validation was used to assess the reliability of the cognitive network. The cross-validation found a strong correlation between the predicted and actual network scores (coefficient of correlation r=0.81, $p < 0.000001$). A scatter plot of the estimated cognitive network scores against the actual network scores shows this correlation (figure 6.15). The strong correlation indicates the cognition-related perfusion network formed from this subject group may be a reliable predictor of network score in an independent ASL perfusion dataset. This is an exciting result, as network scores obtained from neuroimaging in this way could conceivably be used to evaluate individual cognitive status, supplementary to neuropsychological testing.

The predictive accuracy of this model, while high, may have suffered slightly from over-fitting. This introduces random error or noise that reduces the performance of the network in making predictions. Over-fitting could be avoided in the future by the use of more advanced machine learning algorithms, such as support or relevance vector machines, or by the inclusion of a larger proportion of PD-N and PDD subjects. This may allow the formation of a more representative cognition-related network, less affected by noise and outliers, that may further improve the capability of this model in predicting cognition from perfusion data.

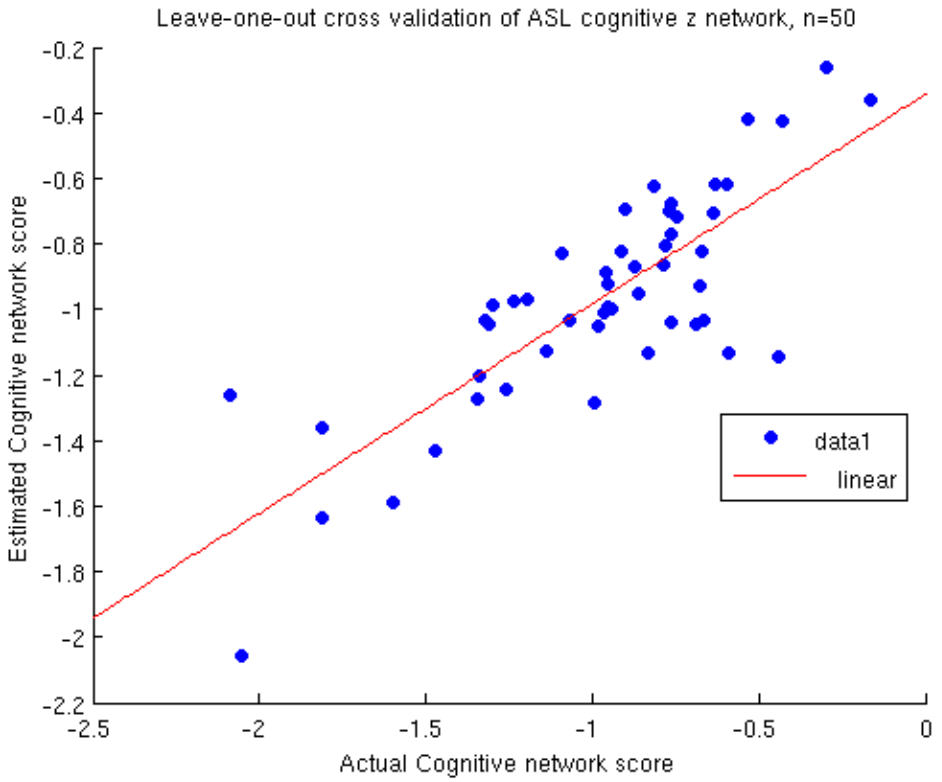

FIGURE 6.15: LOO cross-validation carried out on the cognition-related network displayed a strong correlation between the predicted network scores and the actual network scores (r=0.81, p<0.000001). This indicates the cognition-related network model may be well applied in the evaluation of independent datasets outside of this thesis.

6.5.2 PDDRS-related components

Of the 10 principal components entered into linear regression analysis with PDDRS, components 1 (figure 6.13 A) and 3 (figure 6.13 B) were found to be significant (p<0.01). These components explained 23.8 and 10.1% of the variance in the ASL_{non} data respectively. The PC's were used in linear combination to form a characteristic PDDRS-related

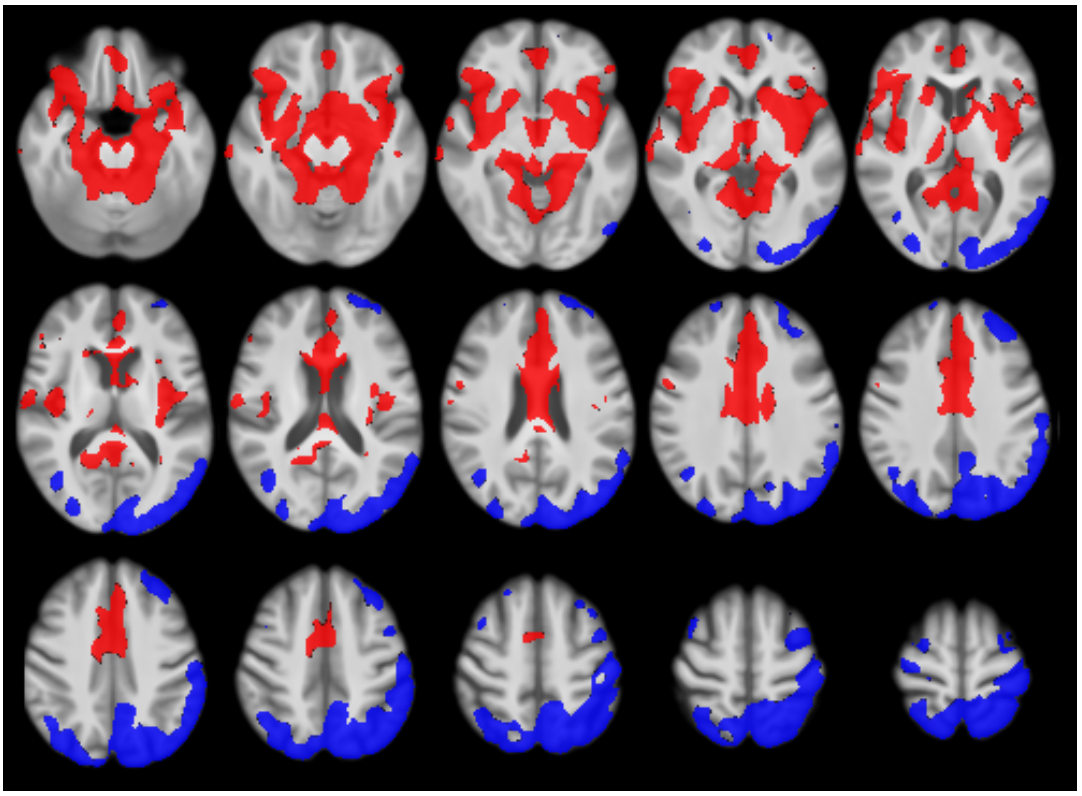

FIGURE 6.16: PDDRS-related perfusion network created by the bootstrap estimation procedure. Perfusion deficits were located primarily in the posterior bilateral occipital cortex and left superior parietal lobule, extending through the post-central, middle-frontal and superior frontal gyri. Preserved perfusion was located anterior cingulate and paracingulate gyri, with some involvement in the frontal medial and frontal orbital cortex.

ASL perfusion network, using the correlation coefficients from the regression (1 and 3; β = 1.48, 1.11).

Regions described by the positive ($z > 1.96$) and negative ($z < -1.96$) voxel loadings were examined as before, this time ordering the mean values given by the positive and negative regions by increasing PDDRS. Thus, the first group of voxel values within each region has a lower mean PDDRS than the second group, separated at the median PDDRS. Examining the area described by the negative loadings, the mean of the first group was found to be higher than the mean of the second group, corresponding to decreasing perfusion with increasing PDDRS. The areas described by the positive loadings were found to correspond to preserved perfusion in the subject data. Negative loadings were thus coloured blue to indicate perfusion deficits, while the positive loadings indicating preserved perfusion were coloured red.

Network reliability and validation

The bootstrap estimation procedure was employed once again, yielding a population standard deviation for the PDDRS network from resampled statistics. The bootstrap PDDRS network, given by dividing the original PDDRS network by the derived standard deviation, is given in figure 6.16. This network demonstrated decreased perfusion in the posterior bilateral occipital cortex, precuneus, left supramarginal and angular gyri, left superior parietal lobule and the frontal pole, with some involvement in the post central, midfrontal and superior frontal gyri. The network showed preserved perfusion relating to PDDRS primarily in the anterior cingulate and paracingulate gyri, with some involvement in the frontal medial and frontal orbital cortex. Decreased and preserved perfusion in the areas defined by this pattern was associated with a higher risk of development of dementia.

Visually, the PDDRS network appears less noisy than the cognition-related network, which may relate to an improved performance of the model in predicting network score from perfusion data outside of this subject group. Leave-one-out cross validation gave an

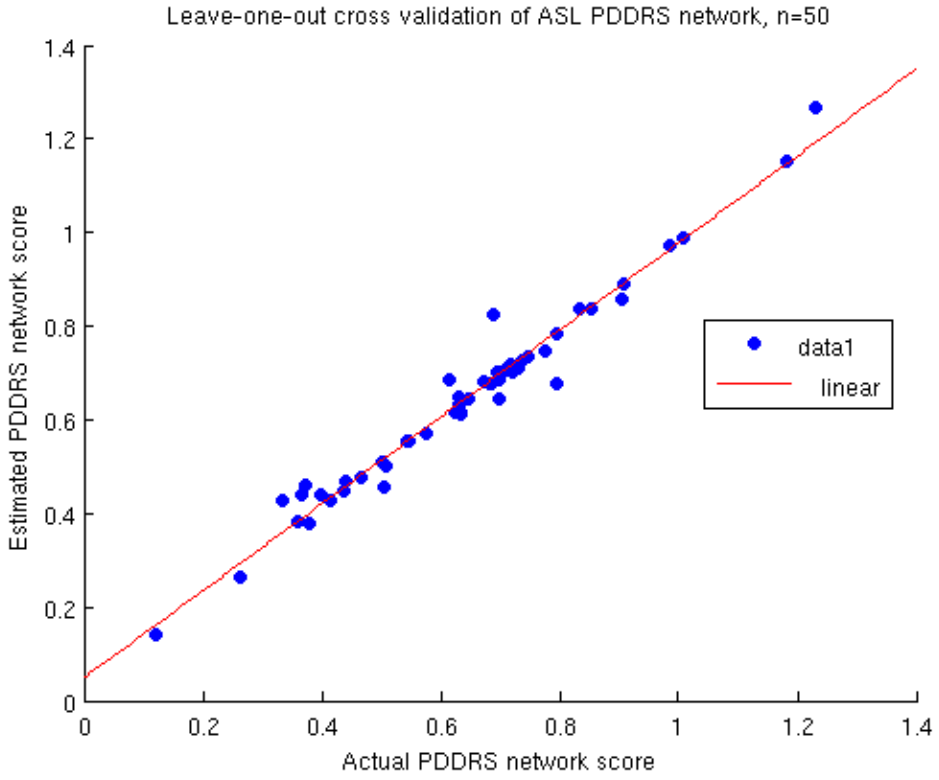

FIGURE 6.17: LOO cross-validation carried out on the PDDRS-related network displayed excellent correlation between the predicted network scores and the actual network scores (r=0.98, p< 0.000001).

almost perfect correlation between the predicted PDDRS network scores and the observed network scores for this subject group (coefficient of correlation r=0.98, p< 0.000001). This finding suggests that cortical perfusion changes in PD have an even stronger and more stable association with the risk of conversion to dementia than with cognition. This is compelling, as a PDDRS network such as that derived in the current work could be quickly and easily evaluated in individuals undergoing routine MRI, prior to cognitive screening.

While neuropsychological testing will always be necessary to complete a full patient evaluation, the PDDRS network expression may present an extremely useful first-pass screening measure to help identify those at imminent risk of developing dementia. Additionally, the model used to calculate PDDRS from subject data may benefit from the inclusion of perfusion information as a significant and stable predictor of imminent conversion, given the strong positive results in this thesis.

6.6 Strengths, limitations and future work

The current work adds to existing perfusion literature, examining a reasonably large sample size of 50 well characterised subjects. It was initially intended to include data from 85 subjects in the analysis, however numerous delays in scanning reduced the number of subjects that could feasibly be included within the time-frame of this thesis. A subject group of 50 subjects was sufficient to obtain significant results. Notably, an association of cognitive dysfunction with decreased perfusion in posterior parietal regions replicated previous work (T. Melzer et al., 2011), and was well supported by the results of linear regression and cognition-related network analysis with this subject group. The inclusion of more subjects in future analysis may strengthen this finding and reduce the affect of noise and random error in the cognition-related network model.

The correlation of PDDRS with ASL-derived perfusion in PD-MCI had not been examined prior to this study. A significant negative correlation of PDDRS with perfusion was found in the posterior bilateral occipital cortex and precuneus, relating to decreased perfusion in these areas for this subject group. The current work introduces the possibility of using perfusion information to infer not only current cognitive status, but also the individualised risk of imminent future conversion to dementia. The results presented here justify the

inclusion of perfusion information in the predictive model used to calculate PDDRS, which may improve the sensitivity of the model in screening for at-risk individuals.

Early-phase FBB PET was examined as a novel method of perfusion imaging; here, key issues were highlighted concerning the choice of scan time as it relates to the biological measure obtained. It was hypothesised that a blood pool effect may mask perfusion information due to non-optimal selection of time-frame for the summed PET image. Had the 2-3 minute patient set-up time been accounted for initially, this blood pool effect might not have limited the results obtained from early-phase FBB PET. However, the blood pool hypothesis may present an interesting and worthwhile area of future investigation, regarding the physiological information obtained from different dynamic time frames within the first 10 minutes of FBB PET imaging.

The lack of correlation between the FBB and ASL-derived data could also be due in part to the sensitivity of perfusion data to state changes. Factors such as the time of day, drowsiness, caffeine ingestion and eye status can effect regional cerebral perfusion (Poudel et al., 1994)(Haller et al., 2013). MRI and PET data were acquired on different days, and without controlling for these factors; therefore, there may have been some unaccounted-for variation in the data that reduced the strength of the correlation.

This thesis was limited by a lack of range in cognitive status, due to the inclusion of predominantly PD-MCI patients in the subject group. This may have affected the reliability of the cognition-related network model, as a result of slight overfitting of the data reducing the prediction accuracy in subjects outside of the studied group. The PDDRS-related network did not seem to be affected by this, suggesting that the association of perfusion with PDDRS is more stable than the association with the global cognitive measure used here, and is less affected by outliers. A higher proportion of PD-N and PDD participants were unable to be included in this thesis as a result of numerous delays in scanning caused by external factors. Planned future work within the longitudinal study may remedy this issue and produce a more representative cognition-related perfusion network.

The reliability of the network analysis may be further improved by the use of independent component analysis (ICA) instead of PCA to identify meaningful characteristics within the data. It is perhaps more biologically relevant to employ ICA to extract underlying patterns from perfusion data, as ICA rests on the assumption that the signals comprising a dataset are statistically independent and uncorrelated with each other (Stone, 2002).

PCA requires only that they be uncorrelated, which is a relatively weak constraint to impose on this data. It is realistic to assume independent physical processes produce uncorrelated signals. These stronger constraints used by ICA may therefore be well-suited to perfusion data, and yield more robust networks less affected by noise. Future analysis could compare the networks given by PCA and ICA, and determine the most appropriate method for use in network analysis of perfusion imaging.

6.7 Concluding remarks

The primary aim of this thesis was to investigate the use of ASL MRI and early-phase FBB PET in the evaluation of cognitive status and dementia risk, and to create informative perfusion networks from these data. To this end, the results of linear regression analysis with cognitive z-score and PDDRS given by each imaging modality were compared; significant correlation of perfusion with cognition and dementia risk were identified in the ASL data, while this correlation was absent in the FBB-derived data for this cohort. There was also found to be very little voxelwise correlation between the FBB and ASL-derived images. It was proposed that these results may be due to a masking of perfusion information by retained signal, instead resulting in a blood pool image. Examining the kinetics of FBB within different time-frames over the first 10 minutes post-injection may provide valuable insight in regards to functional imaging using early-phase FBB PET. This hypothesis warrants further investigation.

Network analysis employed with the ASL-derived perfusion data revealed significant networks of perfusion relating to cognitive z-score and PDDRS. Both networks displayed significant posterior hypoperfusion, consistent with previous findings. The regions showing perfusion deficits in the cognition and PDDRS networks are believed to be involved with the processing and integration of somatosensory information, visuospatial processing, language, episodic memory, reflections of self and other aspects of higher cognitive function (Tortora & Derrickson, 2012)(Cavanna & Trimble, 2006). The PDDRS-related network may be the most compelling aspect of this thesis, as it represents a promising avenue of evaluating disease severity and future dementia risk.

Early-phase PET and ASL MRI present exciting opportunities in terms of the future of neuroimaging and the evaluation of disease. This work presents and compares these two

modalities for the first time in the context of cognitive decline and future conversion to dementia, two highly impactful elements of disease burden in PD. While considerable work remains, the results obtained here add to our understanding of the Parkinson's disease neuropathology and underlying functional changes, and raise interesting questions regarding the way early-phase PET data is interpreted. Planned future work may lead to the development of the PDDRS network as a new imaging biomarker of imminent dementia in PD.

Appendix A

Tables and Figures

Executive Function	Attention & working memory	Episodic Memory	Visuospatial	Language
Stroop interference	Digits forwards/backwards	California Verbal Language Test-II Short Form; acquisition, short and long delays	Judgement of line orientation (JLO)	Boston Naming test
Letter fluency	Digit ordering	Rey Complex Figure test; short and long delays	Fragmented letters test	Dementia Rating Scale-2 similarities sub-test
Category fluency	Map search task		Picture completion test	Alzheimer's Dementia Assessment Cognitive Scale; object/finger naming, commands, comprehension, spoken language, word finding difficulties
Category switching	Stroop colour reading		RCF-Copy	
Action fluency	Stroop word reading			
Trails B	Trails A			

FIGURE A.1: The neuropsychiatric test battery consists of a series of test within each of the five cognitive domains.

Anon. ID	NZBRI criteria	Age	Sex	Education	Disease symptom duration	MOCA	UPDRS-III	Attention total	Executive function total	Visuo total	Learning total	Language total	Total all domains	PDDRS
NZ043754	PD-MCI	67	M	14	8	22	26	-1.20	-0.47	0.17	-0.04	-0.67	-0.38	0.05
NZ012804	PD-MCI	72	M	12	8	24	41	0.00	-0.84	-0.20	0.52	-0.60	-0.13	0.74
NZ011098	PD-MCI	76	F	13	15	20	33	-0.27	-1.81	-1.67	-0.66	-0.57	-1.10	0.70
NZ053680	PD-MCI	75	F	13	23	20	32	-1.32	-1.19	-2.24	-1.10	0.16	-1.46	0.94
NZ062891	PD-MCI	73	M	12	14	23	41	0.53	0.10	-0.21	-1.28	-0.94	-0.21	0.05
NZ070930	PD-MCI	78	F	11	10	26	35	-0.05	-0.87	-0.33	0.78	0.54	-0.12	0.52
NZ003283	PD-MCI	65	M	10	7	24	36	-0.85	-0.66	-0.09	-2.32	-0.15	-0.98	0.25
NZ074618	PD-MCI	68	M	12	13	24	39	-1.17	-1.17	0.24	-0.78	-0.61	-0.72	0.54
NZ065140	PDD	78	M	15	8	20	41	-0.73	-1.09	-0.35	-1.98	-0.57	-1.04	0.96
NZ025117	PD-MCI	59	M	10	5	21	20	-1.29	-1.68	-0.77	-1.62	0.16	-1.34	0.95
NZ063968	PD-MCI	75	F	10	9	23	23	-0.38	-0.61	-0.08	-1.62	-0.83	-0.67	0.54
NZ040704	PD-MCI	74	M	11	10	19	36	-1.60	-2.23	-1.74	-1.30	-1.49	-1.72	0.99
NZ038593	PDD	79	M	11	15	16	61	-1.47	-1.76	-2.22	-1.72	-0.80	-1.79	0.99
NZ012899	PD-MCI	75	M	10	4	25	33	-0.46	-0.94	-1.20	-0.72	-0.39	-0.83	0.85
NZ000681	PD-MCI	72	M	10	21	21	26	-1.04	-1.36	-1.01	-2.09	-0.60	-1.38	0.78
NZ053551	PD-MCI	71	F	15	4	19	13	-2.04	-1.88	-1.33	-1.86	-0.55	-1.78	0.99
NZ032484	PD-MCI	74	M	16	5	22	35	-1.12	-0.97	0.08	-0.90	-1.56	-0.73	0.52
NZ075876	PD-MCI	73	M	11	5	18	49	-1.21	-1.93	-2.03	-2.16	-0.60	-1.83	0.97
NZ021748	PD-MCI	73	M	9	3	16	23	-2.47	-2.08	-1.48	-1.08	-1.49	-1.78	0.99
NZ063658	PD-MCI	73	F	10	2	15	29	-0.82	-1.02	-1.46	-2.32	-0.27	-1.40	0.84
NZ074394	PD-MCI	76	M	16	6	28	40	-1.63	-1.58	-0.18	0.24	0.13	-0.79	0.96
NZ077668	PD-MCI	79	M	16	10	24	59	-1.89	-1.54	-1.34	0.22	-0.02	-1.14	0.97
NZ078926	PD-MCI	74	M	10	9	16	49	-1.56	-1.73	-0.94	-1.18	-1.26	-1.35	0.99
NZ077039	PD-N	73	M	12	11	27	47	-0.72	-0.10	0.93	0.84	0.51	0.24	0.10
NZ014157	PD-MCI	63	M	10	20	23	56	-0.91	-1.38	-0.97	-0.88	-0.70	-1.03	0.73
NZ038093	PD-N	74	F	16	10	27	25	0.38	0.72	1.02	0.34	0.06	0.62	0.10
NZ023006	PD-MCI	86	M	13	6	23	43	-1.49	-1.38	0.33	-1.30	-0.24	-0.96	0.96
NZ011417	PD-MCI	60	F	11	13	26	46	-0.68	-1.07	-1.31	-0.20	0.16	-0.82	0.11
NZ076505	PD-MCI	67	M	11	5	22	44	-1.49	-1.54	-0.36	-0.84	-0.61	-1.06	0.90
NZ042591	PD-MCI	75	M	10	4	17	51	-1.51	-2.00	-1.67	-0.34	-0.50	-1.38	1.00
NZ035224	PD-MCI	66	M	18	5	19	25	-0.37	-0.38	-0.04	-0.76	-0.67	-0.39	0.14
NZ030907	PD-N	71	M	15	20	26	68	-0.54	-0.40	-0.45	-0.10	-0.64	-0.37	0.30
NZ030278	PD-MCI	70	M	15	10	21	35	-0.74	-1.49	-0.72	-0.98	-0.90	-0.98	0.58
NZ012046	PD-MCI	74	M	18	5	25	19	-0.36	-0.75	0.10	-1.28	-0.71	-0.57	0.17
NZ039222	PD-MCI	74	M	11	2	25	62	-0.52	-0.81	-0.22	0.06	0.18	-0.37	0.46
NZ082390	PD-MCI	77	M	11	1	24	35	-1.08	-1.53	-0.64	-1.48	-0.06	-1.18	0.96
NZ052698	PDD	84	M	13	3	20	65	-2.61	-2.06	-1.71	-0.62	-0.83	-1.75	1.00
NZ030373	PD-MCI	75	M	11	6	20	36	-0.69	-0.67	-1.43	-1.58	-1.16	-1.09	0.33
NZ078435	PD-MCI	78	F	11	13	24	52	-0.42	-0.73	-0.12	-1.18	0.20	-0.61	0.68
NZ034595	PD-MCI	64	M	10	4	23	43	-1.60	-1.66	-0.17	-0.28	-1.56	-0.93	0.57
NZ061547	PD-MCI	71	M	15	16	27	46	-0.19	-0.21	-1.16	-1.44	0.24	-0.75	0.14
NZ084406	PD-MCI	74	M	11	17	24	24	-0.86	0.48	-1.25	-0.50	-0.16	-0.53	0.42
NZ030726	PD-N	84	M	13	12	25	58	-0.05	-0.07	-0.66	1.54	0.54	0.19	0.49
NZ057325	PD-MCI	79	M	19	4	23	64	-1.05	-0.76	-0.38	-0.28	-0.66	-0.62	0.69
NZ069543	PDD	68	M	11	4	16	57	-1.99	-2.28	-2.54	-2.42	-1.17	-2.31	0.99
NZ060065	PD-MCI	78	M	10	5	23	42	-0.82	-1.21	0.19	-1.02	0.20	-0.71	0.37
NZ079021	PD-MCI	82	M	17	5	20	41	-0.55	-0.26	-1.27	-1.62	-1.37	-0.92	0.39
NZ003197	PD-MCI	69	M	14	5	16	39	-2.67	-2.64	-2.24	-2.22	-2.00	-2.44	0.99
NZ017526	PD-MCI	63	F	12	15	25	65	-0.72	-1.07	-1.29	-1.36	-0.26	-1.11	0.43
NZ002568	PDD	79	M	12	3	12	38	-2.95	-2.52	-1.83	-1.76	-2.56	-2.26	1.00

FIGURE A.2: Participant neuropsychiatric results (z-score) and demographics.

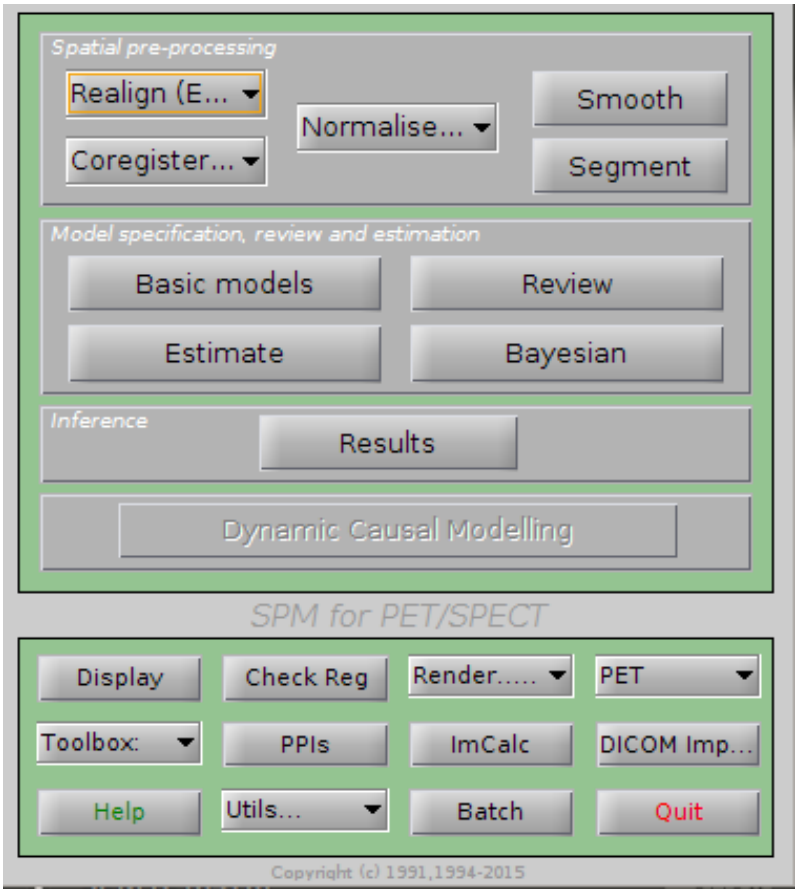

FIGURE A.3: The SPM12 graphical user interface (GUI), employed here to carry out pre-processing on PET and MRI data.

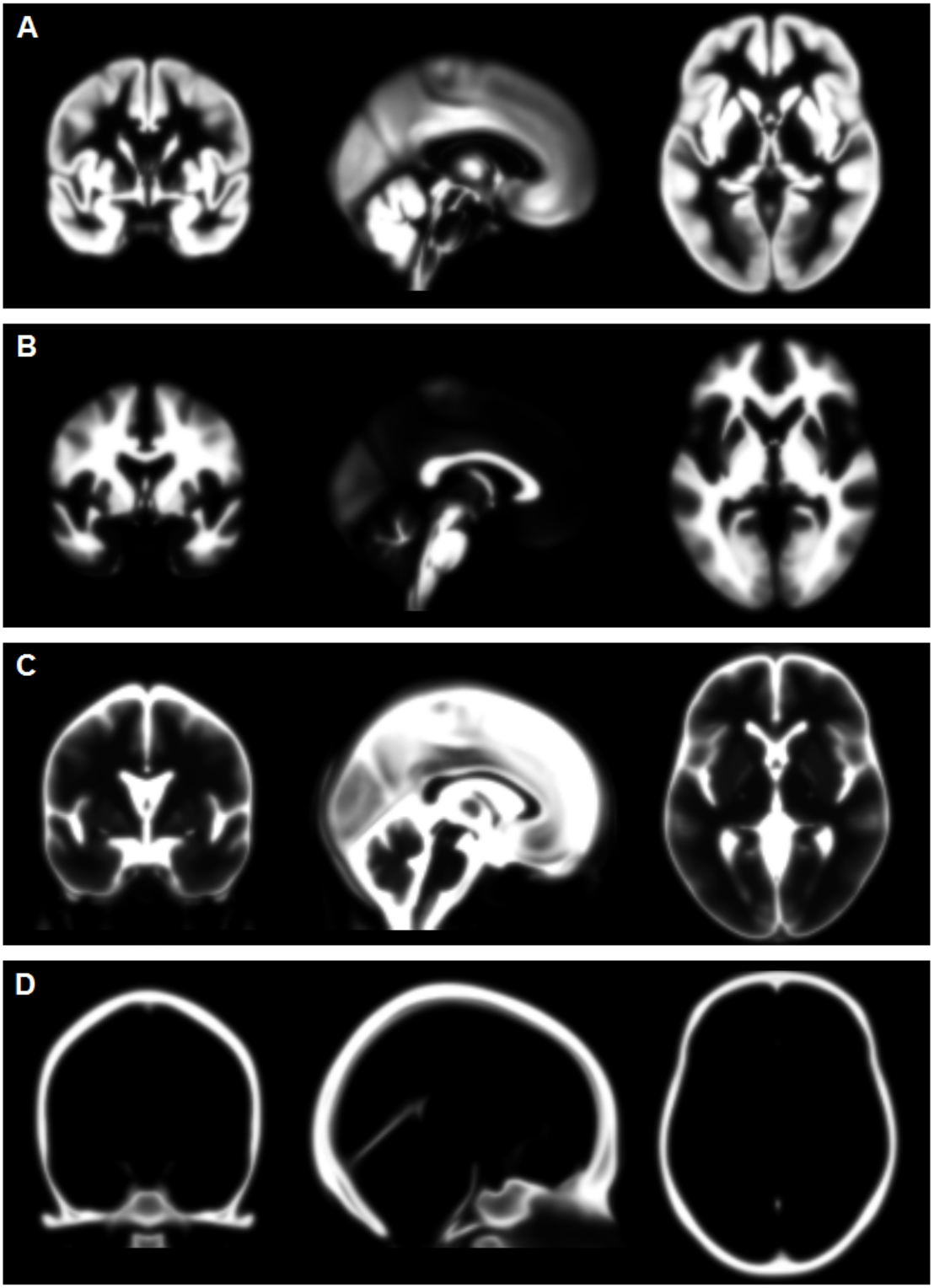

FIGURE A.4: The tissue probability maps (TPMs) for a) grey matter, b) white matter, c) cerebrospinal fluid and d) bone. The TPMs for skin and air are also used in the SPM segmentation routine but are not included here.

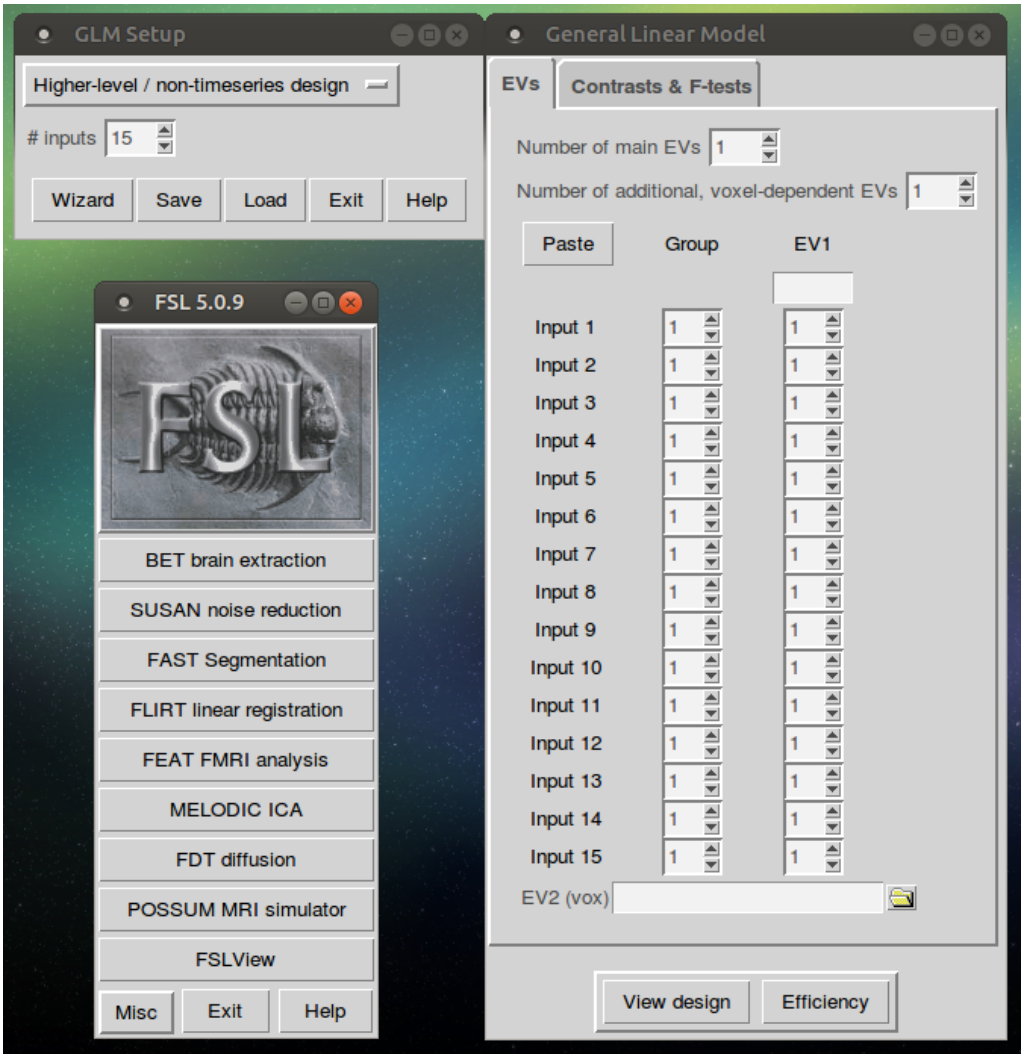

FIGURE A.5: The FSL GLM graphical user interface (GUI), demonstrating the options for a higher-level/non-timeseries design. The number of main EV's can be changed to allow multiple tested effects and confounds, entered as discrete data. Voxel dependent EV's are input as a 4D image file, with dimensions matching exactly that of the data the EV is being compared to.

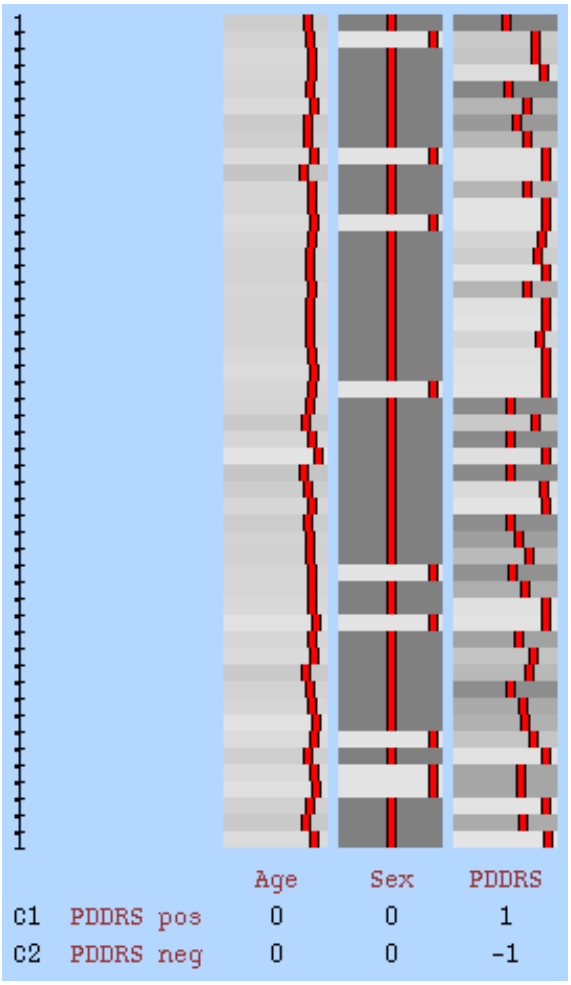

FIGURE A.6: The design matrix implemented by FSL's Randomise, with Parkinson's disease dementia risk score (PDDRS) as the tested covariate and age and sex as confounds. Significant results on the negative contrast indicate decreased voxel values with increased PDDRS. For the ASL perfusion data, this may indicate decreased perfusion corresponding to increased risk of conversion to dementia.

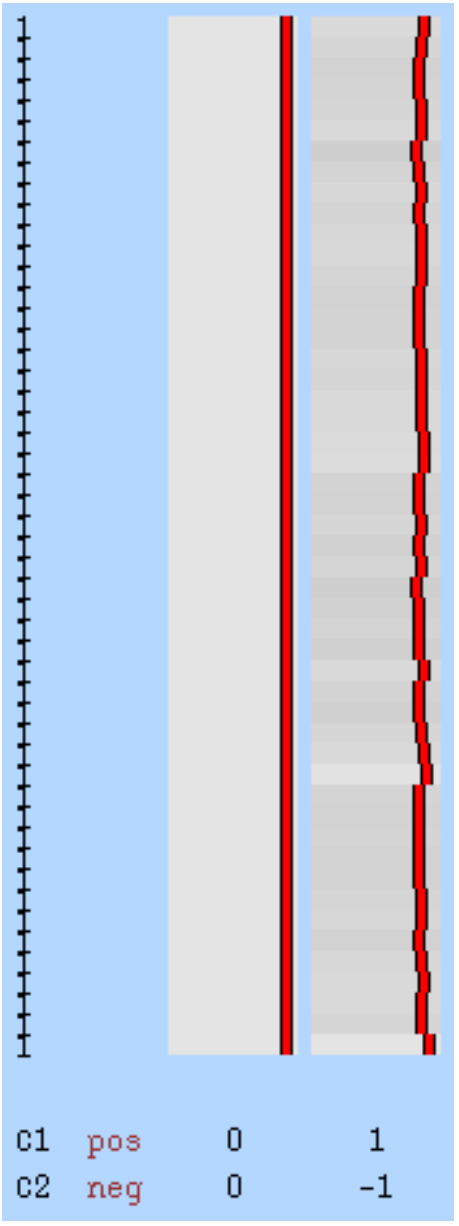

FIGURE A.7: This design matrix, created using FSL's GLM graphical user interface, specifies the ASL_{GM} 4D image file as a voxel-dependent explanatory variable, represented graphically here by the mean value across all voxels. The FBB_{GM} images input into Randomise are compared voxel-by-voxel with the corresponding ASL_{GM} images, using permutation inference with threshold-free cluster enhancement. Both positive and negative voxelwise correlation are tested using the contrasts specified in this design.

Appendix B

Supporting figures

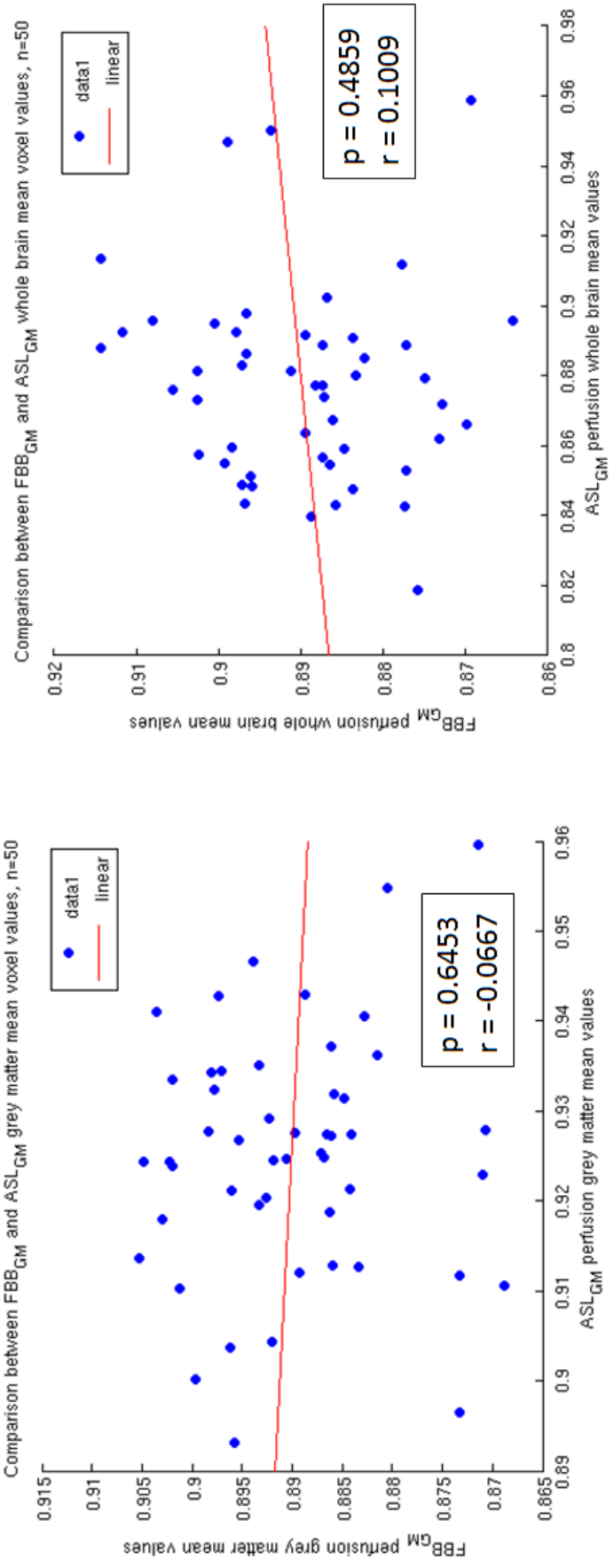

FIGURE B.1: Regional mean values extracted from FBB$_{GM}$ and ASL$_{GM}$ were examined for correlation. There was no significant correlation found between the two modalities in the (left) grey matter or (right) whole brain.

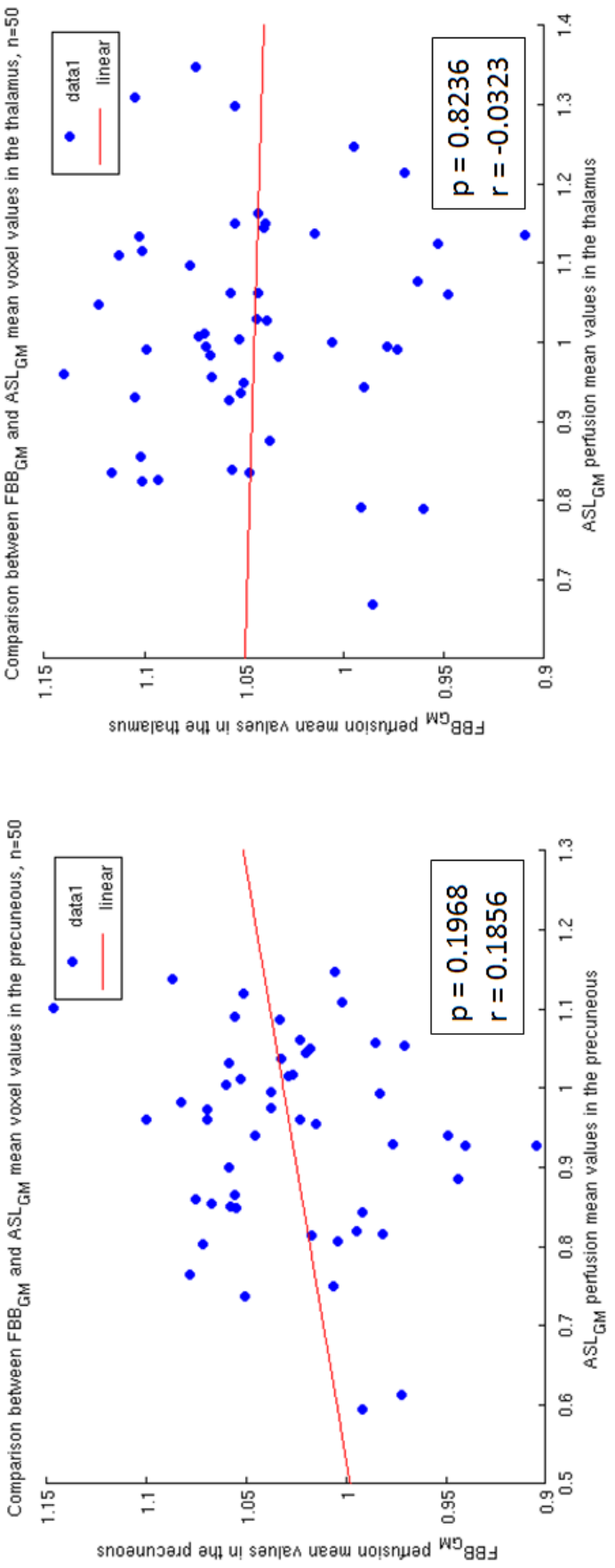

FIGURE B.2: Regional mean values extracted from FBB$_{GM}$ and ASL$_{GM}$ were examined for correlation. There was no significant correlation found between the two modalities in the (left) precuneus or (right) thalamus.

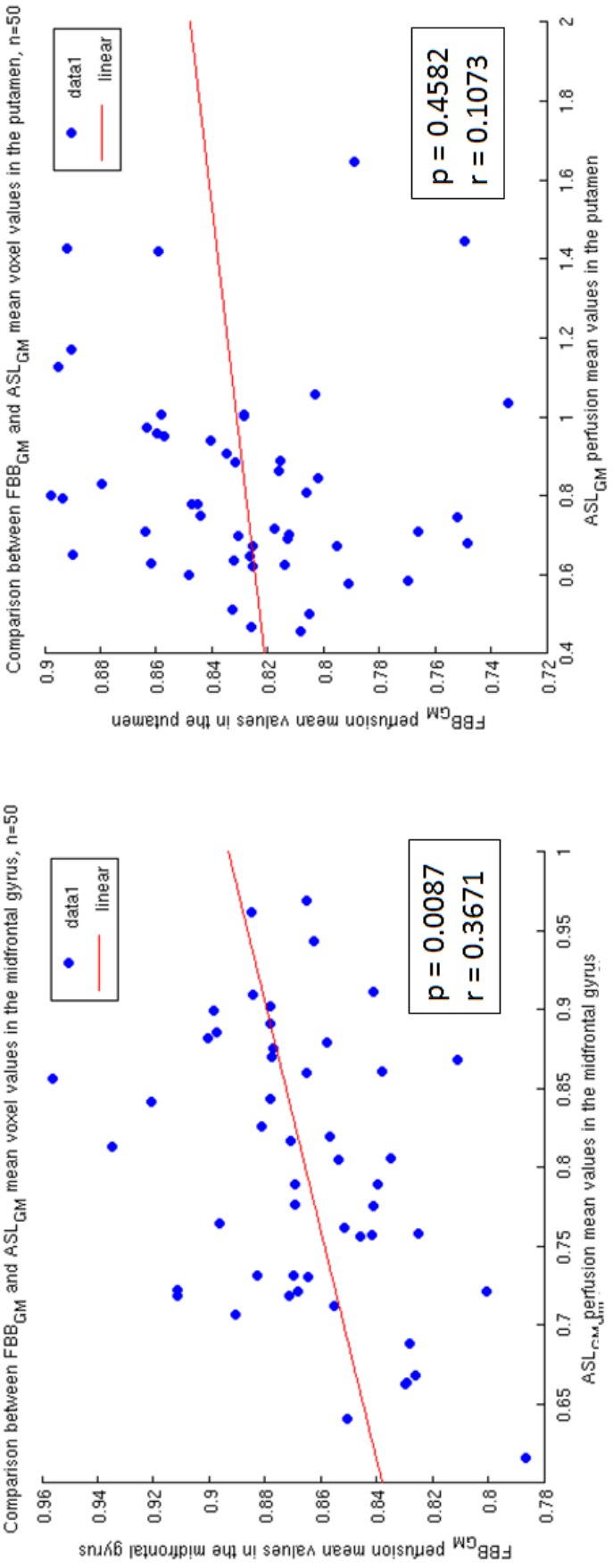

FIGURE B.3: Regional mean values extracted from FBB_{GM} and ASL_{GM} were examined for correlation. There was significant correlation between the two modalities in the (left) midfrontal gyrus, but no significant correlation in the (right) putamen.

Appendix C

Matlab Code

Here I have included two scripts that were employed in this thesis. The SUVR creation script was used to normalise the images to a chosen reference region.

The PCA function carried out principal component analysis on the data, followed by a logistic regression to identify significant PC's relating to the chosen covariate. The bootstrap and LOO procedures employed very similar methods as those used in this function, modified to resample the data and compute individual network expression.

Other scripts were used to stream-line preprocessing, but were not included here.

SUVR creation script:

```
%% SUVR: Normalise images to cerebellum or global grey matter

% This script takes an input image and normalises it by the mean grey matter
% voxel value within a chosen mask. Here, SUVR images are created from FBB
% tofac images by normalising to the mean value in the cerebellar grey
% matter or global grey matter. ASL perfusion images are left non normalised
% or normalised to global grey matter.

%%

spm('Defaults','pet');
 !source /etc/profile.d/fsl.sh

%Set working directory. This directory contains all subject image data
%within MRI series folders.
direct = '/data/analysis/pet-fbb/MRI_m/';
```

```
%Define MRI scan numbers
input = [
];

scan_num = num2str(input(:,1));

for i =1:size(scan_num,1)

%Uncomment either tofac or ecqCBF.
  %warped tofac image.
  vph1 = spm_vol(spm_select('FPList',[direct scan_num(i,:)],'^wperf_tofac.*.nii$'));
  hot1 = spm_read_vols(vph1);
  %warped ecqCBF image
  vph1 = spm_vol(spm_select('FPList',[direct scan_num(i,:)],'^wecq.*.nii$'));
  hot1 = spm_read_vols(vph1);

%Grab the GM image produced by segmentation step
  vph2 = spm_vol(spm_select('FPList',[direct scan_num(i,:)],'^mwc1ds.*.nii$'));
  hot2 = spm_read_vols(vph2);

%Uncomment the appropriate mask.
  %Cerebellum mask.
  vph3 = spm_vol('/.../r_cerebellum_mask.nii');
  %Global GM mask
  vph3 = spm_vol('/.../maskGM_s4_m0wrp1ds_cut.nii');

  hot3 = spm_read_vols(vph3);

%Deal with NaN.
  hot1(isnan(hot1))=0;

%Grab voxels that have a >90% chance of being grey matter (as defined by
%the subject grey matter segment image) that are within the chosen mask.
  gm = (hot3>0) & (hot2>0.1);

%Get mean PET or ASL voxel value within the chosen region.
  avg_pet_gm = mean(hot1(gm));

%Create SUVR by dividing by the avg_pet_wm value.
  suvr_pet = hot1/avg_pet_wm;

%**********************************
% Write as image.

[pth nam] = spm_fileparts(vph1.fname);
s = regexp(nam,'\_', 'split');
vph1.dt = [16 1];
```

```
%normalising wperf_tofac to whole brain GM
vph1.fname = [pth filesep 'suvr_GMnorm_wperf_tofac_' char(s(3)) '.nii'];

%normalising wperf_tofac to cerebrellum
vph1.fname = [pth filesep 'suvr_wperf_tofac_' char(s(3)) '.nii'];

%normalising wecqCBF to whole brain GM
vph1.fname = [pth filesep 'wecqCBF_GMnorm_' char(s(2)) '.nii'];
spm_write_vol(vph1, suvr_pet);

disp(sprintf('%d SUVR images created',i));
end
```

PCA network creation function, with logistic regression:

```
function [srp_r_c,c,es,s_es,vs,scvs,pat,col_av,col_std,inputfile,net] = spm_pca_linear_AB
%-----------------------------------------------------------------------
% 2015 - Tracy Melzer, Megan Stark
% Original by Richard Watts (2010)
%-----------------------------------------------------------------------
% Output variables:
% srp = subject residual profile: the twice demeaned data
% c = covariance matrix
% es = vector of eigenvalues associated with eigenvectors(principal
% components) 100*(es)/sum(es) = %variance explained by each of the
% components.
% s_es = scaled eigenvalues
% vs = Eigenvectors (expression or 'score' of each component)
% scvs = scaled eigenvectors--These represent the expression of each PC in
% each individual.
% pat = [#voxels x #subject] matrix of linear principal components:
%       First column is PC1, second column is PC2, etc...pat is saved as
%       'pattern_matrix' in the current working directory (line 255)
% col_av = group average (if ASL, average CBF of entire group)
% col_std = group standard deviation
% inputfile = list of images used in the analysis
%
% Saved Variables:
% pca### = Principal Component images
% average_lin = group average brain image (average at each voxel)
% std_lin = standard deviation image for the group (std at each voxel)
%-----------------------------------------------------------------------
% This script uses a Grey Matter (GM) mask to restrict analysis to GM
% perfusion (avoid the need to log transform the input data).
%-----------------------------------------------------------------------
```

```
%Things that can/need to be changed in this script depending on use:
% 1. nComponents: Sets the number of Principal Component image to write out
% 2. mask: Study specific GM mask (or other mask)
% 3. out_direct: set the location of the PC images written out
% 4. group: covariate to use in logistic regression with PCs to form
% network

%set number of PCs to use in logistic regression and to write out. Can
%change this according to how many PC's make up 67% of the variance.
nComponents = 15;

%use the oxford mask defining mean GM (modulated normalised)
mask = spm_vol('/.../maskGM_s4_m0wrp1ds_cut.nii');

%Specify output directory
out_direct = '/.../PCA';

%spm_select opens dialogue window to select study images
[inputfile sts] = spm_select(inf, 'image', 'Select input images for PCA');
v = spm_vol(inputfile);

%-----------------------------------------------------------------------
%Import mask
y_mask = spm_read_vols(mask);

%***********************************************************************

%Find the voxels in/out of the mask.
ind_out = find(y_mask==0);  %Voxels outside the brain.
ind_in = find(y_mask);      %Voxels inside the brain.

fprintf('Reading files\n');
%***********************************************************************

%Pre-define srp and define vols = number of subjects (images) in the analysis
vols = size(v,1);
zrp = zeros(vols,size(ind_in,1));
srp = zeros(vols,size(ind_in,1));
srp_r = zeros(vols,size(ind_in,1));
srp_r_c = zeros(vols,size(ind_in,1));

k=1;
%Sets up linear indexing and excludes voxels not part of GM.
for j = 1:size(v,1)
    y = spm_read_vols(v(j));

    %Exclude non-GM voxels
    z = y(ind_in);
```

```
    zrp(k,:) = reshape(z,1,[]);
    k=k+1;
end

%Find any values equal to zero or NaN and set them to 1, otherwise log transform
%won't work. Zeros and NaN's arise due to coregistration.
a = find(zrp<=0);
zrp(a)=1;
ns = isnan(zrp);
zrp(ns)=0;

srp=log(zrp);

%Calculate Row mean (subject mean)
row_av = mean(srp,2);

fprintf('Subtracting mean image\n');
%1: subject de-mean 2: group de-mean
%Subtract row averages (subject average) so that voxel values represent
%within-subject derivations from the mean of the subject image.

for ii = 1:vols
    srp_r(ii,:) = (srp(ii,:)-row_av(ii));
end

%Columns are then averaged to create a characteristic mean image vector for
%the group.  The column averages are subtracted from the individual matrix
%entries to produce a matrix of 'residual' images termed the subject
%residual profile (SRP). This represents the matrix of deviations from the
%subject and group means.

col_av = mean(srp_r,1);
col_std = std(srp_r,0,1);

%Demean and Normalize standard deviation to 1.
for jj = 1:size(srp,2)
    srp_r_c(:,jj) = (srp_r(:,jj)-col_av(jj));
end

%A covariance matrix is contstructed from the subject residual prodiles by
%computing the covariance between each pair of SRP matrix rows. divide by
%'n' not 'n-1'.
fprintf('Calculating covariance matrix\n');

c = zeros(vols,vols);
for ix=1:vols
    for iy=ix:vols
```

```
        c(ix,iy) = sum(srp_r_c(ix,:).*srp_r_c(iy,:))/(vols-1);
        c(iy,ix) = c(ix,iy);
    end
end

fprintf('Calculating and sorting eigenvalues and eigenvectors\n');
[vo,d] = eig(c);
[t,index] = sort(diag(d));          % Sorts eigenvalues into ascending order
index(:) = size(srp,1)-index(:)+1;    % Descending order index
vs(:,:) = vo(:,index);               % Sort eigenvectors
es = t(size(srp,1):-1:1);             % Sort eigenvalues

%take absolute value of eigenvalues
es = abs(es);
fprintf('Creating eigenvector images\n');

%**************************************************************************

vols = size(v,1);
zrp = zeros(vols,size(ind_in,1));
srp = zeros(vols,size(ind_in,1));
srp_r = zeros(vols,size(ind_in,1));
srp_r_c = zeros(vols,size(ind_in,1));

%#of components for log reg
comp = 12;

%set up group variable for logistic regression
group = zeros(vols,1);

k=1;

% %sets up GM mask
%Sets up linear indexing and excludes voxels not part of GM.
for j = 1:size(v,1)
    y = spm_read_vols(v(j));

    z = y(ind_in);
    zrp(k,:) = reshape(z,1,[]);
    k=k+1;
end

%log transform the data
a = find(zrp<=0);
zrp(a)=1;
srp = log(zrp);

%if using just values of interest (ind_in), then calculating subject rows:
```

```
row_av = mean(srp,2);

%subtract row averages so that voxel values represent within-subject
%deviations from the mean of the subject log image.
for ii = 1:vols
    srp_r(ii,:) = (srp(ii,:)-row_av(ii));
end

col_av = mean(srp_r,1);
col_std = std(srp_r,0,1);

%Demean group average (not using stdeviation right now)
for jj = 1:size(srp,2)
    srp_r_c(:,jj) = (srp_r(:,jj)-col_av(jj));%./col_std(jj);
end
%covariance matrix
c = zeros(vols,vols);
for ix=1:vols
    for iy=ix:vols
        c(ix,iy) = mean(srp_r_c(ix,:).*srp_r_c(iy,:));
        c(iy,ix) = c(ix,iy);
    end
end
%fprintf('Calculating and sorting eigenvalues and eigenvectors\n');
[vo,d] = eig(c);
[t,index] = sort(diag(d));          % Sorts eigenvalues into ascending order
index(:) = size(srp,1)-index(:)+1;    % Descending order index
vs(:,:) = vo(:,index);               % Sort eigenvectors
es = t(size(srp,1):-1:1);             % Sort eigenvalues

% need absolute value of eigenvalues
es = abs(es);
%Weight by the sqrt of eigenvalue
s_es = sqrt(es);

%Create the scaled Eigenvectors: Scale by square root of eigenvalue.
%Mult when calculating log reg and div when calculating PC's. Use divide to
%set variance of patterns (PC's) to one.

scvs = zeros(size(vs));
scvs_div = zeros(size(vs));
tvs = vs';
for h = 1:vols
    scvs(:,h) = vs(:,h)*s_es(h);
    scvs_div(:,h) = vs(:,h)/s_es(h);
    scvs_trans(h,:) = s_es(h)*tvs(h,:);
end
```

```
%Create the PC's by multiplying the transpose of the SRP matrix by the
%scaled eighenvectors.

pat = srp_r_c'*scvs_div;


%Write out the PC's for nComponents
[pth,nam,ext,num] = spm_fileparts(v(1).fname);

%% Write out the PC's for nComponents
pat_vol = zeros((v(1).dim(1)*v(1).dim(2)*v(1).dim(3)),vols);

for i = 1:vols
    mid = pat_vol(:,i);
    mid(ind_in) = pat(:,i);
    pat_vol(:,i) = mid;
end

for component = 1:nComponents
    network_volume = reshape(pat_vol(:,component),v(1).dim(1),v(1).dim(2),v(1).dim(3));
    mask.fname = [out_direct 'pc' sprintf('%.3d', component) ext];
    mask.dt = [16 0];
    spm_write_vol(mask, network_volume);
end

%Write out mean vol and standard deviation: First reshape row vectors
%into 3D volume.
mean_mid = zeros((v(1).dim(1)*v(1).dim(2)*v(1).dim(3)),1);
std_mid = zeros((v(1).dim(1)*v(1).dim(2)*v(1).dim(3)),1);

%Assign values to 3D volume
mean_mid(ind_in) = col_av;

%std_mid = col_std;
std_mid(ind_in) = col_std;

%Write out volumes in output directory.
meanim = reshape(mean_mid,v(1).dim(1),v(1).dim(2),v(1).dim(3));
mask.fname = [out_direct 'average_lin' ext];
mask.dt = [16 0];
spm_write_vol(mask, meanim);

stdim = reshape(std_mid,v(1).dim(1),v(1).dim(2),v(1).dim(3));
mask.fname = [out_direct 'std_lin' ext];
mask.dt = [16 0];
spm_write_vol(mask, stdim);

%% stepwise logistic
```

```
% Set up group variable for logistic regression. Either cognitive z score
% or PDDRS, input values into group and change output PCA network file name
% accordingly (below)

group = [
];

%Stepwisefit runs the logistic regression
[b,se,pval,inmodel,stats,nextstep,history] = stepwisefit(scvs(:,1:nComponents),group);

%Output coefficients, intercept and PC expression from the logistic
%regression with the group variable
betas = inmodel(:).*b(:);
intercept = stats.intercept;
net = stats.intercept + scvs(:,1:nComponents)*betas;

%Create the network

net_im = stats.intercept + pat(:,1:nComponents)*betas;

av_net = mean(net_im);
st_net = std(net_im);

newnet = (net_im-av_net)/st_net;
newnet_lin_im = zeros((v(1).dim(1)*v(1).dim(2)*v(1).dim(3)),1);
net_lin_im_im = zeros((v(1).dim(1)*v(1).dim(2)*v(1).dim(3)),1);

newnet_lin_im(ind_in) = newnet;
net_lin_im_im(ind_in) = net_im;

newnet_im = reshape(newnet_lin_im,v(1).dim(1),v(1).dim(2),v(1).dim(3));
net_im_im = reshape(net_lin_im_im,v(1).dim(1),v(1).dim(2),v(1).dim(3));

%Write out new network as NIFTI. Change network name (cogZ/pddrs)

v(1).fname = [out_direct '/cogZ_network.nii'];
v(1).dt = [16 0];
spm_write_vol(v(1), newnet_im);

v(1).fname = [out_direct '/net_image.nii'];
v(1).dt = [16 0];
spm_write_vol(v(1),net_im_im);

fprintf('Done\n');
```

References

Aarsland, D., & Kurz, M. W. (2010, May). The epidemiology of dementia associated with parkinson's disease. *Brain Pathology*, *20*(3), 633-639. doi: 10.1111/j.1750-3639.2009.00369.x

Alves, G., Forsaa, E. B., Pederson, K. G., Gjerstad, M. D., & Larsen, I. P. (2008, September). Epidemiology of parkinson's disease. *J Neurol*, *255*(5), 18-32. doi: 10.1007/s00415-008-5004-3

Anderson, T., Myall, D., Wood, K., Livingston, L., Pitcher, T., Melzer, T., ... Dalrymple-Alford, J. (n.d.). *Individualised medicine: Predicting dementia in parkinsons disease.*

Anderson, T. J. (2013). *Genetics, brain imaging, and cognitive decline in parkinson's disease.* Research Project Full Application (GA214F) to the Health Research Council of New Zealand.

Ashburner, J. (2007, Oct 15). A fast diffeomorphic image registration algorithm. *NeuroImage*, *38*(1), 95-113. doi: 10.1016/j.neuroimage.2007.07.007

Ashburner, J., Barnes, G., Chen, C. C., Daunizeau, J., Flandin, G., Friston, K., ... Zeidman, P. (2015, May). Spm12 manual [Computer software manual]. Retrieved from http://www.fil.ion.ucl.ac.uk/spm/doc/manual.pdf

Bach, J., Ziegler, U., Deuschl, G., Dodel, R., & DoblhammerReiter, G. (2011, October). Projected numbers of people with movement disorders in the years 2030 and 2050. *Movement Disorders*, *26*(12), 2286-2290. doi: 10.1002/mds.23878

Brown, R. W., Cheng, Y.-C. N., Haacke, E. M., Thompson, M. R., Venkatesan, R., & service), W. I. O. (2014). *Magnetic resonance imaging: physical principles and*

sequence design (Second ed.). Hoboken, New Jersey: John Wiley & Sons, Inc. doi: 10.1002/9781118633953.ch4

Bushberg, J. T., Seibert, J. A., Jr., E. M. L., & Boone, J. M. (2012). *The essential physics of medical imaging* (Third ed.). Philadelphia, Penssylvania: Lippincott Williams & Wilkins, a Wolters Kluwer business.

Casanova, R., Srikanth, R., Baer, A., Laurienti, P. J., Burdette, J. H., Hayasaka, S., ... Maldjian, J. A. (2007). Biological parametric mapping: A statistical toolbox for multimodality brain image analysis. *NeuroImage*, *34*(1), 137-143. Retrieved from http://search.proquest.com.ezproxy.canterbury.ac.nz/docview/1506713624?accountid=14499

Cavanna, A. E., & Trimble, M. R. (2006). The precuneus: a review of its functional anatomy and behavioural correlates. *Brain*, *129*(3), 564-583. doi: 10.1093/brain/awl004

Collignon, A., Maes, F., Delaere, D., Vandermeulen, D., Suetens, P., & Marchal, G. (1995). Automated multi-modality image registration based on information theory. *In: Bizais*.

Dai, W., Garcia, D., de Bazelaire, C., & Alsop, D. C. (2008, December). Continuous flow-driven inversion for arterial spin labelling using pulsed radio frequency and gradient fields. *Magnetic Resonance in Medicine*, *60*(6), 1488-1497. doi: 10.1002/mrm.21790

de Lau, L. M. L., & Breteler, M. M. B. (2006, June). Epidemiology of parkinson's disease. *Lancet Neurol*, *5*(6), 525-535.

Diaz, N. L., & Waters, C. H. (2009). Current strategies in the treatment of parkinson's disease and a personalized approach to management. *Expert Review of Neurotherapeutics*, *9*(12), 1781-1789. doi: 10.1586/ern.09.117

Dickson, D. W. (2012, August). Parkinson's disease and parkinsonism: Neuropathology. *Cold Spring Harb Perspec Med*, *8*(2), a009258. doi: 10.1101/cshperspect.a009258.

Docherty, M. J., & Burn, D. J. (2010, April). Parkinson's disease dementia. *Curr Neurol Neurosci Rep*, *10*(4), 292-298. doi: 10.1007/s11910-010-0113-7

Eidelberg, D., Moeller, J. R., Ishikawa, T., Dhawan, V., Spetsieris, P., Chaly, T.,

... Fahn, S. (1995). Early differential diagnosis of parkinsons disease with ^{18}f-fluorodeoxyglucose and positron emission tomography. *Neurology*, *45*(11), 1996-2004.

Firbank, M. J., Colloby, S. J., Burn, D. J., McKeith, I. G., & O'Brien, J. (2003, Oct 01). Regional cerebral blood flow in parkinson's disease with and without dementia. *NeuroImage*, *20*(2), 1309-1319. doi: 10.1016/S1053-8119(03)00364-1

Friston, K. J., Ashburner, J. T., Kiebel, S. J., Nichols, T. E., & Penny, W. D. (2007). *Statistical parametric mapping: the analysis of functional brain images* (First ed.). London, UK: Academic Press.

Haller, S., Rodriguez, C., Moser, D., Toma, S., Hofmeister, J., Sinanaj, I., ... Lovblad, K.-O. (2013). Acute caffeine administration impact on working memory-related brain activation and functional connectivity in the elderly: A bold and perfusion mri study. *Neuroscience*, *250*, 364 - 371. doi: 10.1016/j.neuroscience.2013.07.021

Hasselmo, M. E. (2006). The role of acetylcholine in learning and memory. *Current Opinion in Neurobiology*, *16*(6), 710-715. doi: 10.1016/j.conb.2006.09.002

Hsiao, I.-T., Huang, C.-C., Hsieh, C.-J., Hsu, W.-C., Wey, S.-P., Yen, T.-C., ... Lin, K.-J. (2012). Correlation of early-phase ^{18}f-florbetapir (av-45/amyvid) pet images to fdg images: preliminary studies. *European Journal of Nuclear Medicine and Molecular Imaging*, *39*(4), 613–620. doi: 10.1007/s00259-011-2051-2

Huang, C., Mattis, P., Perrine, K., Brown, N., Dhawan, V., & Eidelberg, D. (2008). Metabolic abnormalities associated with mild cognitive impairment in parkinson disease. *Neurology*, *70*(16), 1470-1477. doi: 10.1212/01.wnl.0000304050.05332.9c

Huang, C., Mattis, P., Tang, C., Perrine, K., Carbon, M., & Eidelberg, D. (2007). Metabolic brain networks associated with cognitive function in parkinson's disease. *NeuroImage*, *34*(2), 714-723. doi: 10.1016/j.neuroimage.2006.09.003

Huang, C., Tang, C., Feigin, A., Lesser, M., Ma, Y., Pourfar, M., ... Eidelberg, D. (2007). Changes in network activity with the progression of parkinson's disease. *Brain*, *130*(7), 1834-1846. doi: 10.1093/brain/awm086

Jeffrey, S. (2014, March). *Fda approves third amyloid pet tracer for alzheimer's disease.* http://www.medscape.com/viewarticle/822370. (Accessed: 2016-04-11)

Jenkinson, M., Beckmann, C. F., Behrens, T. E. J., Woolrich, M. W., & Smith, S. M. (2012, Aug 15). Fsl. *NeuroImage*, *62*(2), 782-790. doi: 10.1016/j.neuroimage.2011.09.015.

Jolliffe, I. T. (2002). *Principal component analysis* (2nd ed.). New York: Springer.

Jueptner, M., & Weiller, C. (1995). Review: Does measurement of regional cerebral blood flow reflect synaptic activity? - implications for pet and fmri. *NeuroImage*, *2*(2, Part A), 148 - 156. doi: 10.1006/nimg.1995.1017

Klunk, W. E., Engler, H., Nordberg, A., Wang, Y., Blomqvist, G., Holt, D. P., ... Lngstrm, B. (2004). Imaging brain amyloid in alzheimer's disease with pittsburgh compound-b. *Annals of Neurology*, *55*(3), 306–319. doi: 10.1002/ana.20009

Lacalle-Aurioles, M., Alemn-Gmez, Y., Guzmn-De-Villoria, J. A., Cruz-Ordua, I., Mateos-Prez, J. O. J. M., Martino, M. E., ... Desco, M. (2013). Is the cerebellum the optimal reference region for intensity normalization of perfusion mr studies in early alzheimers disease? *PLoS ONE*, *8*(12), e81548. doi: 10.1371/journal.pone.0081548

Liepelt, I., Reimold, M., Maetzler, W., Godau, J., Reischl, G., Gaenslen, A., ... Berg, D. (2009). Cortical hypometabolism assessed by a metabolic ratio in parkinson's disease primarily reflects cognitive deterioration - [^{18}f]fdg-pet. *Movement Disorders*, *24*(10), 1504-1511. doi: 10.1002/mds/22662

Lin, C., Bernstein, M., Huston, J., & Fain, S. (2001). Measurements of t1 relaxation times at 3.0t: Implications for clinical mra. *Proc. Intl. Soc. Mag. Reson. Med*, *9*, 1391.

Litvan, I., Goldman, J. G., Tröster, A. I., Schmand, B. A., Weintraub, D., Petersen, R. C., ... Emre, M. (2012). Diagnostic criteria for mild cognitive impairment in parkinson's disease: Movement disorder society task force guidelines. *Movement Disorders*, *27*(3), 349–356. doi: 10.1002/mds.24893

Ma, Y., Tang, C., Spetsieris, P. G., Dhawan, V., & Eidelberg, D. (2007). Abnormal metabolic network activity in parkinson's disease: test-retest reproducibility. *Journal of Cerebral Blood Flow and Metabolism*, *27*(3), 597-605. doi: 10.1038/sj.jcbfm.9600358

McRobbie, D. W., Moore, E. A., Graves, M. J., & Prince, M. R. (2003). *Mri: From*

motion to picture (2nd ed.). New York, USA: Cambridge University Press.

Melzer, T., Watts, R., MacAskill, M. R., Pearson, J. F., Rüeger, S., Pitcher, T. L., ... Anderson, T. J. (2011, February). Arterial spin labelling reveals an abnormal cerebral perfusion pattern in parkinson's disease. *Brain*, *134*(3), 845-855. doi: 10.1093/brain/awq377

Melzer, T. R. (2011). *Magnetic resonance imaging of cognition in parkinson's disease* (Unpublished doctoral dissertation). University of Otago, Christchurch, New Zealand.

Melzer, T. R., Watts, R., MacAskill, M. R., Pitcher, T. L., Livingston, L., Keenan, R. J., ... Anderson, T. J. (2012). Grey matter atrophy in cognitively impaired parkinsons disease. *J Neurol Neurosurg Psychiatry*, *83*(2), 188-194. doi: 10.1136/jnnp-2011-300828

Mergenthaler, P., Lindauer, U., Dienel, G. A., & Meisel, A. (2013). Sugar for the brain: the role of glucose in physiological and pathological brain function. *Trends in Neurosciences*, *36*(10), 587-597. doi: 10.1016/j.tins.2013.07.001

Nobili, F., Abbruzzese, G., Morbelli, S., Marchese, R., Girtler, N., Dessi, B., ... Rodriguez, G. (2009). Amnestic mild cognitive impairment in parkinson's disease: A brain perfusion spect study. *Movement Disorders*, *24*(3), 414-421. doi: 10.1002/mds.22381

Nordberg, A. (2004). Pet imaging of amyloid in alzheimer's disease. *The Lancet Neurology*, *3*(9), 519-527. Retrieved from http://search.proquest.com.ezproxy.canterbury.ac.nz/docview/201514477?accountid=14499

Petrou, M., Dwamena, B. A., Foerster, B. R., MacEachern, M. P., Bohnen, N. I., Mller, M. L., ... Frey, K. A. (2015). Amyloid deposition in parkinson's disease and cognitive impairment: A systematic review. *Movement Disorders*, *30*(7), 928–935. doi: 10.1002/mds.26191

Piechnik, S., Evans, J., Bary, L., Wise, R., & Jezzard, P. (2009). Functional changes in csf volume estimated using measurement of water t2 relaxation. *Magnetic Resonance in Medicine*, *61*(3), 579–586. Retrieved from http://dx.doi.org/10.1002/mrm.21897 doi: 10.1002/mrm.21897

Poudel, G. R., Innes, C. R. H., & Jones, R. D. (1994). Cerebral perfusion differences

between drowsy and nondrowsy individuals after acute sleep restriction. *Sleep*, *35*(8), 1085-1096. doi: 10.5665/sleep.1994

Press, W. H., Teukolsky, S. A., Vetterling, W. T., & Flannery, B. P. (1992). *Numerical recipes in c* (Second ed.). Cambridge: Cambridge University Press.

Rawlings, J. O., Dickey, D. A., & Pantula, S. G. (1998). *Applied regression analysis: A research tool* (2nd ed.). New York, USA: Springer-Verlag.

Razifar, P., Muhammed, H. H., Engbrant, F., Svensson, P., Olsson, J., Bengtsson, E., ... Bergström, M. (2009, April). Performance of principal component analysis and independent component analysis with respect to signal extraction from noisy positron emission tomography data - a study on computer simulated images. *The Open Neuroimaging Journal*, *3*, 1-16. doi: 10.2174/1874440000903010001

Ringnèr, M. (2008, March). What is principal component analysis? *Nature Biotechnology*, *26*(3), 303-304. doi: 10.1038/nbt0308-303

Sabri, O., Seibyl, J., Rowe, C., & Barthel, H. (2015). Beta-amyloid imaging with florbetaben. *Clinical and Translational Imaging*, *3*(1), 13-26. doi: 10.1007/s40336-015-0102-6

Scatton, B., Javoy-Agid, F., Rouquier, L., Dubois, B., & Agid, Y. (1983). Reduction of cortical dopamine, noradrenaline, serotonin and their metabolites in parkinson's disease. *Brain Research*, *275*(2), 321-328. doi: 10.1016/0006-8993(83)90993-9

Smith, S. M. (2002, November). Fast robust automated brain extraction. *Human Brain Mapping*, *17*(3), 143-155. doi: 10.1002/hbm.10062

Smith, S. M., & Nichols, T. E. (2009). Threshold-free cluster enhancement: Addressing problems of smoothing, threshold dependence and localisation in cluster inference. *NeuroImage*, *44*(1), 83-98. Retrieved from http://search.proquest.com.ezproxy.canterbury.ac.nz/docview/1506807232?accountid=14499

Spetsieris, P. G., Ma, Y., Dhawan, V., & Eidelberg, D. (2009, May 01). Differential diagnosis of parkinsonian syndromes using pca-based functional imaging features. *NeuroImage*, *45*(4), 1241-1252. Retrieved from http://search.proquest.com.ezproxy.canterbury.ac.nz/docview/1506784811?accountid=14499

Stanisz, G. J., Odrobina, E. E., Pun, J., Escaravage, M., Graham, S. J., Bronskill, M. J.,

& Henkelman, R. M. (2005). T1, t2 relaxation and magnetization transfer in tissue at 3t. *Magnetic Resonance in Medicine*, *54*(3), 507–512. doi: 10.1002/mrm.20605

Stone, J. V. (2002, February). Independent component analysis: an introduction. *Trends in Cognitive Sciences*, *6*(2), 59-64. doi: 10.1016/S1364-6613(00)01813-1

Surti, S. (2015). Update on time-of-flight pet imaging. *Journal of Nuclear Medicine*, *56*(1), 98-105. doi: 10.2967/jnumed.114.145029

Tortora, G. R., & Derrickson, B. (2012). *Principals of anatomy and physiology* (13th ed.). USA: John Wiley and Sons, Inc.

Verel, I., Visser, G. W. M., & van Dongen, G. A. (2005, January). The promise of immuno-pet in radioimmunotherapy. *The Journal of Nuclear Medicine*, *46*(1), 164S-171S.

Villain, N. N. (2012). Regional dynamics of amyloid- deposition in healthy elderly, mild cognitive impairment and alzheimer's disease: a voxelwise pib-pet longitudinal study. *Brain*, *135*(7), 2126-2139. doi: 10.1093/brain/aws125

Villemagne, V. L., Mulligan, R. S., Pejoska, S., Ong, K., Jones, G., O'Keefe, G., ... Rowe, C. C. (2012). Comparison of 11c-pib and 18f-florbetaben for aβ imaging in ageing and alzheimer's disease. *European Journal of Nuclear Medicine and Molecular Imaging*, *39*(6), 983–989. doi: 10.1007/s00259-012-2088-x

Webster, M. (2015). *Randomise/ user guide.* http://fsl.fmrib.ox.ac.uk/fsl/fslwiki/Randomise/UserGuide.

Winkler, A. M., Ridgway, G. R., Webster, M. A., Smith, S. M., & Nichols, T. E. (2014, May). Permutation inference for the general linear model. *NeuroImage*, *92*, 381-397. doi: 10.1016/j.neuroimage.2014.01.060

Wood, K.-L., Myall, D. J., Livingston, L., Melzer, T. R., Pitcher, T. L., MacAskill, M. R., ... Dalrymple-Alford, J. C. (2016). Different pd-mci criteria and risk of dementia in parkinsons disease: 4-year longitudinal study. *npj Parkinson's Disease*, *2*. Retrieved from http://www.nature.com/articles/npjparkd201527 doi: 10.1038/npjparkd.2015.27

Yang, X., Beason-Held, L., Resnick, S. M., & Landman, B. A. (2011). Robust biological parametric mapping: An improved technique for multimodal brain image analysis. *Proceedings of SPIE–the International Society for Optical Engineering*,

7962(79623X). doi: 10.1117/12.877593

Ye, F. Q., Berman, K. F., Ellmore, T., Esposito, G., van Horn, J. D., Yang, Y., ... McLaughlin, A. C. (2000). H 2 15 o pet validation of steady-state arterial spin tagging cerebral blood flow measurements in humans. *Magnetic Resonance in Medicine*, *44*(3), 450–456. doi: 10.1002/1522-2594(200009)44:3⟨450::AID-MRM16⟩3.0.CO;2-0